Supplementary Information

for

On-site biosignal amplification using a single high-spin conjugated polymer

Gao-Yang Ge[1,#], *Jingcao Xu*[1,#], *Xinyue Wang*[2], *Wenxi Sun*[1], *Mo Yang*[2], *Zi Mei*[3], *Xin-Yu Deng*[1], *Peiyun, Li*[1], *Xiran Pan*[1], *Jia-Tong Li*[1], *Xue-Qing Wang*[1], *Zhi Zhang*[1], *Shixian Lv*[1], *Xiaochuan Dai*[2], *and Ting Lei*[1,*]

[1]National Key Laboratory of Advanced Micro and Nano Manufacture Technology, School of Materials Science and Engineering, Peking University, Beijing 100871, China

[2]Department of Biomedical Engineering, School of Medicine, Tsinghua University, Beijing 100084, China

[3]School and Hospital of Stomatology, Peking University, Beijing 100871, China

[#]These authors contributed equally to this work

[*]E-mail: tinglei@pku.edu.cn

Table of Contents

1. Experimental Details

Materials

All the chemical reagents were purchased and used as received unless otherwise indicated. All air and water-sensitive reactions were performed under a nitrogen atmosphere. Dichloromethane (DCM), tetrahydrofuran (THF), toluene, and *N*, *N*-dimethylformamide (DMF) were dried using a JC Meyer solvent drying system before use. Ultradry solvents were obtained from J&K reagent company.

Chemical structure and optoelectronic property characterization

^{1}H NMR and ^{13}C NMR spectra were recorded on a Bruker ARX-400 (400 MHz) spectrometer. All chemical shifts were reported in parts per million (ppm). ^{1}H NMR chemical shifts were referenced to $CDCl_3$ (7.26 ppm), and ^{13}C NMR chemical shifts were referenced to $CDCl_3$ (77.16 ppm). Mass spectra were recorded on a Fourier-transform high-resolution mass spectrometer (FTMS). Thermogravimetric analyses (TGA) were carried out on a TA Instrument Q600 SDT analyzer, and differential scanning calorimetry (DSC) analyses were performed on a TA Instrument Q2000 analyzer. Absorption spectra were recorded on a PerkinElmer Lambda 750 UV-vis spectrometer. Cyclic voltammograms (CV) were measured through an electrochemical workstation SP-300 (BioLogic Science Instruments). A standard three-electrode setup was established by employing glassy carbon as the working electrode (WE), a block of platinum mesh as the counter electrode (CE), and an Ag/AgCl electrode as the reference electrode (RE), further calibrated against ferrocene (Fc/Fc^{+}). The measurements were carried out in an aqueous solution with 0.1 M NaCl or in acetonitrile with 0.1 M tetrabutylammonium hexafluorophosphate as the supporting electrolyte with a scan rate of 50 mV/s. HOMO and LUMO energy levels were obtained using the equation: $E_{HOMO} = (E_{Ox} - E_{Fc/Fc^{+}} + 4.8)$ eV, $E_{LUMO} = (E_{Red} - E_{Fc/Fc^{+}} + 4.8)$ eV. Electron paramagnetic resonance (EPR) spectroscopy was conducted on a Bruker E580 spectrometer using ER 4122 SHQE highly sensitive EPR cavity. An Qxford EPR900 cryostat was used for temperature control. The microwave frequency is at 9.37 GHz.

Gel permeation chromatography measurement

Polymer number-average molecular weight (M_n) and molecular weight distributions (PDI = M_w/M_n)

were measured by gel permeation chromatography (GPC). HFIP GPC analyses were performed on a Waters 1515 instrument equipped with a PLMIXED 7.5 × 50 mm guard column, two PLMIXED-C 7.5 × 300 columns, and a differential refractive index detector at 35 °C with a flow rate of 1 mL/min. The instrument was calibrated using 10 PS standards, and chromatograms were processed with Waters Breeze software.

DFT calculations

a) Neutral states:

The geometries of P(TII-T), P(TII-2FT), P(TII-2ClT), and other polymers were optimized at the (R/U)B3LYP/6-311G(d,p) level in the gas phase using the Gaussian 16 software package[1]. For closed-shell singlet states, B3LYP was used. For open-shell states, UB3LYP and a broken-symmetry approach were used. Long side chains were replaced with methyl groups to simplify the calculation. The ΔE_{ST} was calculated from the energy difference between the open-shell singlet and triplet states. The diradical character index (y_0) was performed at the PUHF/6-311G(d,p) level (*Nat Commun.* 12, 5889 (2021)) and calculated by the following equations (*Nat. Commun.* 13, 2258 (2022); *Phys. Chem. Chem. Phys.* 20, 24227-24238 (2018)):

$$y_0 = 1 - \frac{2T}{1+T^2}, T = \frac{n_{HOMO} - n_{LUMO}}{2}$$

where n_{HOMO} and n_{LUMO} are the occupancy numbers of the HOMO and LUMO in the natural orbital analysis.

The spin density distribution was performed at the UωB97XD/6-311G(d,p) level. The bond length alternation (BLA) and the energy ($E_{neutral}$) were performed at the ωB97XD/6-311G(d,p) level. The relaxed potential energy surface (PES) of the dihedral angles in these polymer building blocks was performed at the ωB97XD/6-311G(d,p) level. For each building block, the defined dihedral angle was fixed while the rest of the building block was allowed to relax. The planarity indexes ⍰$\cos^2\varphi$⍰ of these polymer building blocks were calculated according to the literature (*Angew. Chem. Int. Ed.* 60, 1364-1373 (2021)).

b) Charged states:

The geometries of charged P(TII-T), P(TII-2FT), P(TII-2ClT), and other polymers were optimized at the UB3LYP/6-311G(d,p) level in the gas phase. The energies ($E_{positive}$ and $E_{negative}$) and

the PES of the dihedral angles in these charged polymer building blocks were performed at the UωB97XD/6-311G(d,p) level (*Nat Commun.* 13, 5970 (2022)). The planarity indexes ⟨cos²φ⟩ of these charged polymer building blocks were also calculated according to the literature (*Angew. Chem. Int. Ed.* 60, 1364-1373 (2021)).

c) Visualization:

Molecular frontier orbitals and energy levels were extracted by Gaussian View 6[2]. The spin density distribution and bond length alternation (BLA) were visualized by Multiwfn[3] and VMD[4].

Planarization index ⟨ cos²φ⟩

The ⟨ cos²φ⟩ index was first proposed by Perepichka et al. (*Angew. Chem. Int. Ed.* 60, 1364-1373 (2021)). In their work, they presented a detailed calculation process for evaluating the planarity of a polymer backbone, which involves three steps:

a) First, the relaxed potential energy surface (PES) of the dihedral angles in the polymer building blocks was calculated at the ωB97XD/6-311G(d,p) level. For each building block, the defined dihedral angle (φ) was fixed while the rest of the building block was allowed to relax. After the PES calculation, the energy profile $E(\varphi)$ was extracted, showing the potential energy distribution as the dihedral angles between the "TII unit" and "thiophene/fluorinated thiophene/chlorinated thiophene" varied from 0° to 180° at intervals of 10°.

b) The probability function $P(\varphi)$ is calculated using a Boltzmann distribution:

$$P(\varphi) = Ae^{-\frac{E(\varphi)}{RT}}$$

where φ is 0° and ±180° for *s*-trans and *s*-cis conformations, respectively, T = 298 K, and A is a normalizing factor.

c) By considering all their torsional conformations and their relative contributions to the overall structural disorder, the concept of the planarization index ⟨ cos²φ⟩ was proposed to quantify planarity as a collective property within the thermodynamic ensemble:

$$\langle \cos^2 \varphi \rangle = \frac{\int_0^{2\pi} P(\varphi) \cos^2 \varphi \, d\varphi}{\int_0^{2\pi} P(\varphi) \, d\varphi}$$

The ⟨ cos²φ⟩ is well-suited as a representation of backbone planarity because it:

a) serves as a natural sinusoidal approximation of π-orbital overlap (*Chem. Eur. J.* 15, 8613-

8624 (2009)), also observed as the Karplus relationship for spin coupling in NMR (*J. Am. Chem. Soc.* 85, 2870-2871 (1963));

b) equates *s*-cis and *s*-trans conformations, focusing solely on planarity;

c) ranges between 0 (perpendicular) and 1 (coplanar);

d) is linearly related to the Wiberg bond order (B.O.) of the bridging C-C bond, representing the degree of π-conjugation (*Tetrahedron* 24, 1083-1096 (1968)).

Based on these points, we employed the planarization index $\langle \cos^2\varphi \rangle$ to quantify backbone planarity in our manuscript.

Charge carrier density calculations

Charge carrier density can be calculated by the mobility and charge carrier concentration in electrochemical doping. Taking the hole density as an example：

$$J = \frac{I}{A} = \frac{I}{W \times d} = \sigma E = ep\mu_{\mathrm{h}}\frac{V}{L}$$

where J is the current density derived from the current (I) and the cross-sectional area of the channel ($W \times d$) in electrochemical doping. σ is the conductivity, and E is the built-in electric field determined by the source-drain voltage (V) and channel length (L). e is the elementary charge, and p is the hole density. The hole mobility (μ_{h}) has been obtained by analyzing the transfer characteristic curve. Therefore, the estimated hole density of P(TII-2FT) is 5.10×10^{20} cm^{-3}. Similarly, the electron density of P(TII-2FT) is estimated to be 5.03×10^{20} cm^{-3}.

We can also estimate the charge carrier density by the capacitance (C) and geometric parameters from GIWAXS, which is a common method for electrochemical systems (*J. Phys. Chem. C*, 116, 3132–3141 (2012)):

$$Q = CV = C^{*}abcV = epabc$$

where the lattice parameters a = 3.57 Å, b = 26.23 Å, c = 25.46 Å is obtained from GIWAXS; C* of P(TII-2FT) is shown in Supplementary Table 3; V = 0.7 V. Therefore, the calculated hole density and electron density are 3.85×10^{20} cm^{-3} and 6.04×10^{20} cm^{-3}, respectively. The electron density and hole density obtained from both methods are of the same order of magnitude, corresponding to a structure where approximately 2 to 3 charges are distributed per four segments,

consistent with empirical results.

Spectroelectrochemistry

Spectroelectrochemistry was performed using an ITO-coated glass slide, which was spin-coated with the polymer solution (3×10^{-3} M chloroform solution) at a rotating speed of 500 rpm for 45 s. These polymer-coated ITO slides were employed as the working electrode (WE) and immersed in a cuvette filled with a 0.1 M aqueous NaCl solution. A Pt mesh was used as the counter electrode (CE), and an AgCl/Ag pellet served as the reference electrode (RE). A PerkinElmer Lambda 750 UV-vis spectrometer was used, with the beam path passing through the electrolyte-filled cuvette and the polymer-coated ITO samples. A background spectrum was recorded with the cuvette/electrolyte/ITO setup before a potential was applied to the cell. The potential was applied to the WE for 5 s before recording the spectra and was maintained for a certain amount of time until the completion of spectrum scanning.

Cytotoxicity

The sample substrate was preloaded into a 6-well plate. 5×10^5 mouse fibroblasts (L929) were seeded into each well and cultured in high glucose DMEM with 10% fetal bovine serum (FBS, 6021031, DAKEWE), 100 U/mL penicillin (Invitrogen), and 100 U/mL streptomycin (Invitrogen) at 37 °C with 5% CO_2 and 95% humidity. After 24 hours, a live/dead staining assay (cat# 40747ES76, Yeasen) was performed to evaluate the biocompatibility of the substrates. Briefly, cells were washed with 1×Assay Buffer. A working solution was prepared by adding 2 mM Calcein-AM solution and 1.5 mM PI solution to 5 mL of 1×Assay buffer. The working solution and assay buffer were added to the cell culture plates at a ratio of 1:2 and incubated at 37 °C for 15 minutes. Live cells (green fluorescence) and dead cells (red fluorescence) were excited with a 490 ± 10 nm laser (Nikon DS-F).

OECT fabrication and characterization

The fabrication of OECTs involved several steps, including the deposition and patterning of metallic electrodes, the parylene layer, and the polymer in the channel. In detail, silica substrates were thoroughly cleaned by ultrasonication in acetone, DI water, and isopropyl alcohol. This

cleaning process was followed by nitrogen blow-drying and a brief oxygen plasma cleaning. Metal pad interconnects and source/drain contacts were patterned. Subsequently, 5 nm of Cr and 35 nm of Au were deposited, and a lift-off process was performed. Metal interconnects and pads were insulated by depositing 1 μm of parylene-C using a PDS 2010 Labcoater-2, along with a 3-(trimethoxysilyl)propyl methacrylate (A-174 silane) adhesion promoter. A 2% aqueous solution of industrial cleaner (Micro-90) was then spin-coated to act as an anti-adhesive for a second sacrificial 1 μm parylene-C film. This second film was used to simultaneously define the active channel area and pattern the underlying parylene layer. Samples were subsequently patterned with a 5 μm thick layer of AZ9260 photoresist and AZ-400K developer. The patterned areas were opened by reactive ion etching with O_2 plasma using an LCCP-6A reactive ion etcher (Leuven Instruments).

The manufacturing process for the vOECT inverter is similar to that of the OECT. Firstly, the bottom layer output end of the inverter was patterned on the cleaned wafer. Next, 5 nm of Cr and 35 nm of Au were deposited and subjected to a lift-off process. A 0.5 μm Parylene-C layer was deposited for insulation using PDS 2010 Labcoater-2, along with 3-(trimethoxysilyl)-propyl methacrylate (A-174 silane) as an adhesion promoter. Then, 5 nm of Cr and 35 nm of Au were deposited again using a similar method and subjected to lift-off, followed by depositing a 0.5 μm insulation layer using PDS 2010 Labcoater-2. The sample was then spin-coated with a 2% aqueous solution of industrial cleaner (Micro-90), followed by depositing 1 μm of Parylene-C for insulation, which served as the sacrificial layer for the vOECT. Next, the sample was patterned using a 5 μm thick layer of AZ9260 photoresist and AZ-400K developer. An LCCP-6A reactive ion etcher (Leuven Instruments) and O_2 plasma were used to open the patterned areas. The flexible vOECT device was fabricated using a similar method, with the difference being that the substrate used a wafer with a deposited 10 μm parylene-C substitute for the cleaned wafer, which can be stripped with tweezers by immersion in a 0.1 M NaCl solution for 30 minutes.

The polymer was dissolved in chlorobenzene at a concentration of 5 mg/mL. The polymer solution was spin-cast onto the etched devices. After a peeling-off process of the second sacrificial parylene layer, the OECTs were ready for measurement. The device characterization was performed on a probe station using a Keithley 4200 SCS analyzer or an Fs-Pro semiconductor parameter analyzer, PDA. An AgCl/Ag pellet (Warner Instruments) was employed as the gate electrode and immersed in a 0.1 M NaCl solution, which covered the polymer film in the channel. The thickness

of the film was determined in a dry state using a DEKTAK profilometer (Bruker).

Electrochemical impedance spectra

Electrochemical impedance spectra (EIS) were conducted on the polymer-coated electrodes using the electrochemical workstation SP-300 (BioLogic Science Instruments). Polymer films were patterned as squares with specific areas through the lithography technique. These polymer-coated electrodes with a glass substrate were employed as the working electrode and fully immersed in a 0.1 M NaCl solution. Additionally, a Pt mesh (CE) and an AgCl/Ag pellet (RE) were employed to establish a standard three-electrode system. The capacitances of polymers measured on Au electrodes with various sizes were obtained through the potential-EIS method, with the DC offset voltage set to the maximum achievable doping for each polymer. The AC amplitude of voltage in the form of a sine wave on the WE was set at 10 mV (RMS), and the frequency was scanned from 1 Hz to 100 kHz. The resulting Bode plots and Nyquist plots were fitted to an equivalent circuit, specifically Randle's circuit Rs (Rp ||C), using the EC-Lab view software. The thickness of the film was determined in a dry state after testing with a DEKTAK profilometer (Bruker).

Simulated EEG monitoring

The amplifier and the Au electrode, both with the same effective area on the same flexible device, were positioned on an agar model (2 wt%). An AgCl/Ag electrode was inserted into the model to simulate the EEG signal source. The signals from the Au electrode and amplifier were recorded using the Fs-Pro semiconductor parameter analyzer, PDA. MATLAB was used for software filtering. The signals were digitally filtered using a 50 Hz notch filter.

Preparation for in vivo ECoG recording

For the in vivo experiments, mature female C57BL/6 mice, 8 weeks of age (Charles River Laboratories), were used throughout this study. The mice were maintained at 22 ±1 °C with humidity ranging from 30% to 70% and were kept on a 12-hour light/dark cycle, with ad libitum access to food. All 910 experiments were supervised and approved by the Animal Care & Use Committees at Tsinghua University (THU-LARC-2023-008). During the surgery, the mice were anesthetized with oxygen-vaporized isoflurane (3% for induction, 1.5-2% for maintenance, 0.5 L/min). Body

temperature was maintained at 37 °C. Craniotomies (1 mm^2) were performed on the skull to expose the cortical surface without removing the dura mater. One silver wire coated with silver chloride was inserted into the cortex to a depth of about 0.5 mm through the craniotomies, serving as the ground electrode. The flexible amplifier was placed in another opening. The craniotomy where the flexible amplifier was positioned was done in different locations revealing various cortical areas such as the motor (M1), somatosensory (S1), and primary visual (V1) cortices. During subsequent tests, a metal bar was affixed to the mouse's skull using dental methacrylate to stabilize the mouse's brain. The FPC connected to the flexible amplifier was secured to the metal fixed bar to prevent the device from moving on the mouse's brain.

Signal acquisition and processing

A function generator, Keithley 3390, was used to bias the inverter (V_{DD}). A PDA Source Meter was utilized to continuously record the output voltage of the amplifiers and the voltage from the AgCl/Ag or Au electrode at a sampling rate of 1 kHz, and exert a negative V_{SS} ($V_{DD} - V_{SS} = 0.8$ V). MATLAB was used for software filtering. The signals were digitally filtered with a 50 Hz notch filter to eliminate interfering noise. Then, a bandpass filter ranging from 3 to 45 Hz was applied to focus on the significant frequency band.

AFM and GIWAXS characterization

Atomic force microscopy (AFM) measurements were carried out using the Dimension icon ScanAsyst (Bruker). Two-dimensional grazing incidence wide-angle X-ray scattering (2D-GIWAXS) measurements were conducted on a Xenocs-SAXS/WAXS system with an X-ray wavelength of 1.5418 Å and an incidence angle of 0.2°. A Pilatus 300 K was used as a 2D detector. Data processing was performed using GIWAXS-Tools (2.3.1) software[5].

2. Supplementary Tables and Figures

Supplementary Table 1. Calculated energy levels and ΔE_{ST} values of P(TII-T), P(TII-2T), and P(TII-TT) with different repeating units (n).

	P(TII-T)			P(TII-TT)			P(TII-2T)		
	HOMO (eV)	LUMO (eV)	ΔE_{ST} (kcal/mol)	HOMO (eV)	LUMO (eV)	ΔE_{ST} (kcal/mol)	HOMO (eV)	LUMO (eV)	ΔE_{ST} (kcal/mol)
n=1	−5.08	−2.81	−18.27	−5.06	−2.86	−17.76	−5.00	−2.86	−17.33
n=2	−4.80	−3.11	−13.25	−4.81	−3.13	−13.51	−4.79	−3.09	−13.55
n=3	−4.69	−3.24	−11.14	−4.72	−3.24	−12.14	−4.72	−3.18	−12.83
n=4	−4.65	−3.31	−10.47	−4.68	−3.30	−11.79	−4.70	−3.22	−14.75

Supplementary Table 2. Summary of the optical and electrochemical properties of the polymers.

polymer	λ_{sol} [a] (nm)	λ_{film} [b] (nm)	HOMO [c] (eV)	LUMO [c] (eV)	$E_{g,opt}$ [b] (eV)	HOMO [d] (eV)	LUMO [d] (eV)	ΔE_{ST} [d] (kcal/mol)
P(TII-T)	949	1017	–4.59	−3.99	0.87	−4.69	−3.24	−11.14
P(TII-2FT)	929	923	−4.76	−4.05	0.95	−4.84	−3.41	−11.32
P(TII-2ClT)	922	941	−4.89	−4.03	0.92	−5.03	−3.38	−13.62

[a] in CF solution; [b] in thin film; [c] obtained by CV measurement; [d] estimated from DFT calculations.

Supplementary Table 3. Summary of the OECT performance of the polymers.

polymer	polarity	$g_{m,norm}$ (S cm^{-1}) [a]	V_{Th} (V) [b]	μC^* (F cm^{-1} V^{-1} s^{-1}) [c]	C^* (F cm^{-3})	$\mu_{h/e}$ [d] (cm^2 V^{-1} s^{-1})
P(TII-T)	p	44.6±3.7	–0.10±0.006	122.2±9.9	157±27	0.78±0.15
	n	2.2±0.3	0.76±0.008	16.4±1.5	203±28	0.08±0.01
P(TII-2FT)	p	50.1±5.0	–0.39±0.014	158.6±21.4	88±11	1.07±0.3
	n	36.7±4.6	0.64±0.006	147.4±13.2	138±13	1.80±0.14
P(TII-2ClT)	p	32.3±1.9	–0.44±0.004	96.4±5.9	180±27	0.54±0.09
	n	15.2±1.6	0.63±0.007	63.0±5.2	214±9	0.30±0.03

[a] The *W*/*L* of all the devices is 100/10 μm. All the OECT devices were operated in a 0.1 M NaCl aqueous solution; [b] V_{th} was determined by extrapolating the corresponding $I_{DS}^{1/2}$ vs. V_{GS}; [c] Six devices were tested and computed for each polymer. [d] μ was calculated from μC^* and the measured volumetric capacitance C^*.

Supplementary Table 4. OECT performance of the three polymers before and after GPC fractionation.

	polarity	$g_{m,\,norm,\,origin}$ (S cm^{-1})	μC^*_{origin} (F cm^{-1} V^{-1} s^{-1})	$g_{m,\,norm,\,GPC}$ (S cm^{-1})	μC^*_{GPC} (F cm^{-1} V^{-1} s^{-1})
P(TII-2FT)	p	32.1±1.9	83.2±5.3	50.1±5.0	158.6±21.4
	n	19.6±1.8	71.5±6.4	36.7±4.6	147.4±13.2
P(TII-T)	p	44.6±3.7	122.2±9.9	67.62±1.5	179.7±5.2
	n	2.2±0.3	16.4±1.5	2.97±0.4	21.4±3.1
P(TII-2ClT)	p	32.3±1.9	96.4±5.9	43.5±3.2	133.8±9.7
	n	15.2±1.6	63.0±5.2	19.2±1.1	111.3±7.5

Supplementary Table 5. Summary of reported n-type and ambipolar OECT performances.

Polymer	Number	Polarity	HOMO [a] (eV)	LUMO [a] (eV)	μC^* (F cm^{-1} V^{-1} s^{-1})	Ref
BBL_{152}	1	n	−6.12	−4.37	25.9	6
f-BTI2TEG-FT	2	n	−5.59	−3.82	15.2	7
P(C-T)	3	n	−5.53	−4.25	7.6	8
p(gTDPP2FT)	4	n	−5.20	−3.86	54.8	9
f-BTI2g-TVTCN	5	n	−5.57	−3.81	41.3	10
p(C2F-V)	6	n	−6.12	−4.45	108	11
f-BTI2g-TVTF	7	n	−5.60	−3.70	90.2	12
P(gNDI-gT2)	8	p	−4.83	−4.12	N/A	13
		n			0.18	
2DPP-OD-TEG	9	p	−5.08	−3.82	31.8	14
		n			6.8	

P(C4-T2-C0-EG)	10	p n	−5.0	−4.0	0.13 0.16	15
P(C4-T2-C0-EG)	11	p n	−5.0	−4.0	~0.2 0.22	16
PrC60MA:p(g2T-TT) (95:5)	12	p n			22.8 11.8	17
PBBTL:BBL	13	p n			2.72 1.36	18
P(TII-2FT)	14	p n	−4.76	−4.05	158.6 147.4	This work
P(TII-T)	15	p n	–4.59	−3.99	179.7 21.4	This work
P(TII-2ClT)	16	p n	−4.89	−4.03	133.8 111.3	This work

[a] CV measurement results.

Supplementary Table 6. Summary of the device stability for P(TII-2FT) and other reported OECT materials.

Polymer	Number	Cycles	Current retention (%)	type	Optimal μC^* (F cm^{-1} V^{-1} s^{-1})	Ref
f-BTI2g-SVSCN	1	360	45	n	150.9	28
f-BSeI2g-SVSCN	2	360	90	n	191.2	28
p(C2F-V)	3	60	77.2	n	107.56	11
P(gTDPP2FT)	4	257	54	n	54.8	9
f-BTI2g-TVTF	5	100	91	n	90.2	12
p(g3T2)	6	720	15	p	161	29
p(g2T2-g4T2)	7	720	87	p	522	29
p(g1T2-g5T2)	8	720	98	p	496	29

p(g0T2-g6T2)	9	720	98	p	302	29
PTDPP-DT	10	500	91	p	149	30
2DPP-OD-TEG	11	167	5	Ambipolar, p type	31.8	14
			40	Ambipolar, n type	6.8	
P(TII-2FT)	12	1000	96.1	Ambipolar, p type	158.6	This work
			104.5	Ambipolar, n type	147.4	

279 All the unipolar materials are selected with the optimal OECT performance beyond 50 F cm^{-1} V^{-1}
280 in the p-type or n-type operation regime.

281

282 **Supplementary Table 7**. Summary of the gain and supply voltage of different types of inverters.

Polymer	Number	Inverter configuration	V_{DD} (V)	Maxinum gain	Normalized gain	Ref
P(TII-2FT)	1	Ambipolar	0.8	809	1011	This work
PrC60MA:p(g2T-TT) 95:5 (w:w)	2	Ambipolar	0.9	82	91.1	17
p(C4-T2-C0-EG)	3	Ambipolar	0.8	28	35	15
PBBTL:BBL (3:1)	4	Ambipolar	0.6	42	70	18
2DPP-OD-TEG	5	Ambipolar	1.4	50	36	14
PIDTC16-BT, DCNBT-IDT	6	Complementary	0.7	1.1	1.57	19
PIDTPEG-BT, DCNBT-IDT	7	Complementary	0.4	1.2	3	19
BBL, P3HT	8	Complementary	0.7	46	65.7	20
BBL, P3CPT	9	Complementary	0.6	12	20	21
PNDI2TEG-2Tz, Pg2T-TT	10	Complementary	0.6	23.4	39	22
CNg4T2-CNT2, g4T2-T2	11	Complementary	0.8	45	56.25	23
f-BTI2g-TVT, g4T2-T2	12	Complementary	1.4	148	105.7	12
P3HT	13	Unipolar	0.75	8.7	11.6	24
PEDOT: PSS	14	Unipolar	1.3	12.5	9.6	25
PEDOT: PSS	15	Unipolar	0.6	82	136.7	26
P3HT	16	Unipolar	0.85	10	11.8	20
P3HT, PEDOT: PSS	17	Unipolar	0.85	24	28.2	20
PEDOT: PSS	18	Unipolar	0.8	107	133.8	27
PFIBI-BT	19	OFET	100	174	1.74	31
PT-BTD:PDIFCN2	20	OFET	100	84	0.84	31
DNTT:PTCDI-C13	21	OFET	4	130	32.5	31
P1FIID-2FBT	22	OFET	100	94	0.94	31

PTDCNTVT	23	OFET	120	163	1.36	31
PDVT-8:P(NDI2OD-T2)	24	OFET	30	168	5.6	31

Supplementary Table 8. Comparison of the molecular packing parameters of the polymers under different operating conditions.

Samples		(100)			(010)		
		q (Å^{-1})	$d_{lamellar}$ (Å)	CL (Å)	q (Å^{-1})	$d_{\pi-\pi}$ (Å)	CL (Å)
P(TII-T)	pristine	0.24	26.2	79.9	1.76	3.57	60.8
	$NaCl_{(aq)}$ soaked	0.24	26.1	73.8	1.77	3.54	46.0
	n-doped	0.24	26.2	72.5	1.76	3.56	43.4
	p-doped	0.24	26.1	77.6	1.78	3.52	47.4
P(TII-2FT)	pristine	0.24	26.3	85.4	1.79	3.51	41.0
	$NaCl_{(aq)}$ soaked	0.24	26.4	84.0	1.81	3.47	40.0
	n-doped	0.24	26.7	98.7	1.80	3.48	49.0
	p-doped	0.24	26.7	96.9	1.81	3.46	47.0
P(TII-2ClT)	pristine	0.23	27.1	87.61	1.80	3.48	42.1

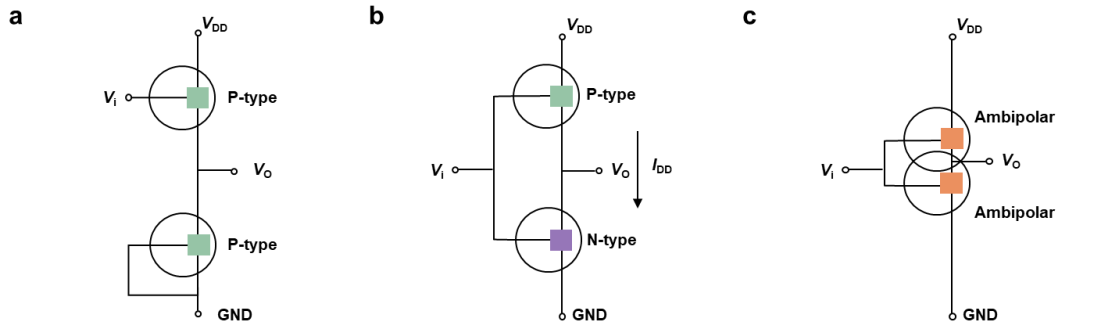

Supplementary Fig. 1 Typical circuit diagrams of inverters constructed by **a** a single p-type material in a ‘‘diode-load’’ configuration, **b** both n-type and p-type materials, and **c** a single ambipolar material with the vOECT structure.

Regarding OECT devices (Supplementary Fig. 1a-c), most studies of inverters constructed by unipolar OECTs usually show lower performance (Fig. 4h) and a notable lack of evidence for their effectiveness directly at the site of interest or within living organisms (in vivo). This shortcoming has been addressed by complementary-type inverters (Supplementary Fig. 1b). However, n-type materials generally have lower performance and poorer stability compared to their p-type counterparts (Fig. 4g). This disparity often requires adjusting the geometric dimensions of the channel to accommodate the unbalanced electronic properties of p-type and n-type materials (*Science 384*, 557 (2024); *Sci. Adv.* 10, eadi9710 (2024)). This results in adverse effects such as complex manufacturing processes, large footprints, low integration, and low device performance (Fig. 4h). In addition, the poor stability of n-type OECT materials significantly limits the practical applications of complementary circuits in bioelectronics. Ambipolar inverters with a cofacial vertical OECT construction (vOECT) could effectively overcome these challenges (Supplementary Fig. 1c). However, similar to n-type OECT materials, current ambipolar materials also show low performance and poor device stability (Fig. 4f), which greatly limits the further development of OECT-based logic circuits and amplifiers in bioelectronics. Unfortunately, the strategy for designing a balanced, efficient, and stable ambipolar material is still unknown.

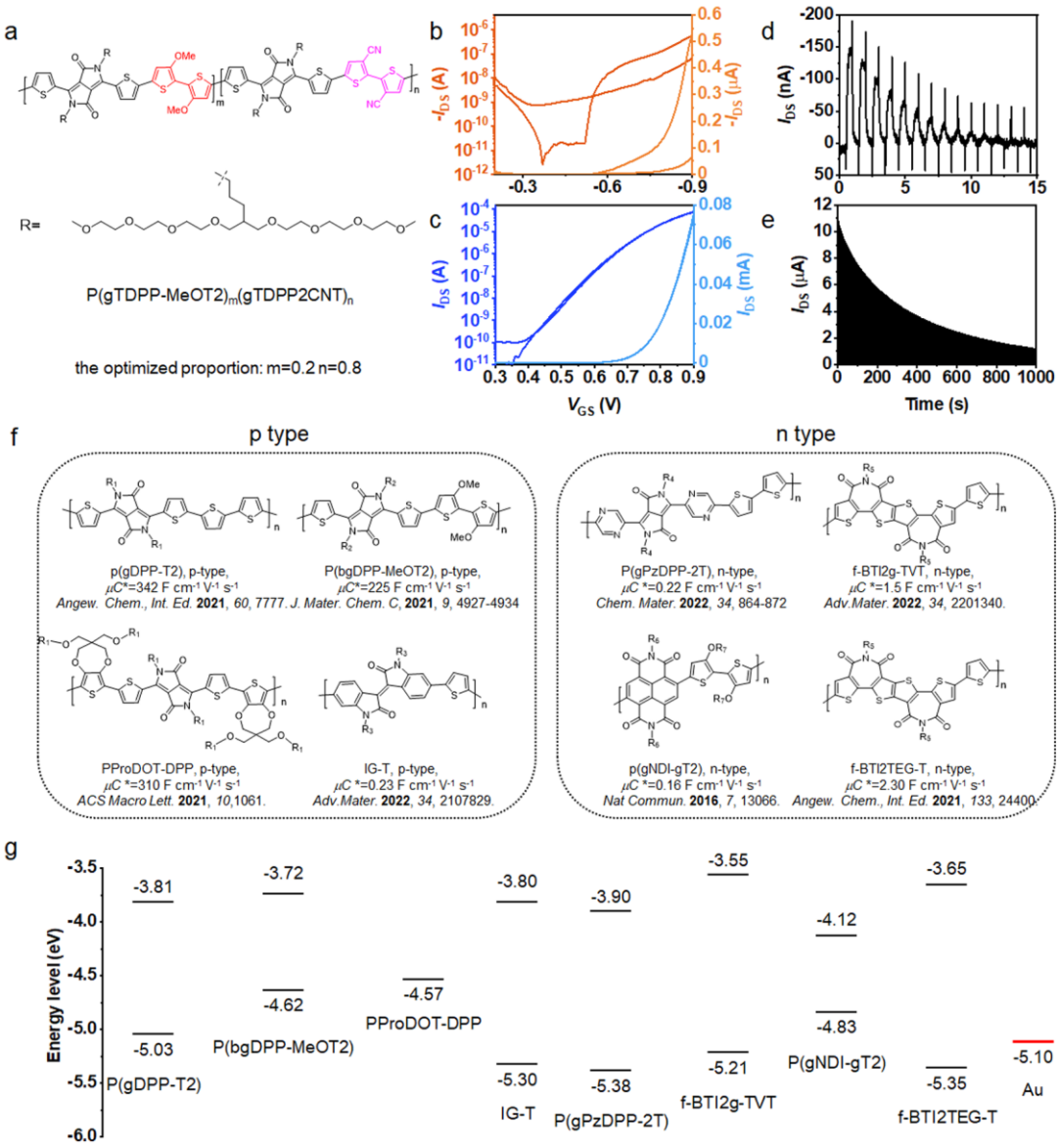

Supplementary Fig. 2 The relationship between molecular energy levels and the OECT performance. a Chemical structures of the copolymer, $P(gTDPP\text{-}MeOT2)_m(gTDPP2CNT)_n$, consisting of p-type and n-type polymer components. **b** P-type and **c** n-type transfer characteristics of $P(gTDPP\text{-}MeOT2)_{0.2}(gTDPP2CNT)_{0.8}$. **d** P-type and **e** n-type operational stability tests for $P(gTDPP\text{-}MeOT2)_{0.2}(gTDPP2CNT)_{0.8}$. **f** Chemical structures of some reported p-type and n-type OECT polymers with a donor-acceptor design. The ethylene glycol (EG) side chains of each polymer are omitted for better clarity. **g** Corresponding HOMO and LUMO energy levels of the polymers (CV measurements).

Traditionally, high-lying HOMO energy levels are beneficial for reducing the energy barrier between p-type materials and gold electrodes, facilitating efficient hole injection. Similarly, low-lying LUMO energy levels are advantageous for efficient electron injection. Therefore, designing

conjugated polymers with donor-acceptor (D-A) structures could effectively enhance ambipolar transport performance in organic field effect transistors (OFETs). However, this approach is not directly applicable to OECTs. In Supplementary Fig. 2a, we designed and synthesized a copolymer, P(gTDPP-MeOT2)$_m$(gTDPP2CNT)$_n$, which combines two different types of OECT polymers: P(gTDPP-MeOT2) (p-type) and P(gTDPP2CNT) (n-type). Based on OECT measurements, the optimized ratio of the polymer is m = 0.2 and n = 0.8. Nevertheless, the unbalanced ambipolar performance and poor stability (Supplementary Fig. 2b-e) suggest that balanced and stable ambipolar OECTs cannot be achieved solely through engineering the molecular energy levels.

To further understand the relationship between molecular energy levels and the transport type of OECT materials, we compiled a list of polymers with D-A structures and their respective transport types, along with their molecular energy levels reported in recent literature for comparison (Supplementary Fig. 2f-g). For instance, compared to the p-type polymer IG-T, the polymer f-BTYI2g-TVT exhibits pure n-type OECT performance despite having a relatively higher HOMO energy level, which should be a p-type OECT material. A similar concern applies to P(gDPP-T2), which is a p-type OECT material with a lower LUMO energy level compared to n-type OECT polymers f-BTYI2g-TVT and f-BTI2TEG-T. Among them, P(gNDI-gT2) is an ambipolar OECT polymer with a narrow molecular bandgap. However, both its p-type and n-type OECT performance are not outstanding due to the twisted backbone and strong charge localization in the doped states.

Despite some deviations in the detailed values of energy levels under different CV test conditions, these results reveal that molecular energy levels are essential but not solely sufficient to determine the charge transport type in OECTs. Other crucial factors, such as molecular planarity and stability in the doped states, should also be adequately considered. We have discussed these aspects in the main text.

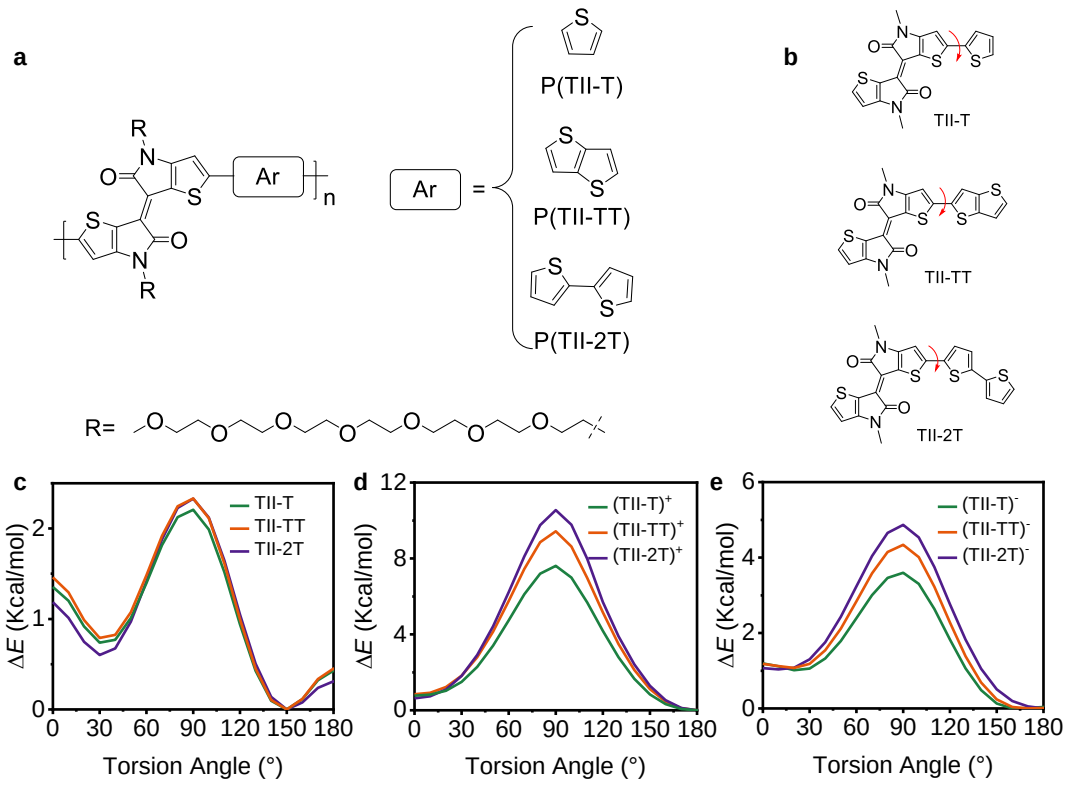

Supplementary Fig. 3 Relaxed PES scans. a Chemical structures of the three polymers: P(TII-T), P(TII-TT) and P(TII-2T). **b** Molecular structures of the three monomers: TII-T, TII-TT, and TII-2T. The EG side chains were replaced with methyl groups to simplify the calculation. Comparison of the relaxed PES scans of the torsion angles for the monomers under **c** neutral, **d** positively, and **e** negatively charged states. The torsion angles are the dihedral angles marked in Supplementary Fig. 3b.

The three monomers (TII-T, TII-TT, and TII-2T) exhibit similar planarity in their neutral or charged states. However, as the repeating units increase, the conjugated backbone of the polymer P(TII-2T) becomes twisted and non-planar due to the presence of torsional angles between the bithiophene (2T) units. Consequently, an anomalous ΔE_{ST} value occurs when the repeating units reach 4 (Fig. 2d and Supplementary Table 1). Compared to P(TII-2T) and P(TII-TT) with the same repeating unit, P(TII-T) displays the largest ΔE_{ST} value, which led us to choose TII and T for constructing the polymer.

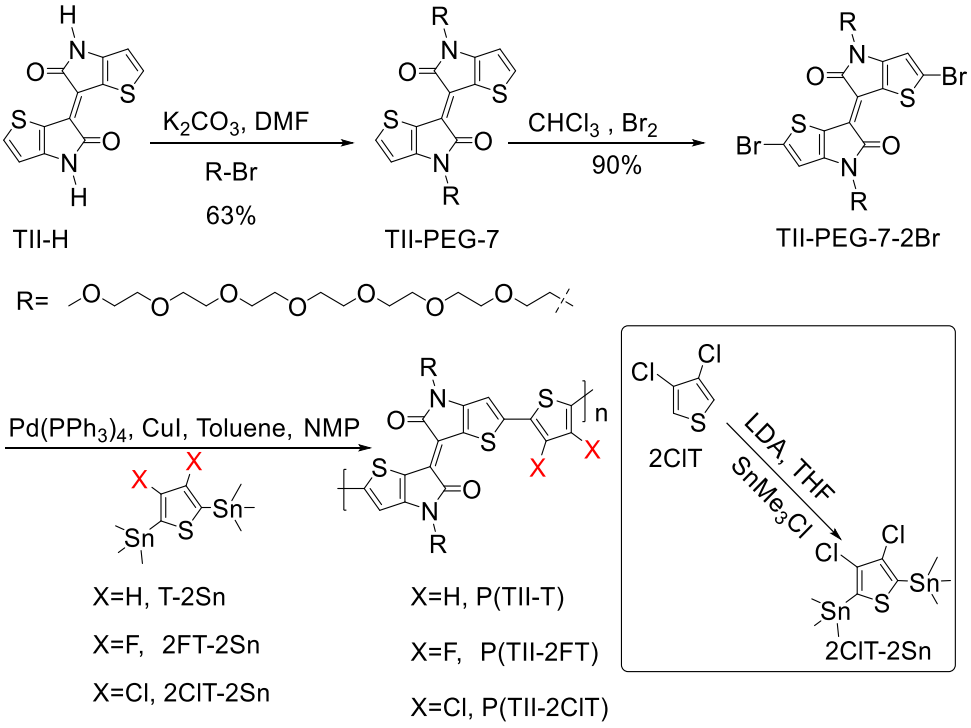

Supplementary Fig. 4 Synthetic routes to the three polymers. P(TII-T), P(TII-2FT), and P(TII-2ClT).

The three polymers were synthesized through Pd-catalyzed Stille coupling reactions with CuI as the co-catalyst, purified by Soxhlet extraction, and collected by chloroform. The molecular weights of the three polymers were evaluated by gel permeation chromatography (GPC) with hexafluoroisopropanol (HFIP) as the eluent (Supplementary Fig. 5). The three polymers show good thermal stability with decomposition temperatures exceeding 300 ℃ (Supplementary Fig. 6 and Supplementary Fig. 7).

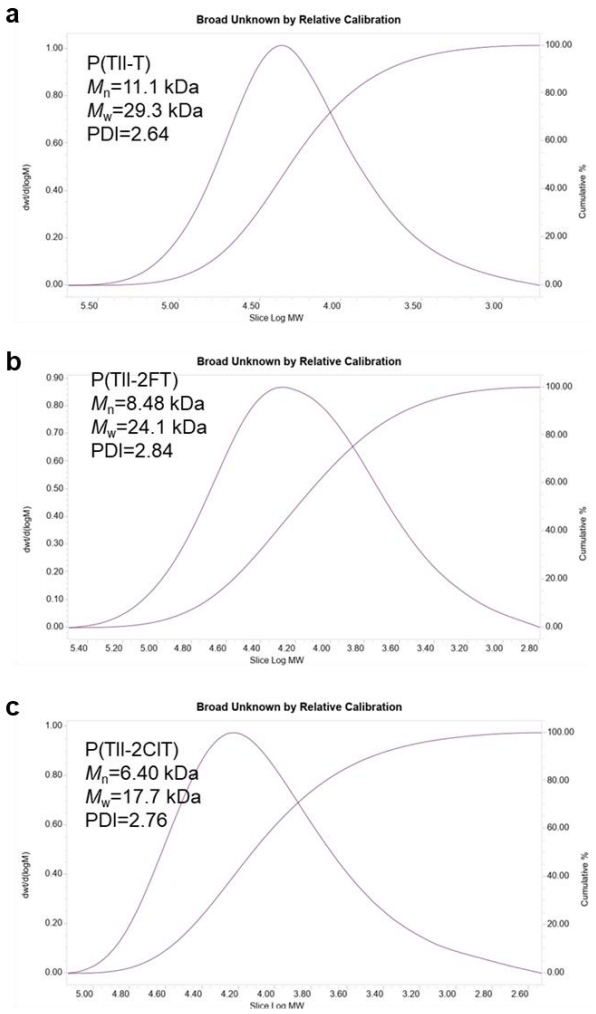

Supplementary Fig. 5 Molecular weights and polymer dispersity index (PDI) of the polymers. **a** P(TII-T), **b** P(TII-2FT), and **c** P(TII-2ClT), measured by GPC with hexafluoroisopropanol (HFIP) as the eluent.

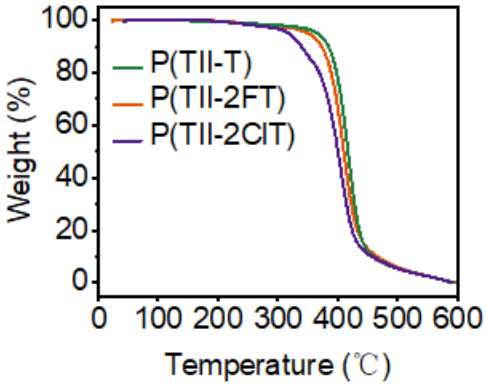

Supplementary Fig. 6 Thermogravimetric analysis (TGA) of the polymers. $T_{d,\ P(TII\text{-}T)}$ = 365 ℃; $T_{d,\ P(TII\text{-}2FT)}$ = 350 ℃; $T_{d,\ P(TII\text{-}2ClT)}$ = 317 ℃.

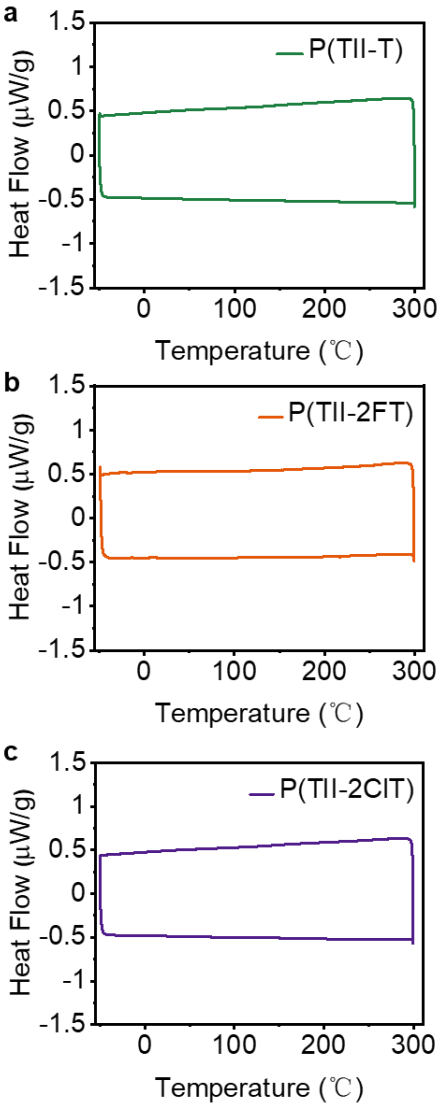

382

383 **Supplementary Fig. 7 Differential scanning calorimetry (DSC) of the polymers. a** P(TII-T), **b**
384 P(TII-2FT), and **c** P(TII-2ClT). All polymers do not show obvious endothermic or exothermic peaks
385 form −50 ℃ to 300 ℃.

386

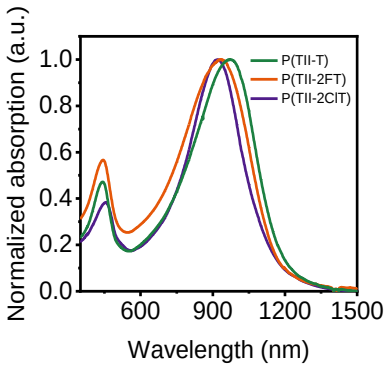

387

388 **Supplementary Fig. 8 The normalized UV-vis-NIR absorption spectra of the polymers.** P(TII-
389 T), P(TII-2FT), and P(TII-2ClT), in chloroform solution.

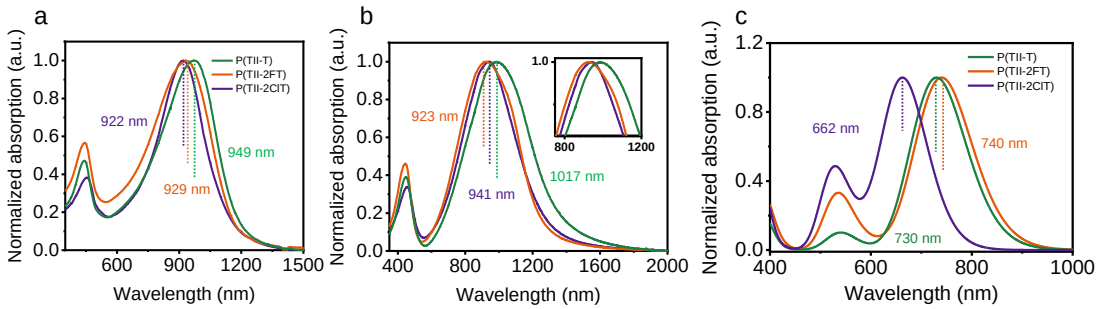

Supplementary Fig. 9 The UV-visible absorption spectra of P(TII-T), P(TII-2FT), and P(TII-2ClT) in **a** dilute chloroform solution and **b** thin film. **c** DFT-calculated absorption spectra for these polymers at the CAM-B3LYP/6-311G(d,p) level in the gas phase.

We conducted DFT calculations to simulate the UV-visible absorption spectra of the three polymers in the gas phase. It can be observed that P(TII-2FT), P(TII-T), and P(TII-2ClT) exhibit progressively blue-shifted absorption spectra (Supplementary Fig. 9c). This phenomenon is inconsistent with the experimental observations that the absorption spectra of the three polymers progressively blue-shift in the order of P(TII-T), P(TII-2FT), and P(TII-2ClT) (Supplementary Fig. 9a, b).

We analyzed the reasons for this difference: (1) The electronic spectra calculated by DFT represent the absorption spectra of the molecular backbones in the single-chain state, while the experimentally measured absorption spectra are obtained in solution or in film states. (2) Therefore, we first performed UV-vis-NIR absorption spectra of the three polymers in three solvents: CF, CB, and *o*-DCB. All their absorption spectra present similar changes, progressively red-shifted in the solvent order of CF, CB, and *o*-DCB (Supplementary Fig. 10a, b, and c). These relatively red-shifted absorption spectra imply strong solution-state aggregation behavior in *o*-DCB solution.

Similar phenomena have been widely observed in various types of high-mobility conjugated polymers (*Chem. Mater.* 36, 3726–3734 (2024); *Adv. Mater.* 32, 2002302 (2020)). As a result, *o*-DCB was chosen as the solvent to measure the temperature-dependent absorption spectra of the three polymers. All three polymers exhibit blue-shifted and weaker absorption spectra as the temperature increases (Supplementary Fig. 10d, e, and f), further suggesting that the three polymers all form an aggregated state in *o*-DCB solution at room temperature (R.T.) (*Angew. Chem. Int. Ed.* 60, 8189–8197 (2021); *Macromolecules*, 45, 9611–9617 (2012)). These phenomena are more

pronounced when cooling down the heated solution to R.T. overnight, as the maximum absorption peaks of the three polymers are slightly red-shifted compared to those of the heated solution cooled down to R.T. immediately (Supplementary Fig. 10g, h, and i). These results indicate that even in the solution state, P(TII-T), P(TII-2FT), and P(TII-2ClT) are all in aggregated states.

As discussed above, all three polymers are in an aggregated state whether in dilute solution or in thin film. When molecules are in an aggregated state, the conjugated backbones are more planar. Based on this conclusion, we flattened the conjugated backbones of P(TII-T) and P(TII-2ClT) during theoretical calculations (Supplementary Fig. 11a, b). The DFT calculation results are as follows: (1) The absorption spectra of P(TII-T) and P(TII-2ClT) with flattened backbones show evident red-shift compared to before (the maximal absorption peaks of P(TII-T) and P(TII-2ClT) shifted from 662/730 nm to 715/740 nm); (2) P(TII-T) exhibits the largest red-shifted absorption spectrum, followed by P(TII-2FT) and P(TII-2ClT), which is consistent with the experimental observations.

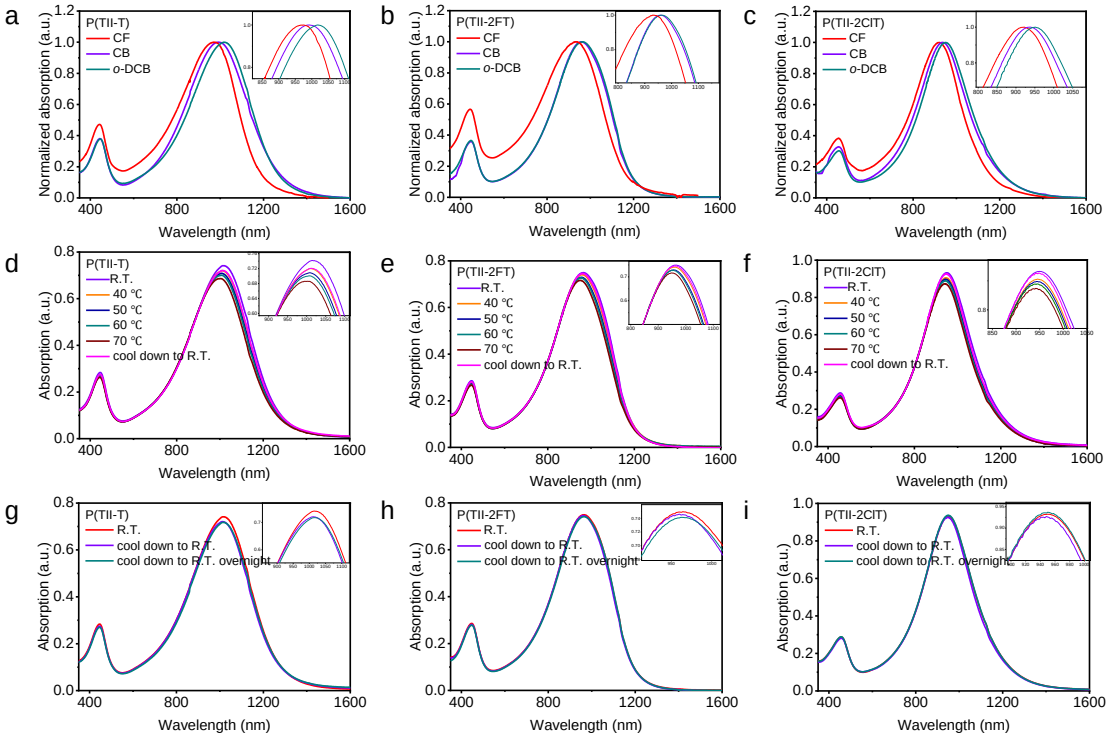

Supplementary Fig. 10 Comparison of the UV-vis-NIR absorption spectra under different testing conditions. UV-vis-NIR absorption spectra of **a** P(TII-T), **b** P(TII-2FT), and **c** P(TII-2ClT) in CF, CB, and *o*-DCB solution (1.0×10^{-5} M). Temperature-dependent UV-vis-NIR absorption spectra of **d** P(TII-T), **e** P(TII-2FT), and **f** P(TII-2ClT) in *o*-DCB. UV-vis-NIR absorption spectra

of **g** P(TII-T), **h** P(TII-2FT), and **i** P(TII-2ClT) in *o*-DCB solution at R.T. or the 70℃ heated solution cooled down to R.T. immediately/overnight.

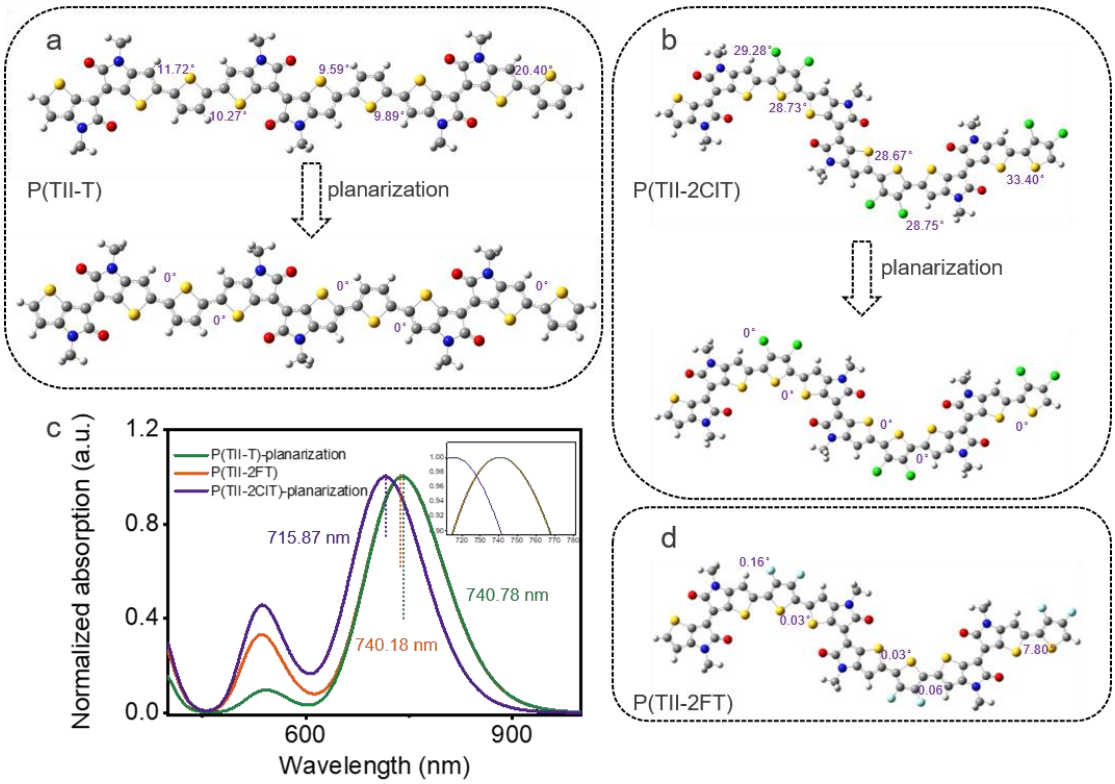

Supplementary Fig. 11 Comparison of the calculated UV-vis-NIR absorption spectra with flattened polymer backbones. Illustration of the flattened molecular backbones of **a** P(TII-T) and **b** P(TII-2ClT). **c** Calculated UV-vis-NIR absorption spectra of the flattened P(TII-T) and P(TII-2ClT). DFT calculations were performed at the CAM-B3LYP/6-311G(d,p) level in the gas phase. **d** DFT-optimized molecular backbone of P(TII-2FT).

In summary, the red-shifted absorption spectra of P(TII-T) compared to the other two polymers can be attributed to the following reasons: (1) Whether in solution or in thin film, the polymer P(TII-T) is in an aggregated state, thereby enhancing the planarity of the polymer backbone; (2) The enhanced planarity, coupled with the strong intramolecular D-A interactions in polymer P(TII-T), results in its absorption spectra exhibiting the most significant red-shift.

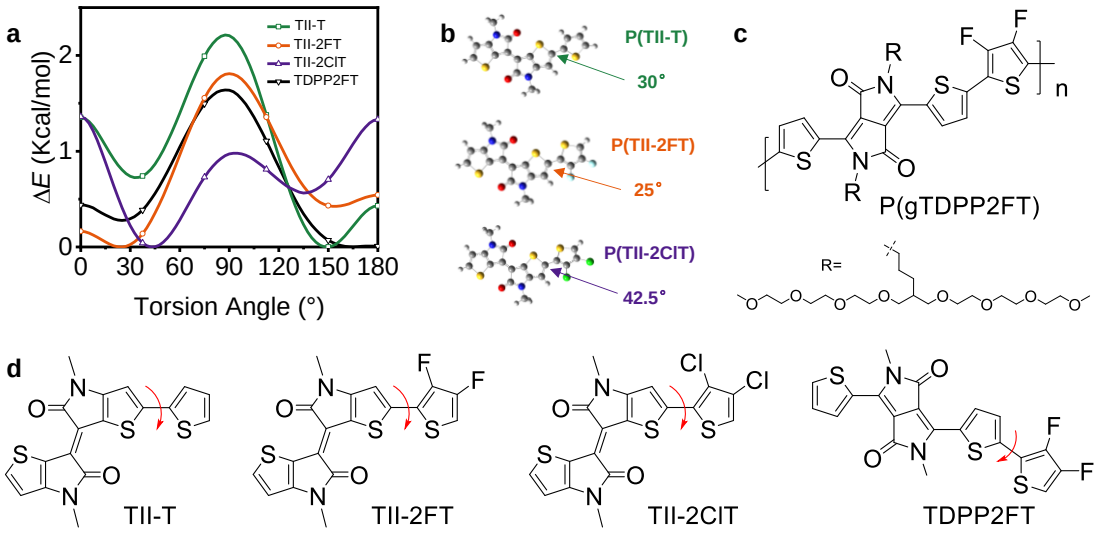

Supplementary Fig. 12 Relaxed PES scans and optimized backbone structures. **a** Comparison of the relaxed PES scans of the torsion angles for the monomers: TII-T, TII-2FT, TII-2ClT, and TDPP2FT. The torsion angles are the dihedral angles marked in Supplementary Fig. 12d. **b** Optimized backbone structures and dihedral angles for the monomers of P(TII-T), P(TII-2FT), and P(TII-2ClT). **c** Chemical structure of polymer P(gTDPP2FT). **d** Molecular structures of the four monomers: TII-T, TII-2FT, TII-2ClT, and TDPP2FT. The EG side chains were replaced with methyl groups to simplify the calculation.

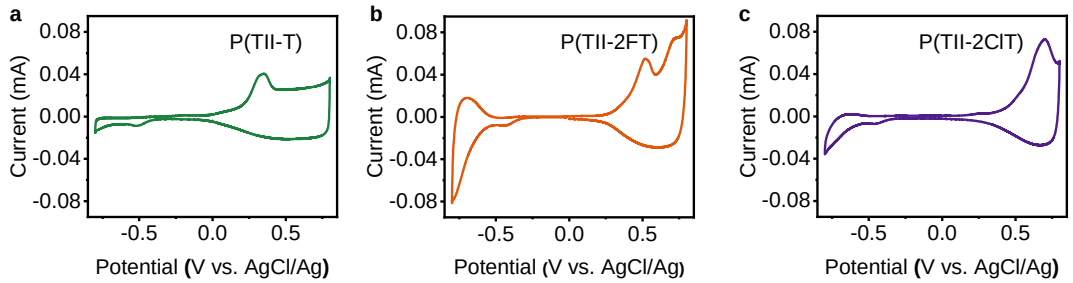

Supplementary Fig. 13 Cyclic voltammograms of the polymers. a P(TII-T), **b** P(TII-2FT), and **c** P(TII-2ClT), in acetonitrile solution with a 0.1 M NaCl aqueous solution as the electrolyte.

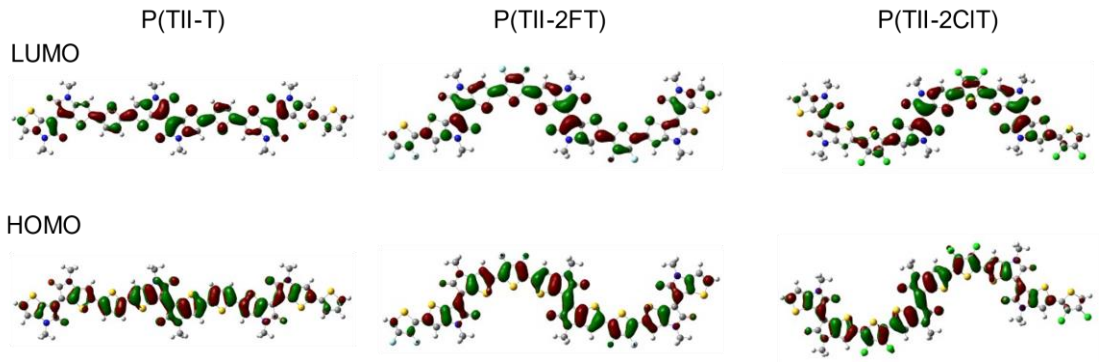

Supplementary Fig. 14 DFT-optimized geometries and molecular frontier orbitals of the

trimers. The EG side chains were replaced with methyl groups to simplify the calculation.

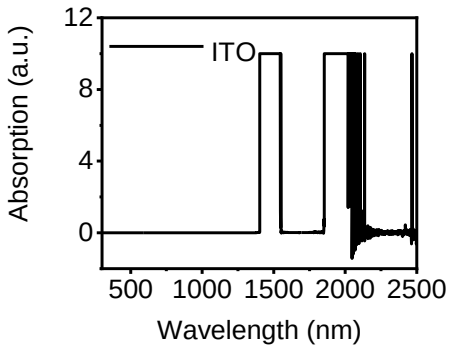

Supplementary Fig. 15 The absorption spectrum of indium tin oxide (ITO) glass. Due to the strong absorption of the ITO glass at wavelengths greater than 1400 nm, the absorption bands of these generated polarons/bipolarons from the polymers are partially obscured in the long-wavelength region.

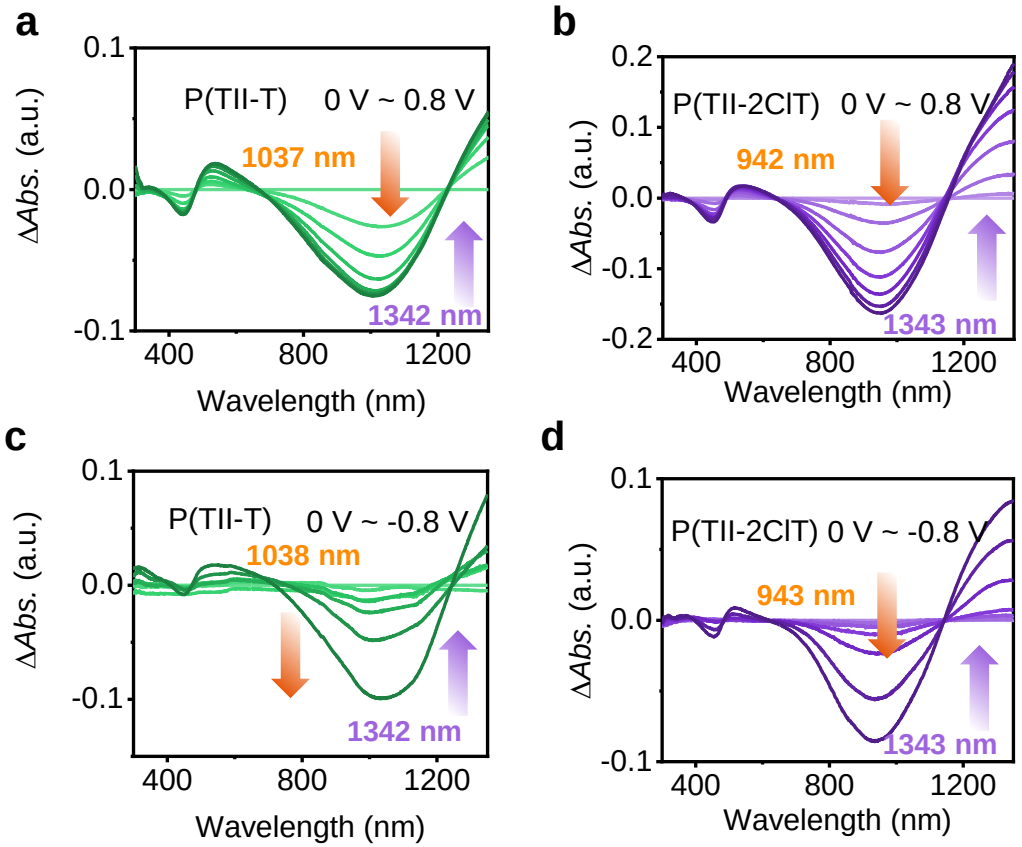

Supplementary Fig. 16 Electrochemical absorption spectra of the polymers. a/c P(TII-T) and **b/d** P(TII-2ClT), with positive voltages (0 to +0.8 V)/negative voltages (0 to –0.8 V) on ITO glass in a 0.1 M NaCl aqueous solution. The Δ*Abs.* represents the difference in absorption intensity at

various bias voltages.

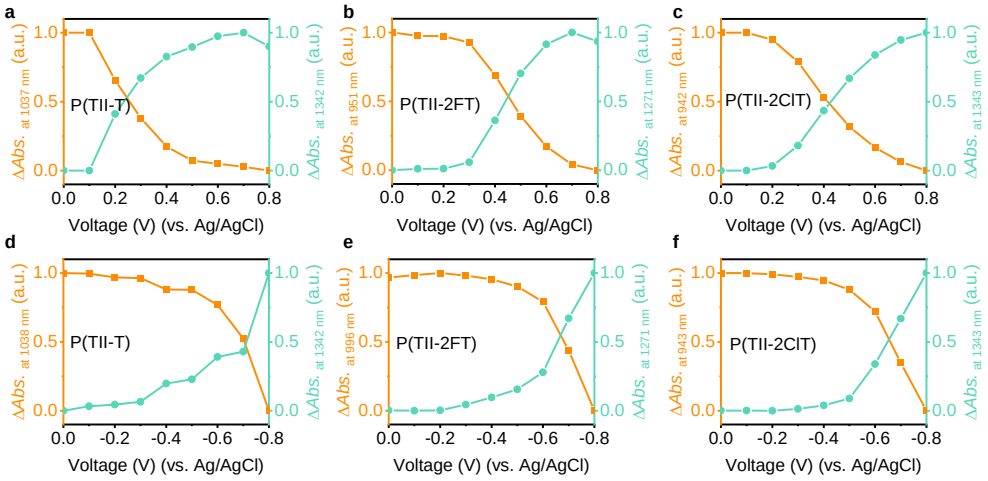

Supplementary Fig. 17 Absorption intensity changes at the tagged wavelengths in the electrochemical absorption spectra. **a/d** P(TII-T), **b/e** P(TII-2FT), and **c/f** P(TII-2ClT), at the different bias voltages.

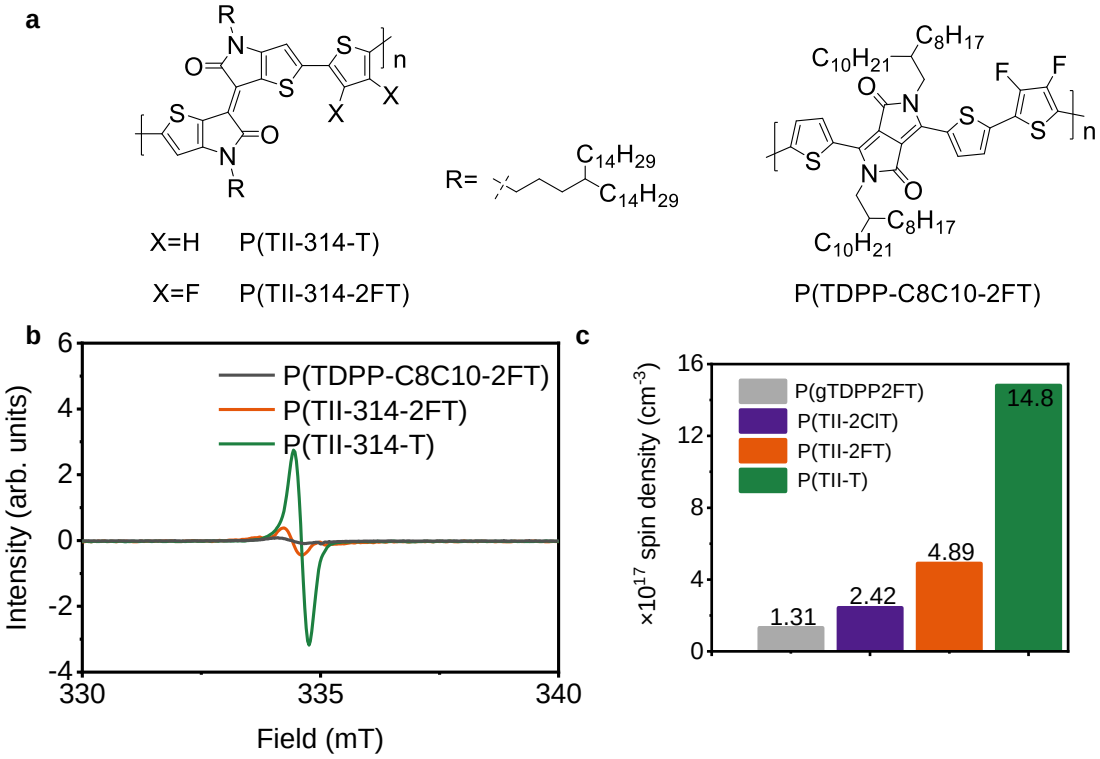

Supplementary Fig. 18 Room temperature EPR signals. a Chemical structures of the alkyl side chain functionalized polymers, P(TII-314-T), P(TII-314-2FT), and P(TDPP-C8C10-2FT). **b** Room temperature EPR signals of P(TII-314-T), P(TII-314-2FT), and P(TDPP-C8C10-2FT) in the solid state. **c** Spin densities of the powders of P(gTDPP2FT), P(TII-T), P(TII-2FT), and P(TII-2ClT) at room temperature.

An n-type OECT polymer, P(gTDPP2FT) (*Nat Commun.* 13, 5970 (2022)), which has a similar structure and backbone planarity (⟨cos^{2}φ⟩ = 0.72) to P(TII-2FT), was also employed for comparison (Supplementary Fig. 12c). At room temperature, P(TII-2ClT), P(TII-2FT), and P(TII-T) exhibited progressively stronger EPR signals, while P(gTDPP2FT) showed almost imperceptible signals (Fig. 3e), indicating its low spin intensity and a tendency to adopt an aromatic closed-shell electronic structure. The spin density extracted from EPR spectra is 2.42×10^{17} cm^{-3} for P(TII-2ClT), 4.89×10^{17} cm^{-3} for P(TII-2FT), and 1.48×10^{18} cm^{-3} for P(TII-T) (Supplementary Fig. 18c). To exclude interference from EG side chains, we synthesized three polymers with the same backbone but alkyl chains for comparison (Supplementary Fig. 18a), and their EPR spectra showed the same trends as the above results (Supplementary Fig. 18b). Thus, the strong EPR signals of the three TII-based polymers collectively indicate the presence of unpaired electrons in their backbone, suggesting that the polymers could adopt a high-spin electronic structure at room temperature. This conclusion is in agreement with the calculated results. The ΔE_{ST} values are −10.00 kcal/mol for P(TII-T), −10.11 kcal/mol for P(TII-2FT), −13.06 kcal/mol for P(TII-2ClT), and −17.66 kcal/mol for P(gTDPP2FT), respectively (Fig. 3d and Supplementary Fig. 19). Besides, the diradical character index (y_0) was also calculated. Normally, the value of y_0 ranges from 0 (a closed-shell characteristic) to 1 (pure diradical). The calculated y_0 values for P(TII-T), P(TII-2FT), P(TII-2ClT), and P(gTDPP2FT) are 0.61, 0.60, 0.45, and 0.43, respectively (Fig. 3d). The large ΔE_{ST} and y_0 values indicate that the order of the open-shell characteristics is as follows: P(TII-T) > P(TII-2FT) > P(TII-2ClT). The above results indicate that the open-shell characteristics of the polymers originate from the TII building blocks, confirming our rational building block screening strategy.

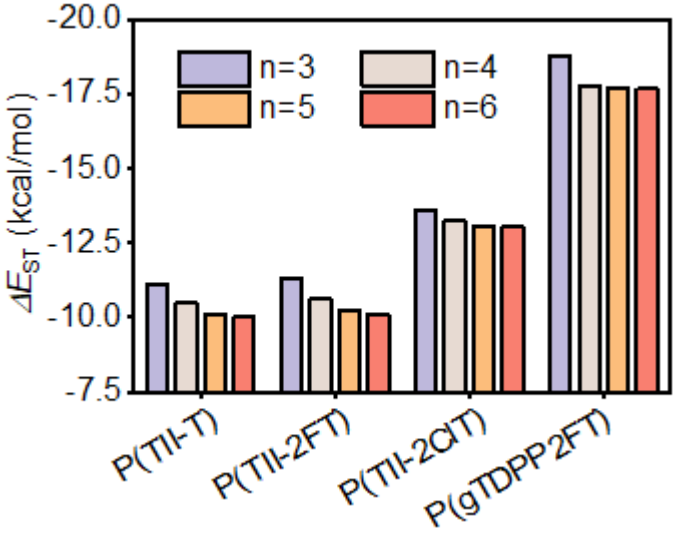

Supplementary Fig. 19. Calculated ΔE_{ST} values. P(TII-T), P(TII-2FT), P(TII-2ClT), and P(gTDPP2FT), with different repeating units (n=3, 4, 5, 6).

As the number of repeating units increases, the calculated ΔE_{ST} values of these four polymers gradually become larger. This trend suggests that the actual polymers may exhibit larger ΔE_{ST} values and might even become positive values due to their longer conjugation lengths. Therefore, the actual polymer with a calculated negative ΔE_{ST} value may also display a high-spin character with the triplet state as the ground state.

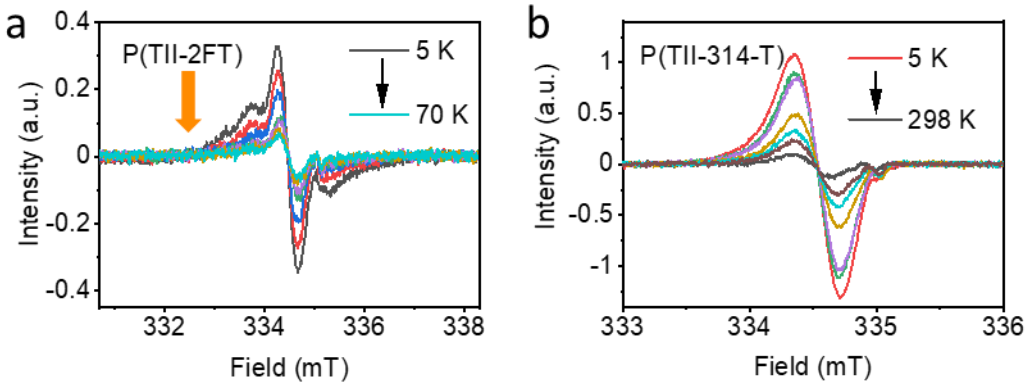

Supplementary Fig. 20 Variable-temperature EPR signals. **a** P(TII-2FT) and **b** P(TII-314-T), in the solid state. The alkyl-substituted polymer P(TII-314-T) exhibits a decreasing trend in EPR signals as the temperature increases, similar to P(TII-2FT) and P(TII-T). This result further indicates that the unpaired electrons originate from their backbones rather than the EG side chains, suggesting the potential presence of a triplet ground state in the backbones of P(TII-2FT) and P(TII-T).

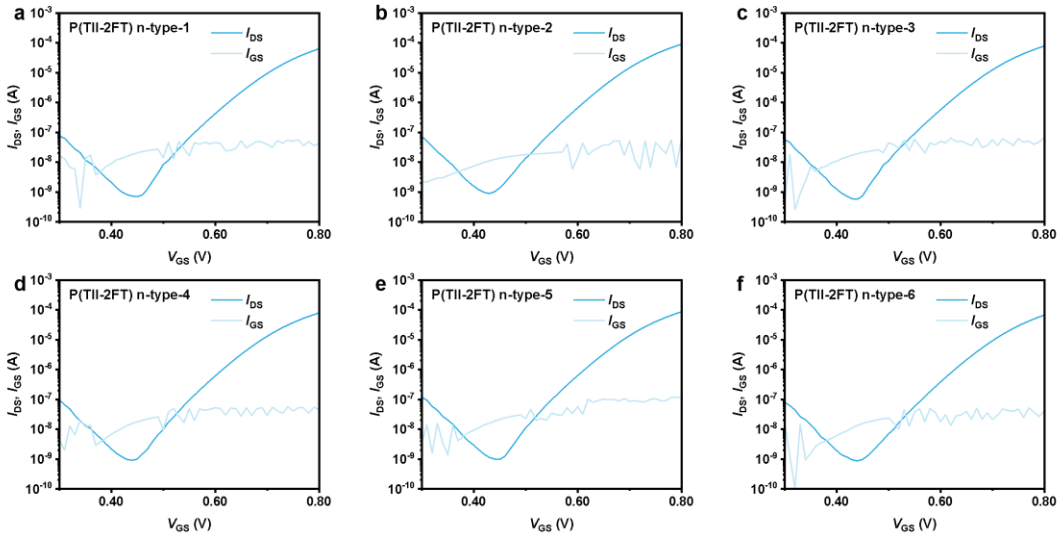

Supplementary Fig. 21 Six typical n-type OECT transfer characteristics based on P(TII-2FT) before GPC fractionation. The dark line indicates the source-drain current, and the light line indicates the leakage current of the gate.

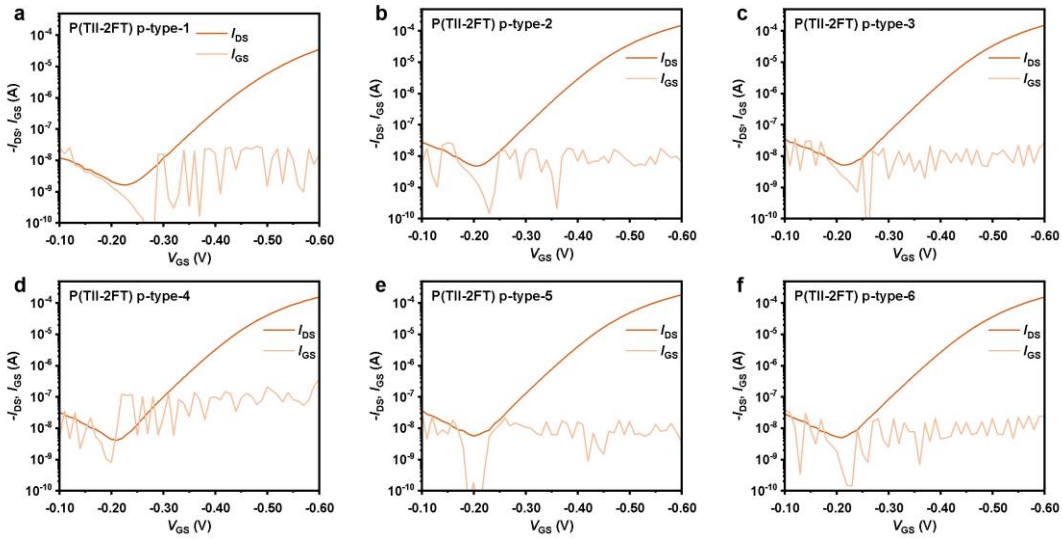

Supplementary Fig. 22 Six typical p-type OECT transfer characteristics based on P(TII-2FT) before GPC fractionation. The dark line indicates the source-drain current, and the light line indicates the leakage current of the gate.

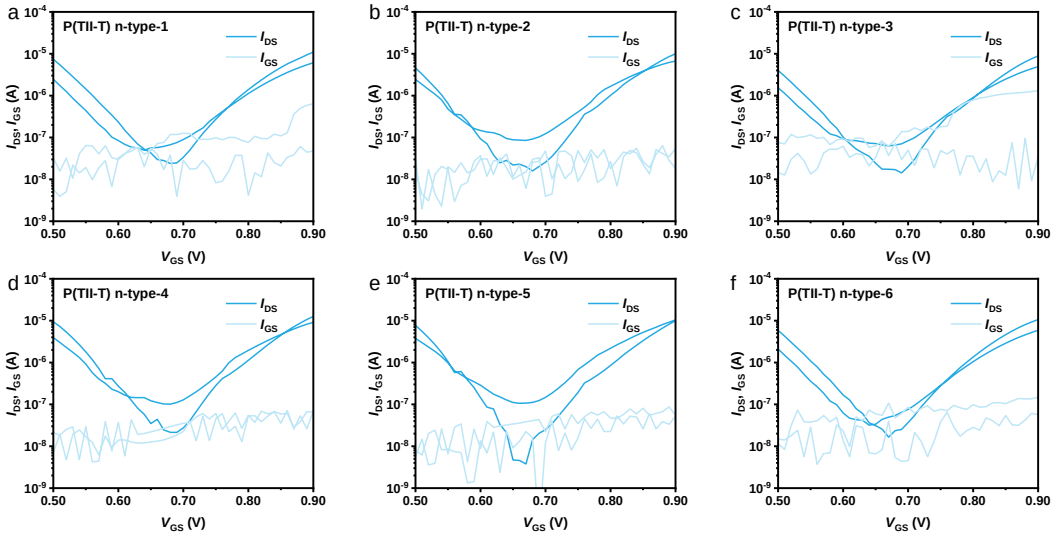

541

542 **Supplementary Fig. 23 Six typical n-type OECT transfer characteristics** based on P(TII-T)
543 before GPC fractionation. The dark line indicates the source-drain current, and the light line
544 indicates the leakage current of the gate.

545

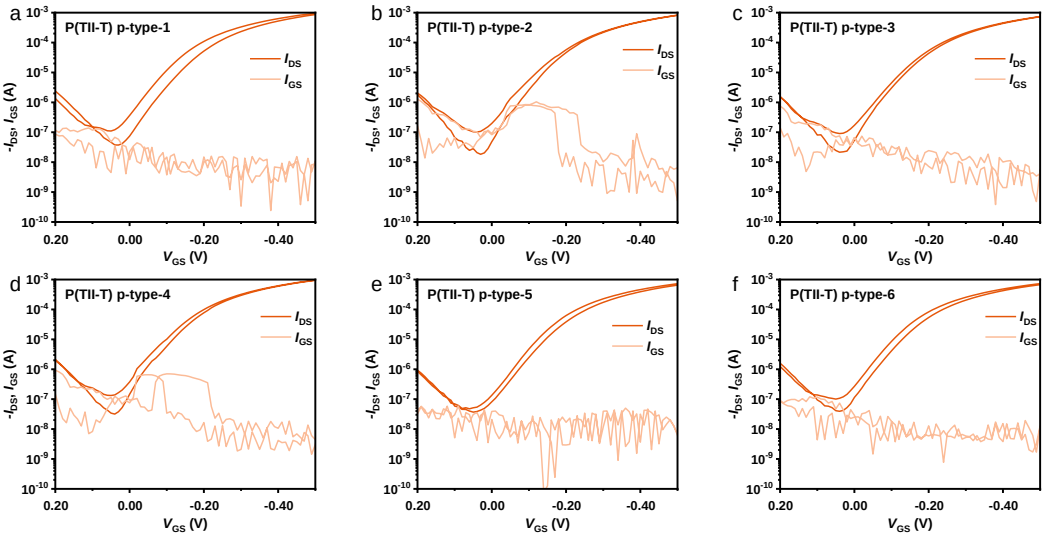

546

547 **Supplementary Fig. 24 Six typical p-type OECT transfer characteristics** based on P(TII-T)
548 before GPC fractionation. The dark line indicates the source-drain current, and the light line
549 indicates the leakage current of the gate.

550

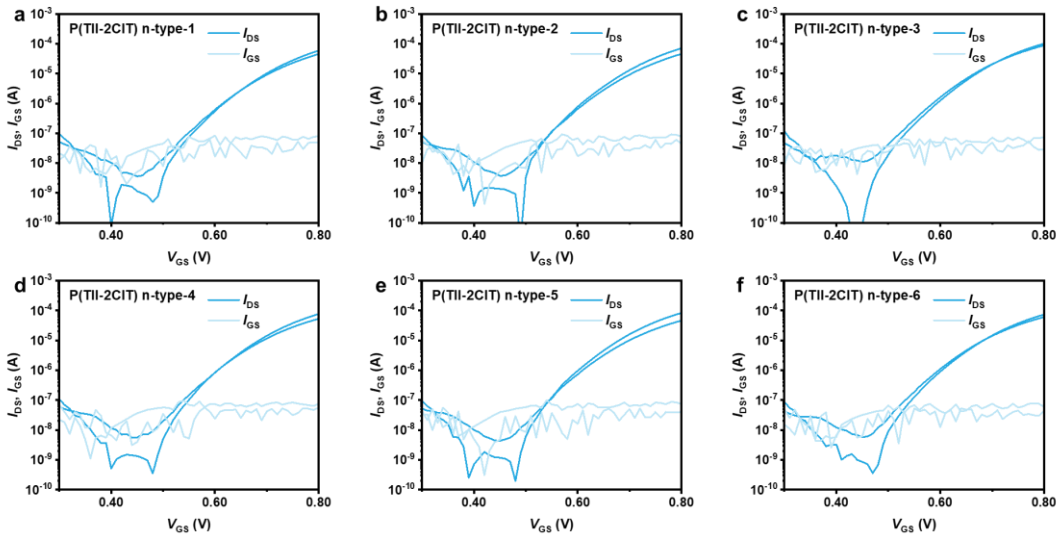

Supplementary Fig. 25 Six typical n-type OECT transfer characteristics based on P(TII-2ClT) before GPC fractionation. The dark line indicates the source-drain current, and the light line indicates the leakage current of the gate.

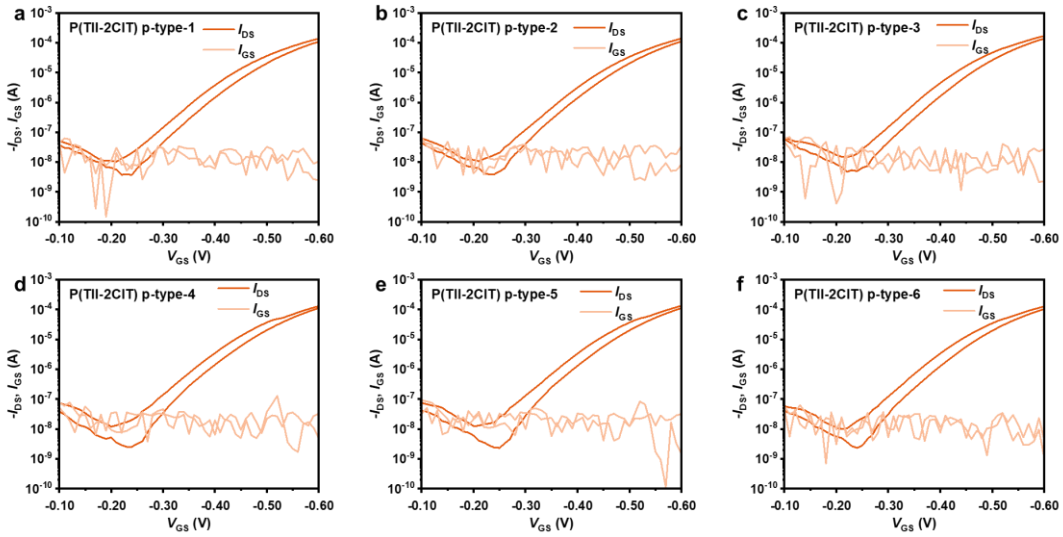

Supplementary Fig. 26 Six typical p-type OECT transfer characteristics based on P(TII-2ClT) before GPC fractionation. The dark line indicates the source-drain current, and the light line indicates the leakage current of the gate.

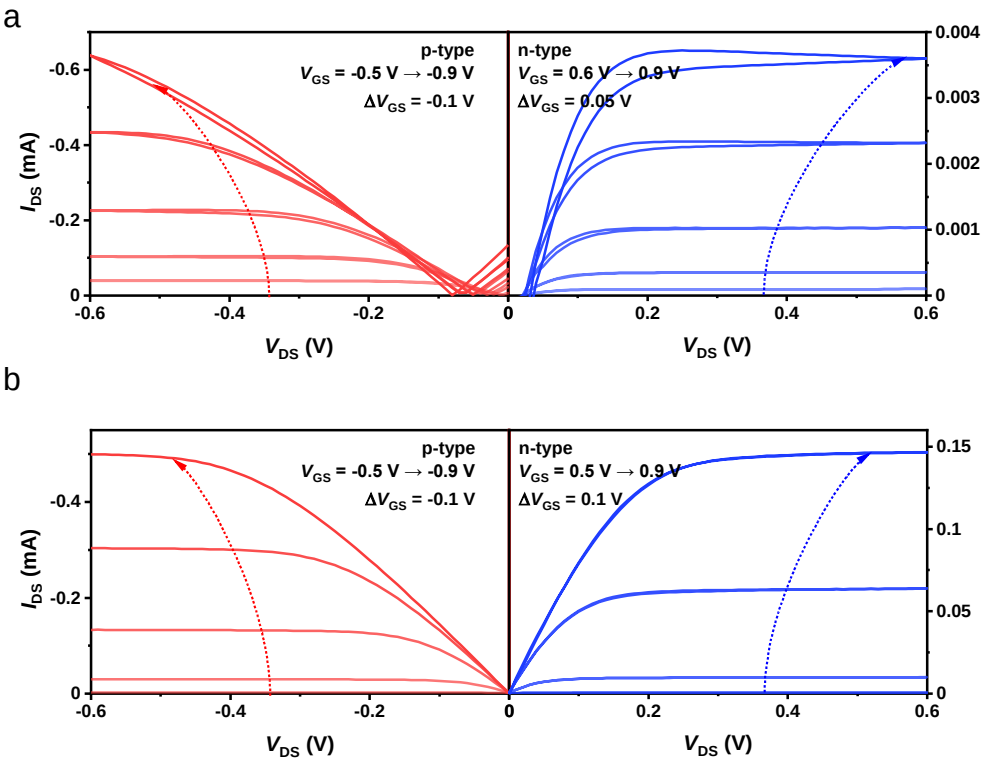

Supplementary Fig. 27 Ambipolar OECT output characteristics before GPC fractionation. a P(TII-T) and **b** P(TII-2ClT).

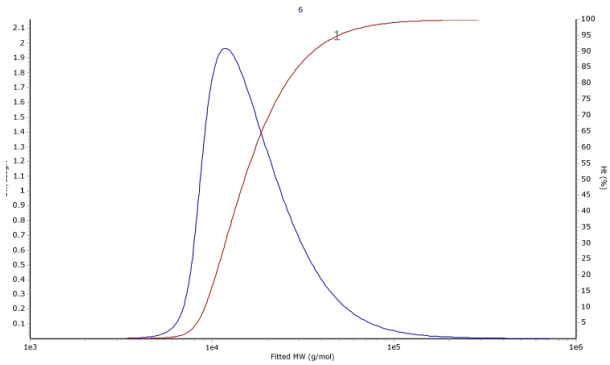

Supplementary Fig. 28 Molecular weights and PDI of purified P(TII-2FT), measured by GPC with hexafluoroisopropanol as the eluent. *Mn* = 14.7 kDa; *Mw* = 20.9 kDa; PDI = 1.42.

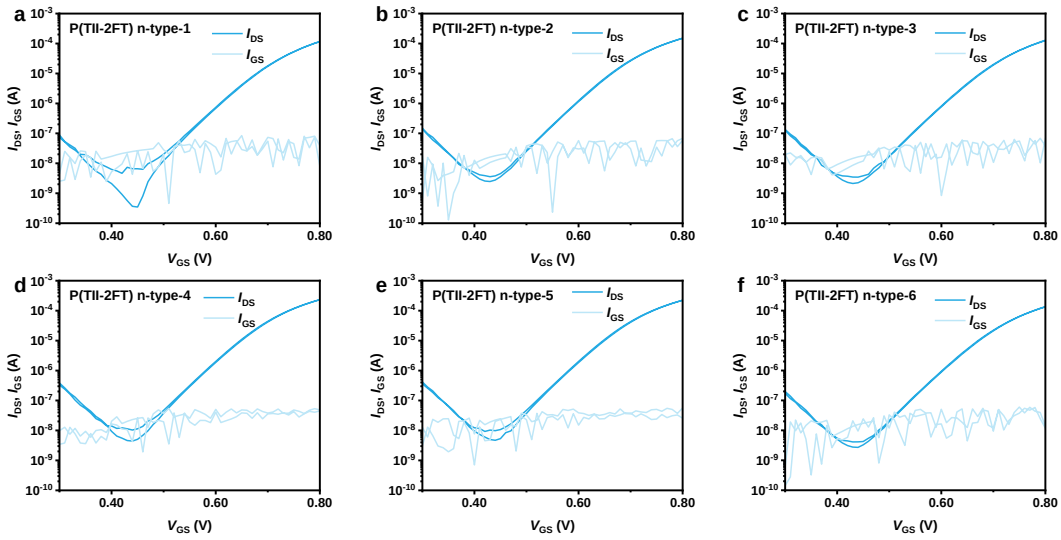

569

570 **Supplementary Fig. 29 Six typical n-type OECT transfer characteristics** based on P(TII-2FT)
571 after GPC fractionation. The dark line indicates the source-drain current, and the light line indicates
572 the leakage current of the gate.

573

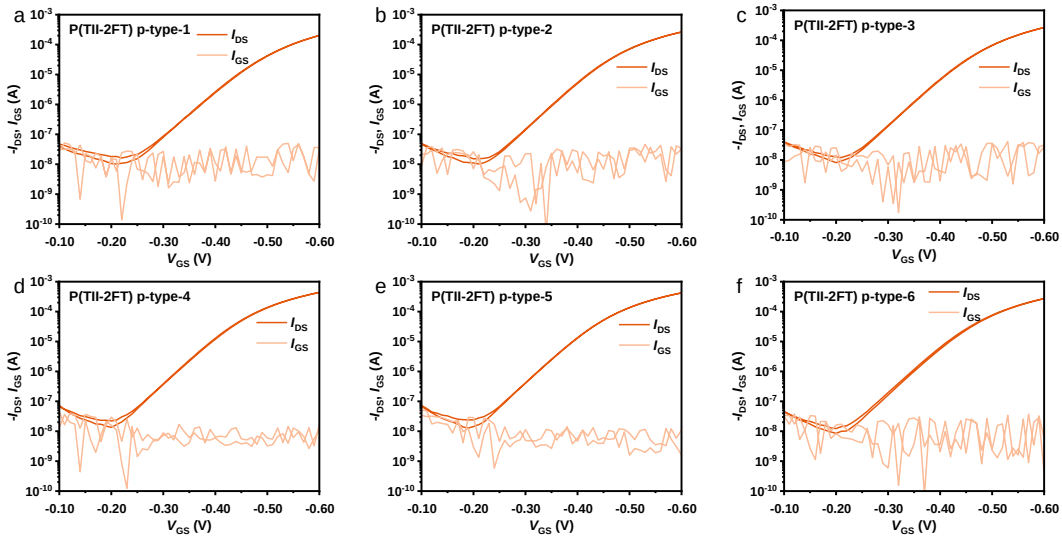

574

575 **Supplementary Fig. 30 Six typical p-type OECT transfer characteristics** based on P(TII-2FT)
576 after GPC fractionation. The dark line indicates the source-drain current, and the light line indicates
577 the leakage current of the gate.

578

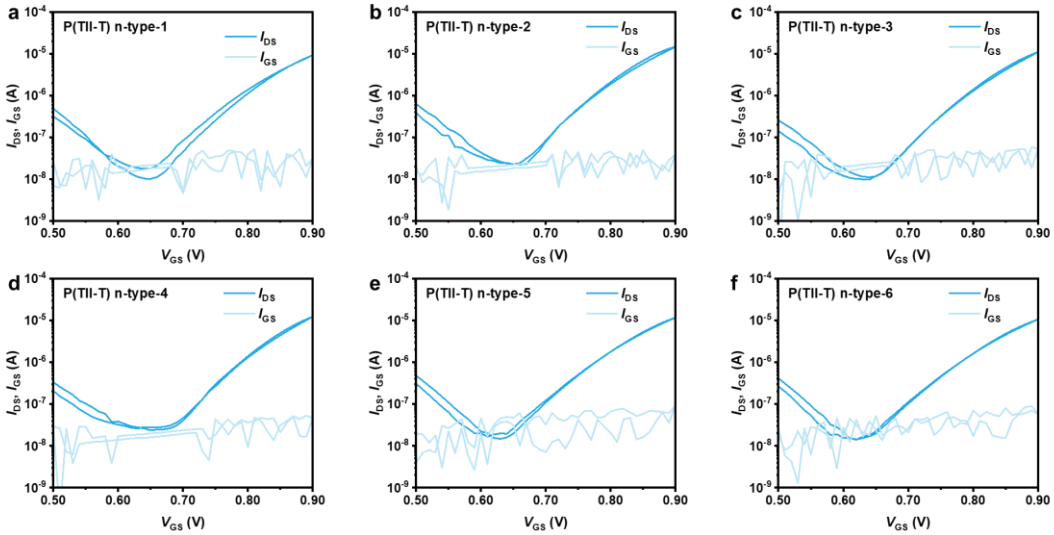

579

580 **Supplementary Fig. 31 Six typical n-type OECT transfer characteristics** based on P(TII-T) after
581 GPC fractionation. The dark line indicates the source-drain current, and the light line indicates the
582 leakage current of the gate.

583

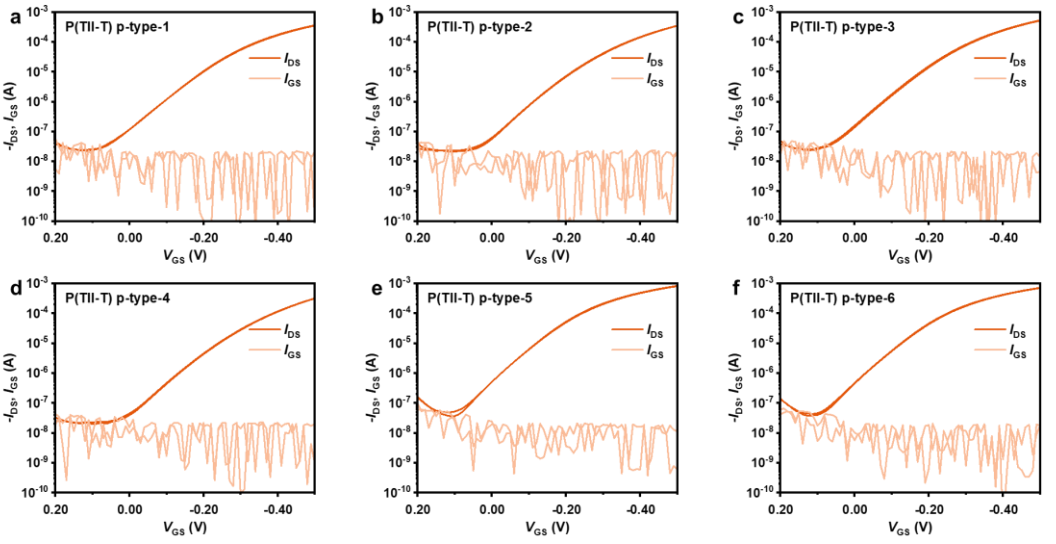

584

585 **Supplementary Fig. 32 Six typical p-type OECT transfer characteristics** based on P(TII-T) after
586 GPC fractionation. The dark line indicates the source-drain current, and the light line indicates the
587 leakage current of the gate.

588

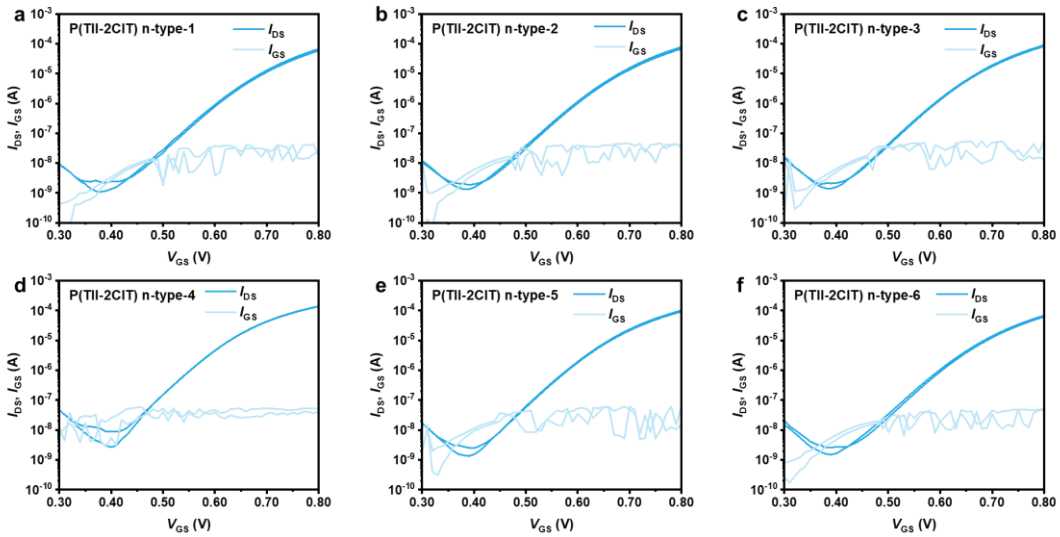

589

590 **Supplementary Fig. 33 Six typical n-type OECT transfer characteristics** based on P(TII-2ClT)
591 after GPC fractionation. The dark line indicates the source-drain current, and the light line indicates
592 the leakage current of the gate.

593

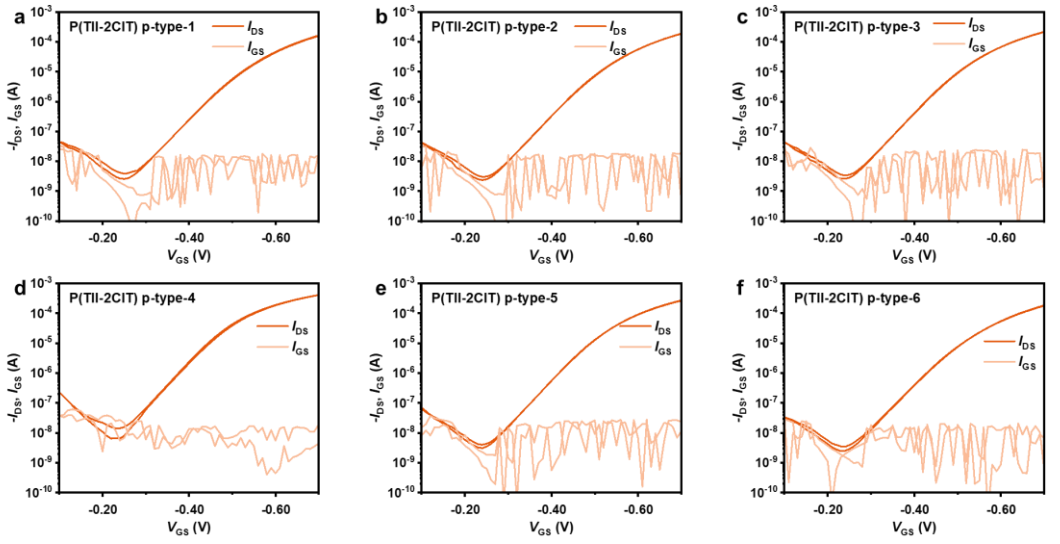

594

595 **Supplementary Fig. 34 Six typical p-type OECT transfer characteristics** based on P(TII-2ClT)
596 after GPC fractionation. The dark line indicates the source-drain current, and the light line indicates
597 the leakage current of the gate.

598

599 After examining the gate current data form all the transfer characteristics (Supplementary Fig.

21-26 and Supplementary Fig. 29-34), we affirm that the leakage current does not contribute to the transfer characteristics and quality factor of the devices.

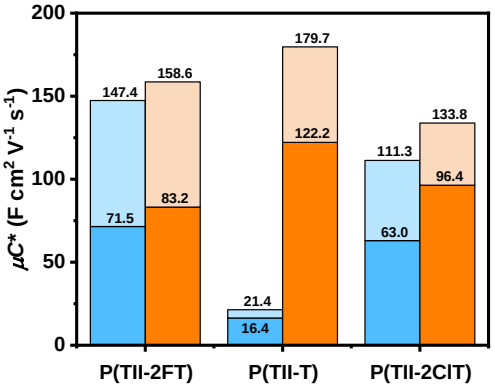

Supplementary Fig. 35 Comparison of OECT performance before and after GPC fractionation. Blue and orange represent the n-type and p-type OECT performance, respectively. Dark colors indicate original performance, while light colors indicate elevated performance after GPC fractionation.

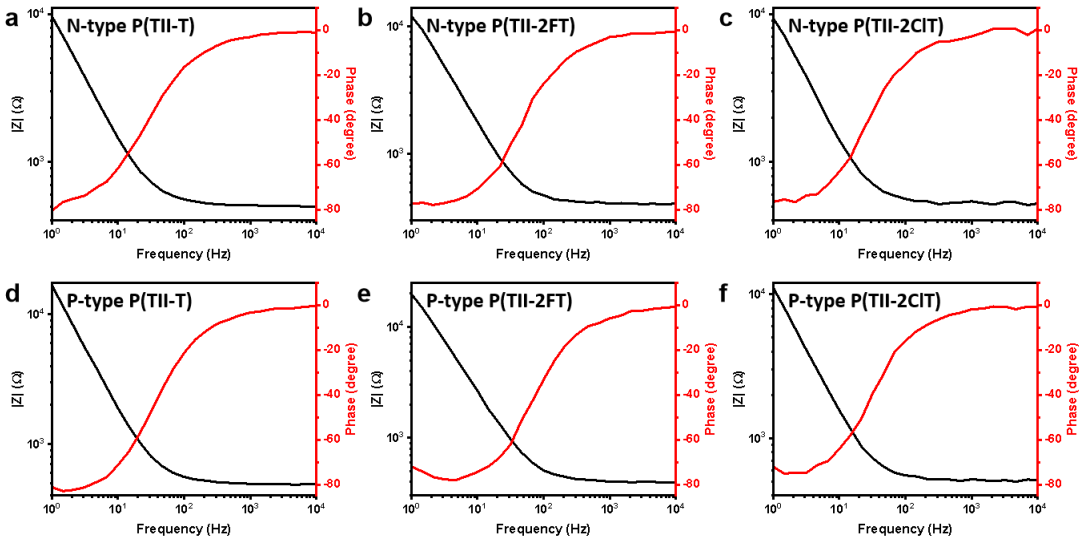

Supplementary Fig. 36 Electrochemical impedance spectrum (EIS). a/d P(TII-T), **b/e** P(TII-2FT), and **c/f** P(TII-2ClT). $|V_{DC}|$ = 0.8 V.

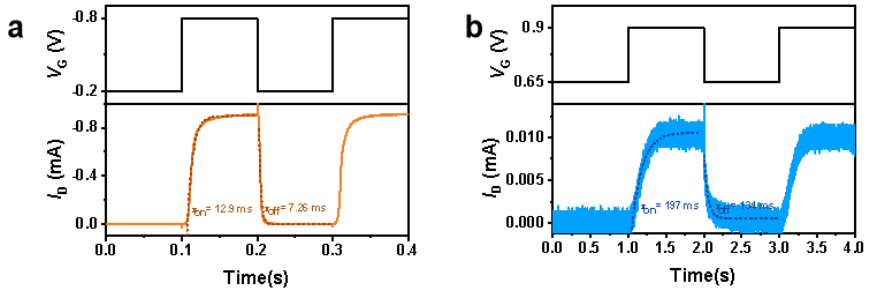

612

613 **Supplementary Fig. 37 Response time measurements for P(TII-T)**. **a** P-type and **b** n-type. $|V_{DS}|$

614 = 0.6 V.

615

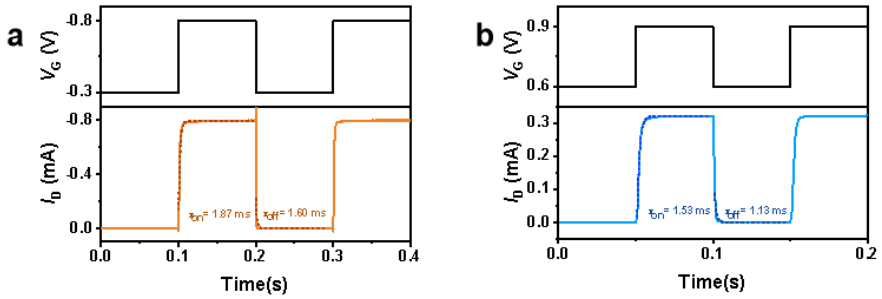

616

617 **Supplementary Fig. 38 Response time measurements for P(TII-2ClT)**. **a** P-type and **b** n-type.

618 $|V_{DS}|$ = 0.6 V.

619

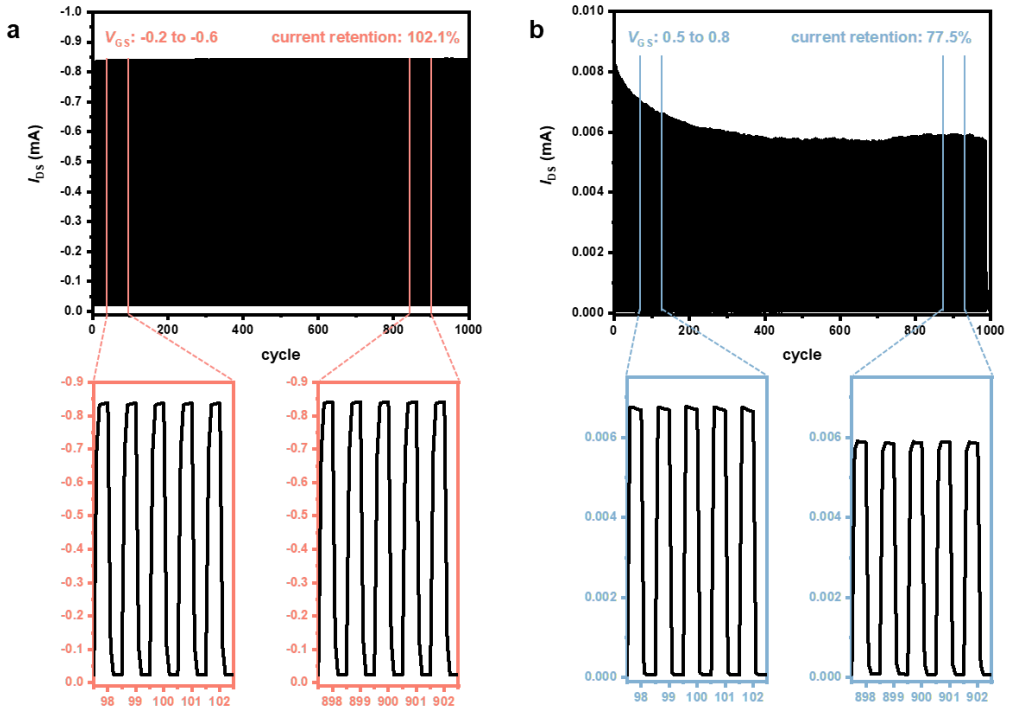

620

Supplementary Fig. 39 Regime stability tests for P(TII-T). **a** P-type and **b** n-type. V_{DS} = -0.6 V.

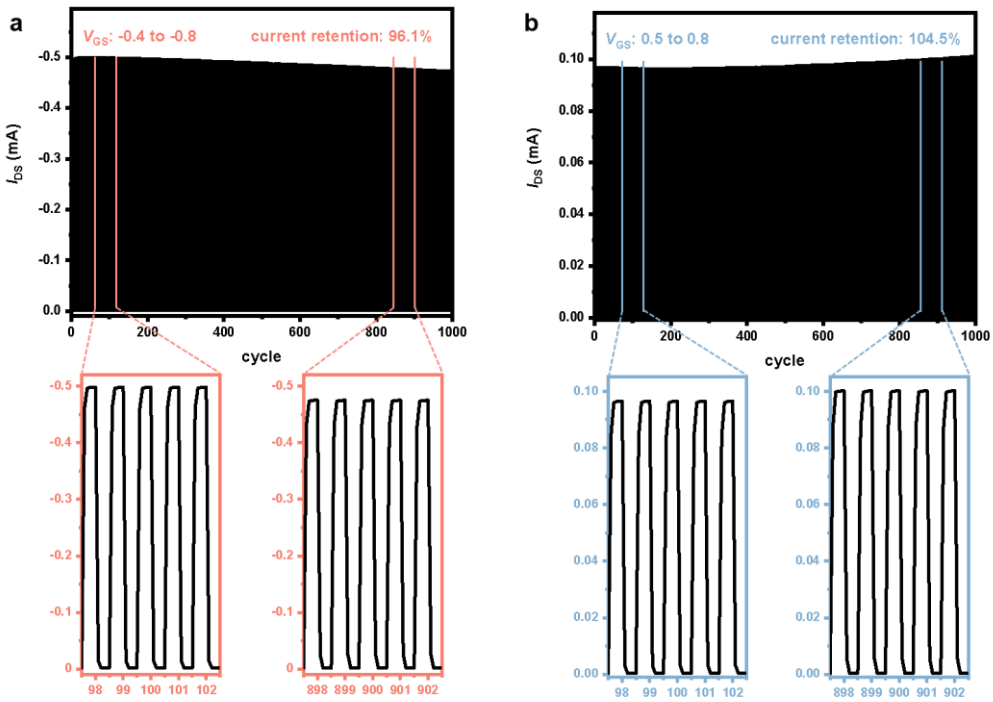

Supplementary Fig. 40 Regime stability tests for P(TII-2FT). **a** P-type and **b** n-type. V_{DS} = -0.6 V.

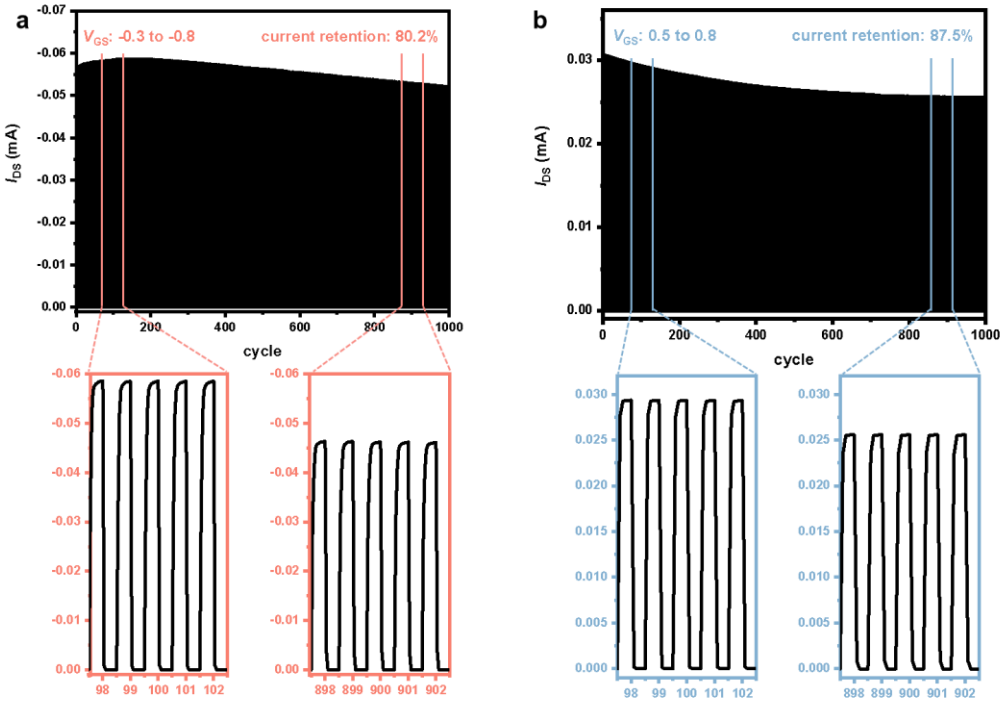

Supplementary Fig. 41 Regime stability tests for P(TII-2ClT). **a** P-type and **b** n-type. V_{DS} = -0.6 V.

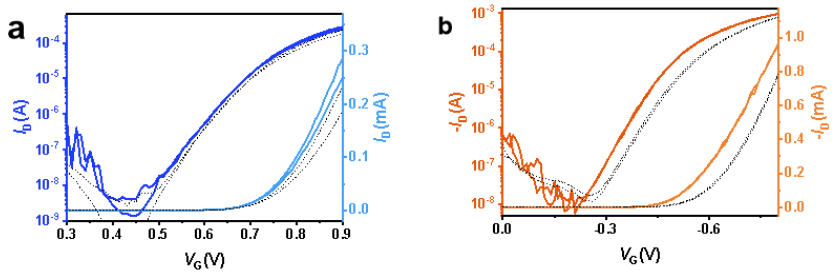

Supplementary Fig. 42 Transfer characteristics based on TII-2FT. **a** N-type and **b** p-type. The black dotted lines represent the transfer characteristics of the device exposed to undried air for 81 days, while the colorful lines represent the original transfer characteristics for comparison.

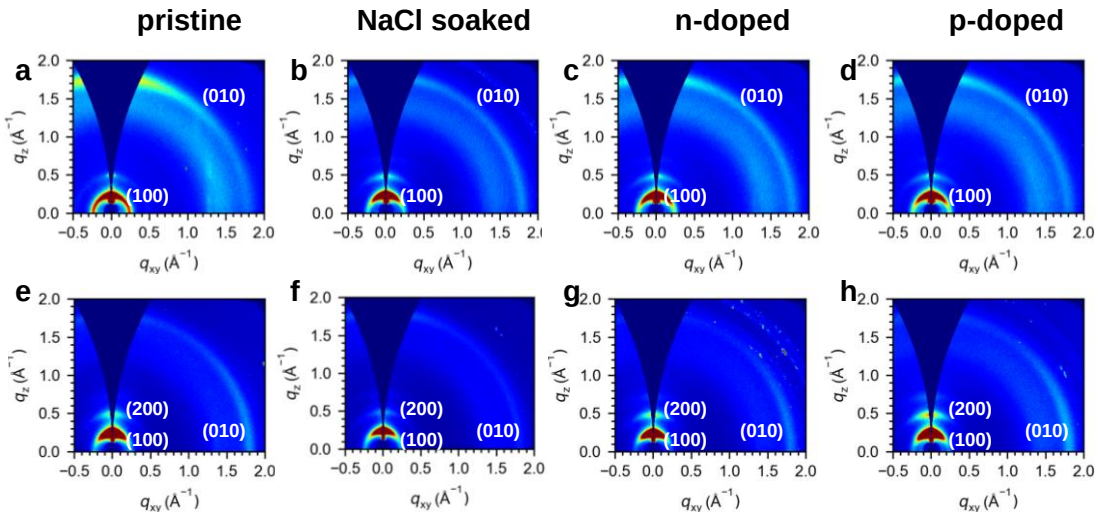

Supplementary Fig. 43 2D-GIWAXS patterns of P(TII-T)/P(TII-2FT) films. a/e Pristine, **b/f** immersed in a 0.1 M NaCl solution, **c/g** n-doped, and **d/h** p-doped processes. The p-doped/n-doped processes stand for the films on the silicon substrate that are oxidized/reduced by the 0.8/–0.8 V voltage bias for 10 min.

Pristine P(TII-2FT) and P(TII-2ClT) films exhibit strong (010) diffractions in the q_{xy} orientation and (100) diffractions in the q_z orientation, indicating a dominant edge-on packing in the film (Supplementary Fig. 43e and Supplementary Fig. 46a). Conversely, the P(TII-T) film displays circular (100) and (010) diffraction signals ranging from q_z to q_{xy} orientation, indicating the coexistence of both edge-on and face-on packing (Supplementary Fig. 43a). Upon immersion in a 0.1 M NaCl solution, both P(TII-2FT) and P(TII-T) films in the (100) and (010) orientations display

decreased crystallinity compared to their pristine films (Supplementary Fig. 43b, f), corroborated by the reduction in their corresponding coherence lengths (CLs) (Supplementary Fig. 44 and Supplementary Table 8). When p-doped or n-doped, P(TII-T) films exhibit further diminished crystallinity, while those of P(TII-2FT) films display slightly enhanced crystallinity. These trends are also observed in AFM height images. Pristine P(TII-2FT) and P(TII-2ClT) films possess smooth surfaces with fiber-like textures (Supplementary Fig. 45e and Supplementary Fig. 46c), and the root-mean-square (RMS) roughness of P(TII-2FT) films subjected to p-doped/n-doped processes is slightly higher than that of the pristine films (Supplementary Fig. 45g, h), suggesting a stronger crystallization feature after doping. However, the RMS roughness of the doped P(TII-T) films displays an opposite trend (Supplementary Fig. 45c, d). Better crystallinity and minimal morphology change might explain the high charge carrier mobility and good stability of P(TII-2FT) after doping.

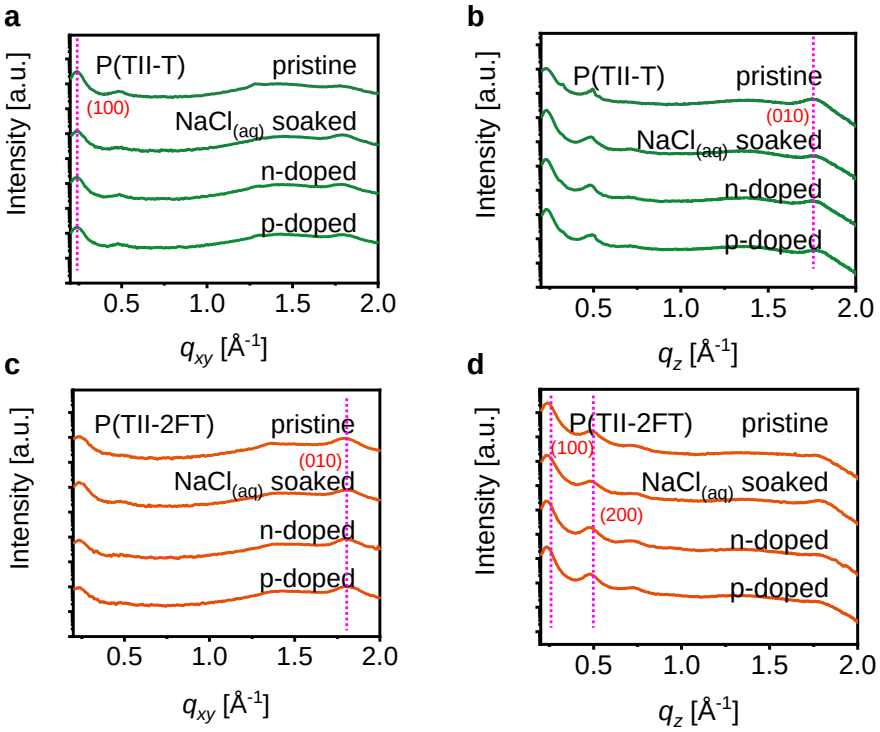

Supplementary Fig. 44 The q_{xy} orientation (in plane) line-cuts and q_z orientation (out of plane) line-cuts. **a & b** P(TII-T) and **c & d** P(TII-2FT), with the different treated processes.

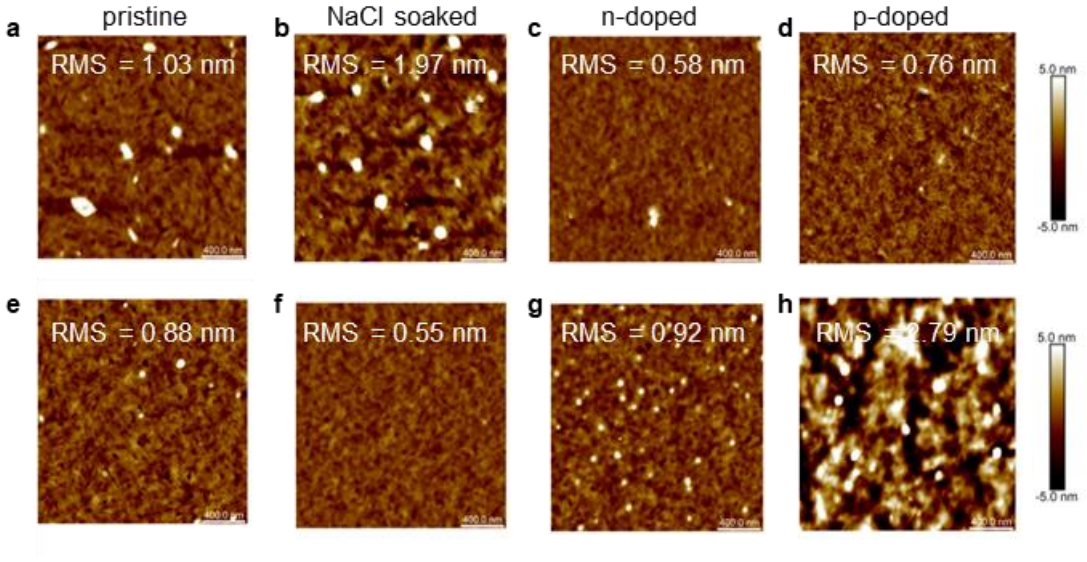

Supplementary Fig. 45 AFM height images of P(TII-T)/P(TII-2FT) films. a/e Pristine, **b/f** immersed in a 0.1 M NaCl solution, **c/g** n-doped, and **d/h** p-doped. The p-doped/n-doped stand for the films on the silicon substrate that are oxidized/reduced by a 0.8/–0.8 V voltage bias for 10 min.

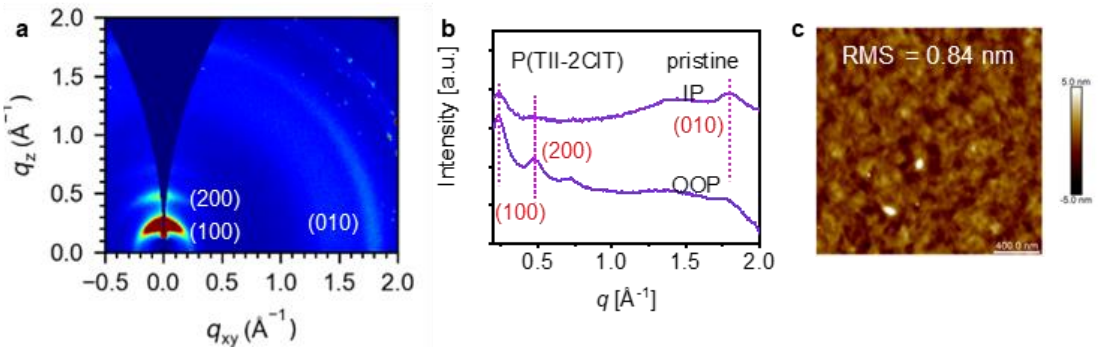

Supplementary Fig. 46 The morphology of pristine P(TII-2ClT) film. a 2D-GIWAXS pattern, **b** 1D-GIWAXS line-cuts, and **c** AFM height image. In plane (IP) stands the q_{xy} orientation, and out of plane (OOP) stands the q_z orientation.

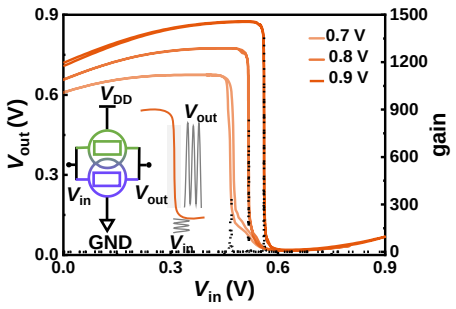

Supplementary Fig. 47 A representative voltage transfer characteristic of the inverter based on P(TII-2FT) at supply voltages, and the associated voltage gains.

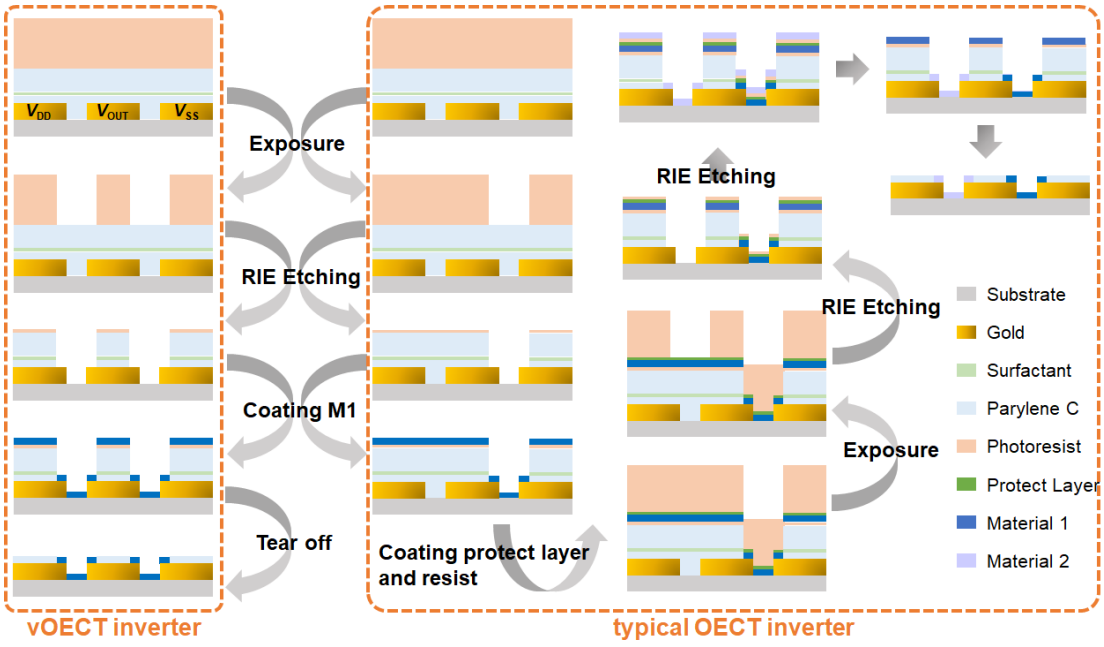

Supplementary Fig. 48 Comparison of the device fabrication processes between vertical OECT inverters based on ambipolar materials and traditional OECT inverters based on complementary p-type and n-type materials.

Regarding the advantages of ambipolar OECTs in simplifying the manufacturing process, we illustrate this in Supplementary Fig. 48. Compared to traditional OECT device structures, the ambipolar vertical OECT device structure simplifies the process from the original 9 steps (including two photolithography and two etching processes) to 4 steps (requiring only one photolithography and one etching). Additionally, the balanced ambipolar OECT performance enables the fabrication of inverters without adjusting the channel dimensions, which is generally necessary in CMOS-like device fabrication. This highlights the significant advantage of the ambipolar vertical OECT device structure in simplifying the manufacturing process.

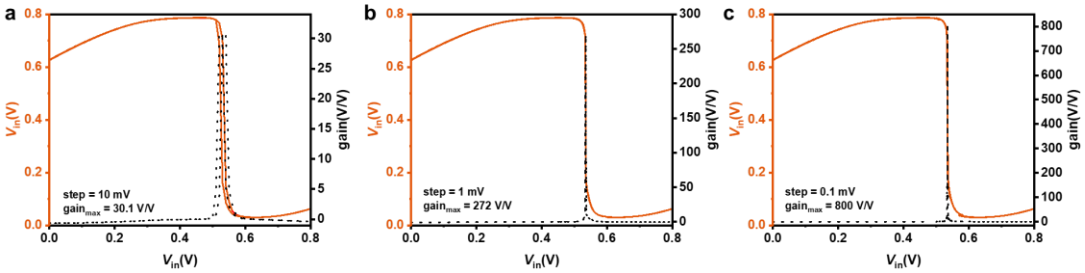

Supplementary Fig 49 The variation of the gains with voltage step size based on a P(TII-2FT) inverter. a 10 mV, **b** 1 mV, **c** 0.1 mV. Notably, the theoretical maximum gains measurable at 10 mV, 1 mV, and 0.1 mV are 40 V/V, 400 V/V, and 4000 V/V, respectively. It can be observed that the experimental gain values obtained under the testing conditions of 10 mV and 1 mV closely approach these theoretical values.

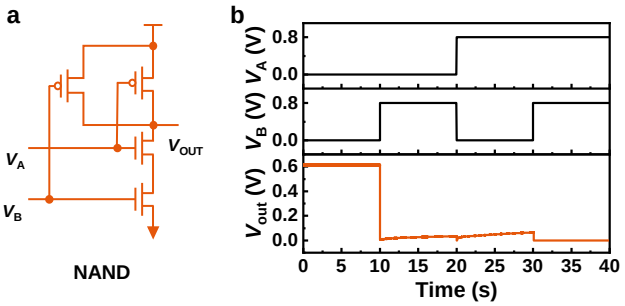

Supplementary Fig. 50 Circuit diagram and voltage input and output behavior given by the **a & b** NAND gate based on P(TII-2FT).

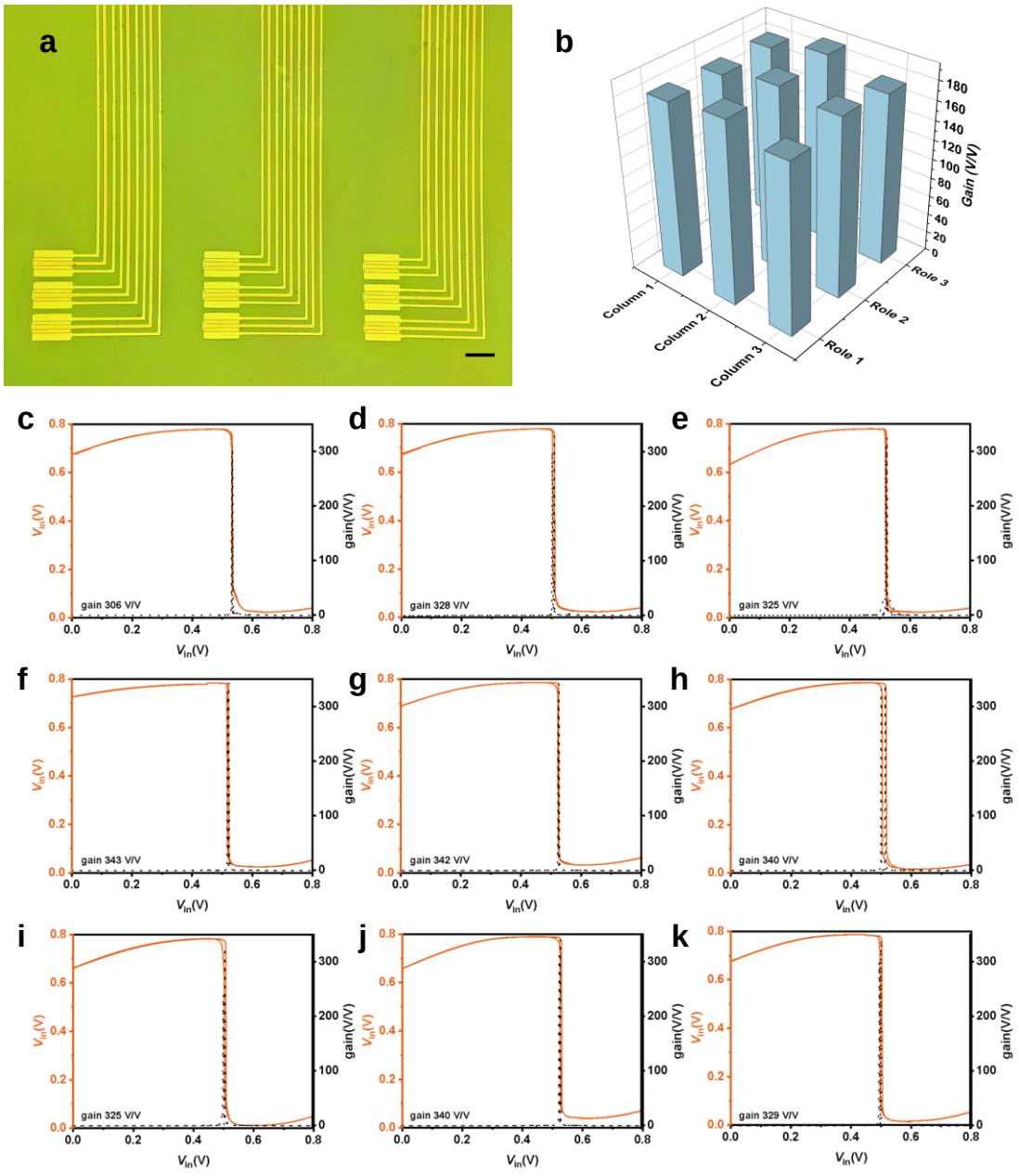

703

704 **Supplementary Fig. 51 The flexible inverter array and repetitive inverter performance based**
705 **on P(TII-2FT)**. **a** Fabricated 3×3 array for testing (scale bar: 100 μm). **b** Gain of the 3×3 vOECT
706 inverter array based on P(TII-2FT). All the inverters show very similar device performance. **c**-**k** The
707 gains of 3x3 inverter arrays based on P(TII-2FT) while V_{DD} = 0.8 V (ΔV_{IN} = 1 mV).

708

709 We successfully fabricated inverter arrays using our ambipolar material, P(TII-2FT). To
710 maximize potential array density, we omitted the wiring of transistors in the array (Fig. 4k, 4l), as
711 they can be connected from the other layer via through-holes (*Science* 373, 88-94 (2021)). Assuming

a critical dimension of 10 μm for flexible electronics, we fabricated a flexible array of 300×300 vertical OECT inverters within an area of 12 mm × 9.6 mm, demonstrating an array density of 78,125 cm^{-2} for the first time. In comparison, under the same lithography precision and channel aspect ratio (W/L = 100), the array density of traditional OECT inverters is only 1,650 cm^{-2}, about $1/50^{th}$ of the vertical OECT inverter array density. This significant difference demonstrates the immense application value of vertical OECT devices constructed with balanced, high-performance, and stable ambipolar OECT materials in enhancing device integration and reducing space occupation.

Furthermore, we would like to emphasize again that achieving high integration, small footprints, and simplified manufacturing processes is not solely dependent on the ambipolar vertical OECT device structure; it is also closely related to the high-performance, balanced, and stable ambipolar polymer P(TII-2FT). As noted by Rashid et al., the interest in vertical OECT research lies not only in designing smaller device sizes but also in achieving higher transconductance and cutoff frequencies within the same area (*Adv. Mater.* 30, 1705031 (2018); *Sci. Adv.* 7, eabh1055 (2021)). However, the generally low device performance and poor stability of currently reported ambipolar OECT materials are implementation barriers. Our proposed high-spin structure design strategy and the resulting high-performance, stable, and balanced ambipolar OECT materials address these bottleneck issues and provide a feasible path to vertical OECT devices for on-site amplification of biological signals.

To further illustrate the operability of our design strategy in enhancing device integration and reducing footprints, we fabricated a 3×3 inverter array based on the vertical OECT structure (Supplementary Fig. 51). This 3×3 inverter array demonstrated a gain of 184.5 ± 6.0 V/V with a test step size of 1 mV, exhibiting excellent performance and consistency. By further reducing the test step size to 0.1 mV, the device achieved a gain of 607.9 V/V. This slow scan rate greatly extends the testing time, generally requiring the material to have very good operational stability, a condition under which most reported materials struggle to remain stable. Using the vertical OECT device structure, Rashid et al. achieved a peak inverter gain of 28 V/V and an ECG signal amplification of 10 times with a 10 mV step size (*Sci. Adv.* 7, eabh1055 (2021)). In contrast, we achieved a peak

inverter gain of 809 V/V and an ECG signal amplification of 73 times with a 0.1 mV step size. This significant difference further demonstrates the advantage of our polymer design strategy in improving device gain and enhancing device stability, directly addressing the bottleneck issues of vertical OECT devices in practical applications.

Supplementary Fig. 52 Photograph and magnified microscope image of the thin and flexible inverters. Attached to a fragile petal.

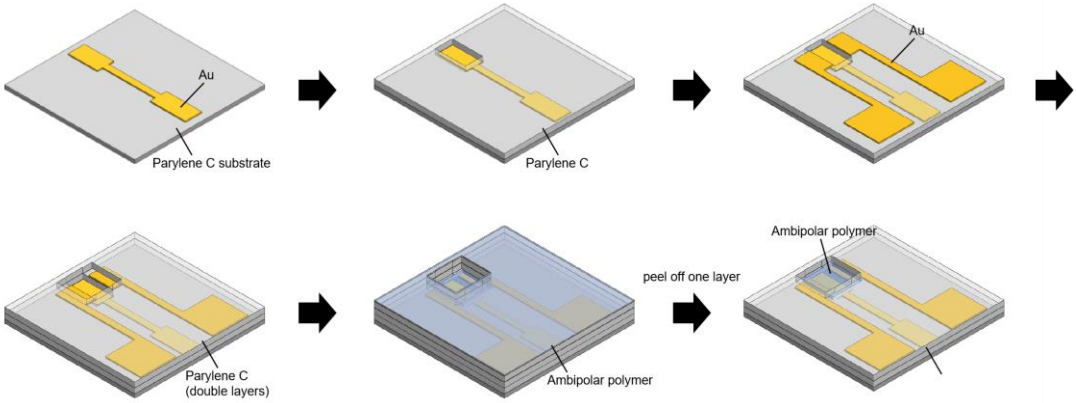

Supplementary Fig. 53 Schematic illustration of the fabrication process of the flexible amplifiers. Used for EEG, ECG, and ECoG signal recording.

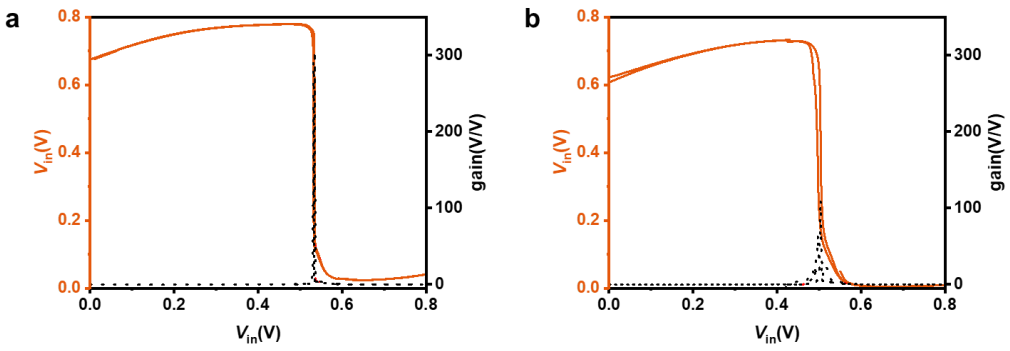

Supplementary Fig. 54 Representative voltage transfer characteristics of the inverter based on P(TII-2FT) in **a** 0.1 M NaCl solution and **b** in artificial cerebrospinal fluid (ACSF).

We prepared artificial cerebrospinal fluid (ACSF) with ion concentrations, pH value, and osmotic pressure similar to animal cerebrospinal fluid. The formulation included NaCl (147 mM), KCl (3.5 mM), NaH_2PO_4 (1 mM), $NaHCO_3$ (2.5 mM), glucose (11 mM), and freshly added suspensions of $Ca(OH)_2$ and $Mg(OH)_2$ to adjust the concentrations of Ca^{2+} (1 mM) and Mg^{2+} (1.2 mM). We tested the OECT devices in ACSF and observed a decrease in gain similar to that seen in brain tissue fluid, even under quasi-static testing conditions (Supplementary Fig. 54). The inverter we utilized exhibited a gain of 306 in a 0.1 M NaCl solution but dropped to only 111 in ACSF (with a testing step size of 1 mV), representing a decrease of 64%. Note that mouse cerebrospinal fluid contains various proteins, and this complex environment may interfere with signal capture and amplification. Therefore, for biosignal capture, factors such as solution environment and response speed (Fig. 5c) should also be considered critical to device performance.

Although the amplification factor for detecting electrocorticography (ECoG) signals in the rat brain was average, the record-high quasi-static gain of 809 based on our amplifier is still meaningful for practical applications, especially for biological signal amplification. High-gain devices are advantageous for amplifying very small biological signals. For example, biosignals from the brain include many small signals, such as local field potential (LFP, 100-500 μV), electroencephalogram (EEG, 5-300 μV), and electrocorticogram (ECoG, 50-500 μV) (*Principles of Neural Science*, New York: McGraw-Hill Health Professions Division, 2000).

In quasi-static testing, the test step size plays a crucial role. Simple mathematical calculations reveal that with a step size of 10 mV, the theoretical upper limit of the inverter gain with a V_{DD} of 0.8 V is 0.8 V / (0.01 V × 2) = 40. This value increases to 400 and 4000 at step sizes of 1 mV and 0.1 mV, respectively. For LFP measurement, the amplitude is small, usually 0.1-0.5 mV. Thus, choosing 0.1 mV as the step size is meaningful. In our device, we obtained a gain of 809 at a step size of 0.1 mV, which is still lower than the theoretical value (4000). However, with a larger step size, the inversion point cannot be found precisely, and we cannot accurately measure the real gain values for small signals, such as LFP. Therefore, to fully characterize the capability of an inverter, quasi-static gain measurement is necessary.

From the gain curve, higher gains correspond to larger magnification and smaller detection ranges. This is why we stress that high-gain devices are advantageous in small signal sensing. This

786 also raises another issue: according to the calculations above, even if the influence of signal
787 frequency is ignored, signals such as electrocardiogram (ECG) signals, which exceed 1 mV, may
788 not fully utilize the quasi-static gain. However, obtaining a 73-fold increase in the ECG signal, as
789 achieved in our work, amplifies a 1 mV signal to 73 mV, which is already a very good amplification
790 value. Therefore, this gain can be considered successful, even though it did not reach the maximum
791 value of 809 V/V. Based on our tests with a 1 mV step, the gain exceeded 200 V/V, and considering
792 the influence of signal frequency on the gain, this result is quite significant.

793 In the sensing test shown in Fig. 5e-f, we achieved a lower gain. Throughout long-term
794 experiments, we observed a significant impact of input signal frequency on gain. As depicted in Fig.
795 5c, a continuous increase in frequency diminishes the gain of the inverter. However, this
796 phenomenon is not exclusive to OECTs; it is present in many other types of transistors, including
797 well-established inorganic transistors (*Microelectron. Eng.* 216, 111054 (2019); *Adv. Funct. Mater.*
798 32, 2205129 (2022); *npj Flexible Electron.* 7, 38 (2023)). Quasi-static gain is a foundation, and
799 during testing, we observed that the actual signal magnification is also larger. This observation is
800 confirmed by other works. For example, a quasi-static gain of over 700 yields 50 times ECG signal
801 amplification (*Adv. Funct. Mater.* 32, 2205129 (2021)). As a reference, we obtained a 73-fold
802 magnification with an 809 quasi-static gain. A quasi-static gain of 28 results in a 10-fold ECG signal
803 amplification (*Sci. Adv.* 7, eabh1055 (2021)). Notably, they used a 10 mV step size. However, we
804 think that they should measure their device at a smaller step size to more accurately evaluate their
805 inverter performance.

806 We would like to point out that some papers did not report quasi-static gains because their
807 devices may not be stable enough. Quasi-static testing with small steps can serve as an important
808 indicator of inverter stability. In inverter testing, we must use small step testing to accurately
809 estimate the amplification capability of an inverter for small signals. In various practical
810 measurements based on complementary logic circuits, we observed that when the stability of OECT
811 devices is poor, it is difficult to complete quasi-static testing with small steps, since the quasi-static
812 measurement requires a considerable amount of time. In biological signal amplification, the stability
813 of an amplifier is crucial, as it directly determines the lifespan of the amplifier and the reliability of
814 data acquisition.

815 In summary, the quasi-static gain is important for biological signal amplification for the

following reasons:

(1) The value of the quasi-static gain can be used to determine the suitable operating scenarios for an inverter. Smaller measurement steps indicate the amplification capability for small signals. For brain signals, our measurement step of 0.1 mV is meaningful.

(2) Quasi-static gain can serve as an upper limit for actual amplification performance. The gain decrease at high scan frequencies and other environmental factors is also based on the quasi-static gain.

(3) The quasi-static gain also reflects the overall operational stability of an inverter.

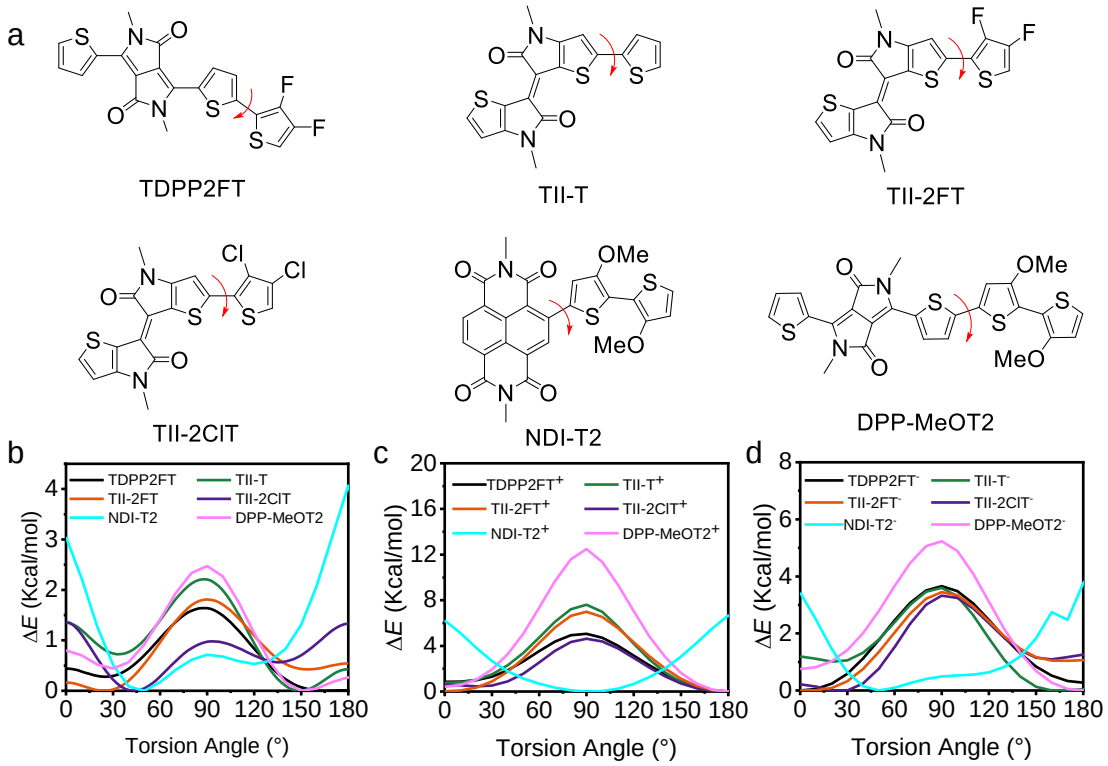

Supplementary Fig. 55. Relaxed PES scans. a Chemical structures of the six monomers: TDPP2FT, TII-T, TII-2FT, TII-2ClT, NDI-T2, and DPP-MeOT2. Comparison of the relaxed PES scans of the torsion angles for the monomers under **b** neutral, **c** positively, and **d** negatively charged states. The torsion angles are the dihedral angles marked in Supplementary Fig. 55a. The EG side chains were replaced with methyl groups to simplify the calculation.

The dominant conformation of the monomers TDPP2FT, TII-T, TII-2FT, TII-2ClT, and DPP-MeOT2 in the positively and negatively charged states shows good planarity, whereas NDI-T2 displays a twisted backbone, particularly in the positively charged state.

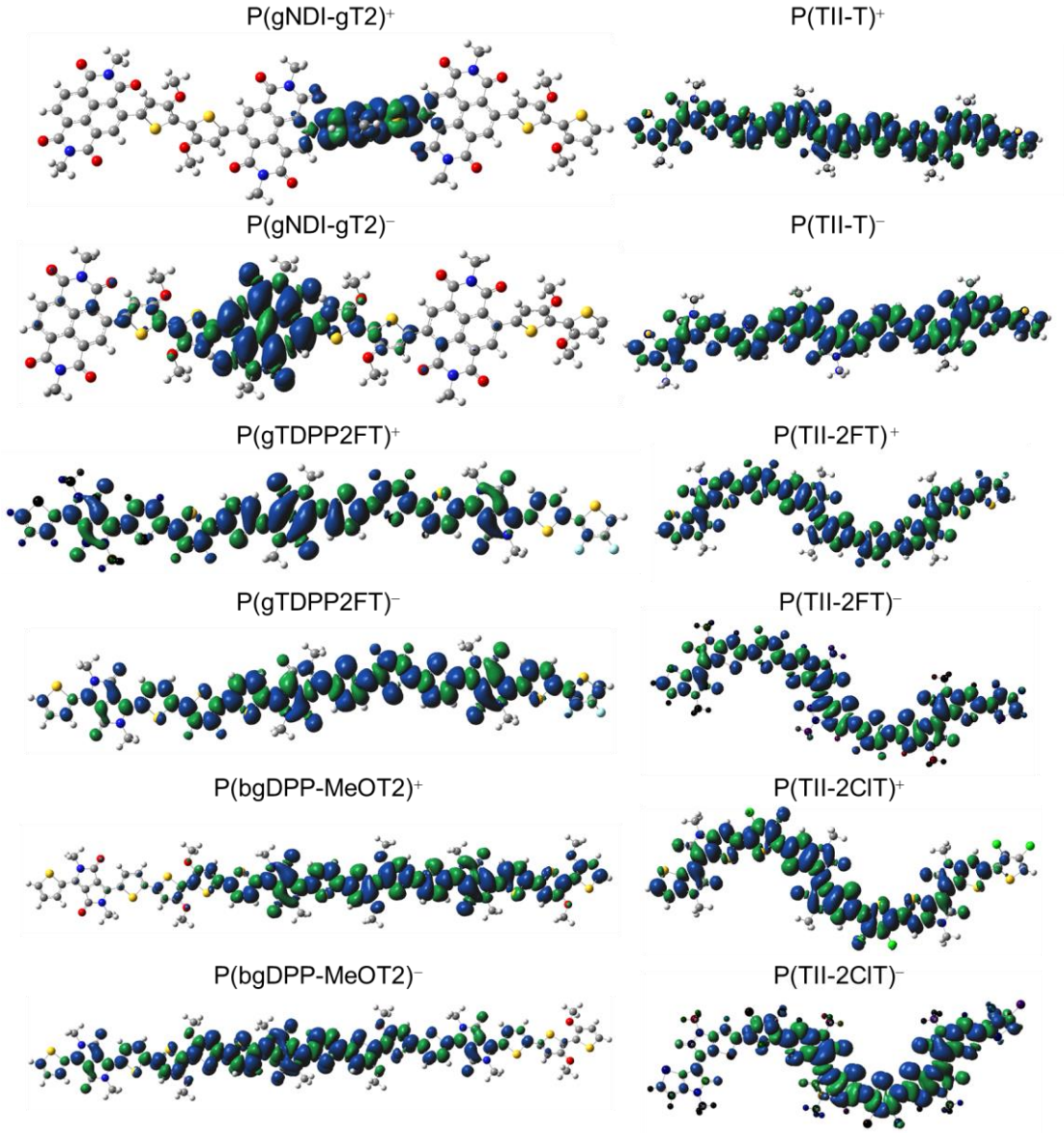

Supplementary Fig. 56 Spin density distribution of positively or negatively charged trimers. P(gNDI-gT2), P(gTDPP2FT), P(bgDPP-MeOT2), P(TII-T), P(TII-2FT), and P(TII-2ClT).

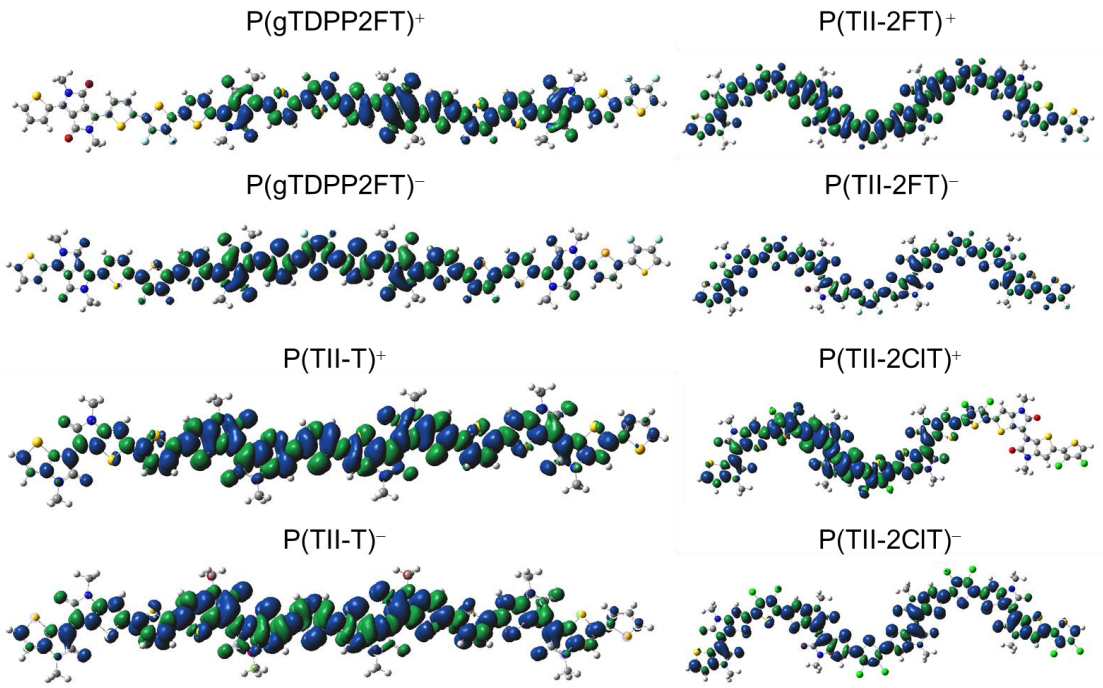

Supplementary Fig. 57 Spin density distribution of positively or negatively charged tetramers. P(gTDPP2FT), P(TII-T), P(TII-2FT), and P(TII-2ClT).

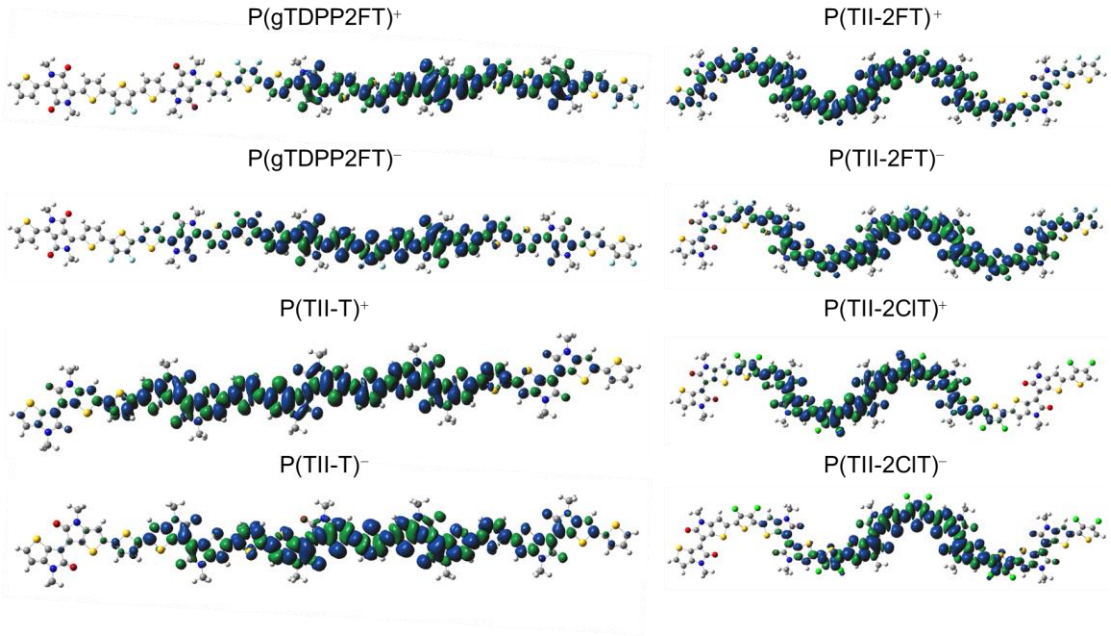

Supplementary Fig. 58 Spin density distribution of positively or negatively charged pentamers. P(gTDPP2FT), P(TII-T), P(TII-2FT), and P(TII-2ClT).

In positively or negatively charged trimers, P(gTDPP2FT), P(TII-T), P(TII-2FT), and P(TII-2ClT) all demonstrate excellent delocalization characteristics (Supplementary Fig. 56). However, in

P(bgDPP-MeOT2) and P(gNDI-gT2), the positive or negative charges cannot fully delocalize throughout the entire backbone, especially in P(gNDI-gT2), which exhibits a strong localization effect in its spin density distribution (Supplementary Fig. 56). These observations imply their weak charge transport abilities. In positively or negatively charged tetramers, the spin density in P(gTDPP2FT) concentrates in the core region of the backbone, whereas due to their high-spin characteristics, P(TII-T), P(TII-2FT), and P(TII-2ClT) display completely delocalized spin density distributions (Supplementary Fig. 57). Additionally, in P(TII-2ClT), there is a lower positive charge distribution at the end of the tetramer (Supplementary Fig. 57), possibly influenced by the pronounced twist in the configuration of P(TII-2ClT). This observation is more apparent in pentamers (Supplementary Fig. 58). Overall, compared to the closed-shell polymer P(gTDPP2FT), the three TII-based high-spin polymers with high-spin structures exhibit a more delocalized distribution of spin density.

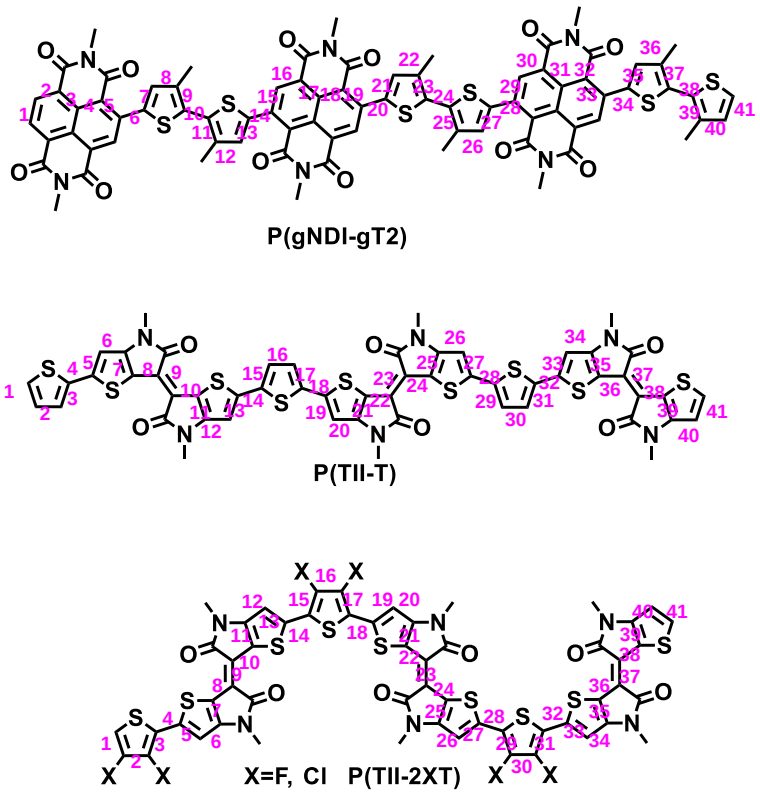

Supplementary Fig. 59 Schematic diagram of single bond and double bond from index 1 to index 41 along the polymer backbones for P(gNDI-gT2), P(TII-T), P(TII-2FT), and P(TII-2ClT)**.**

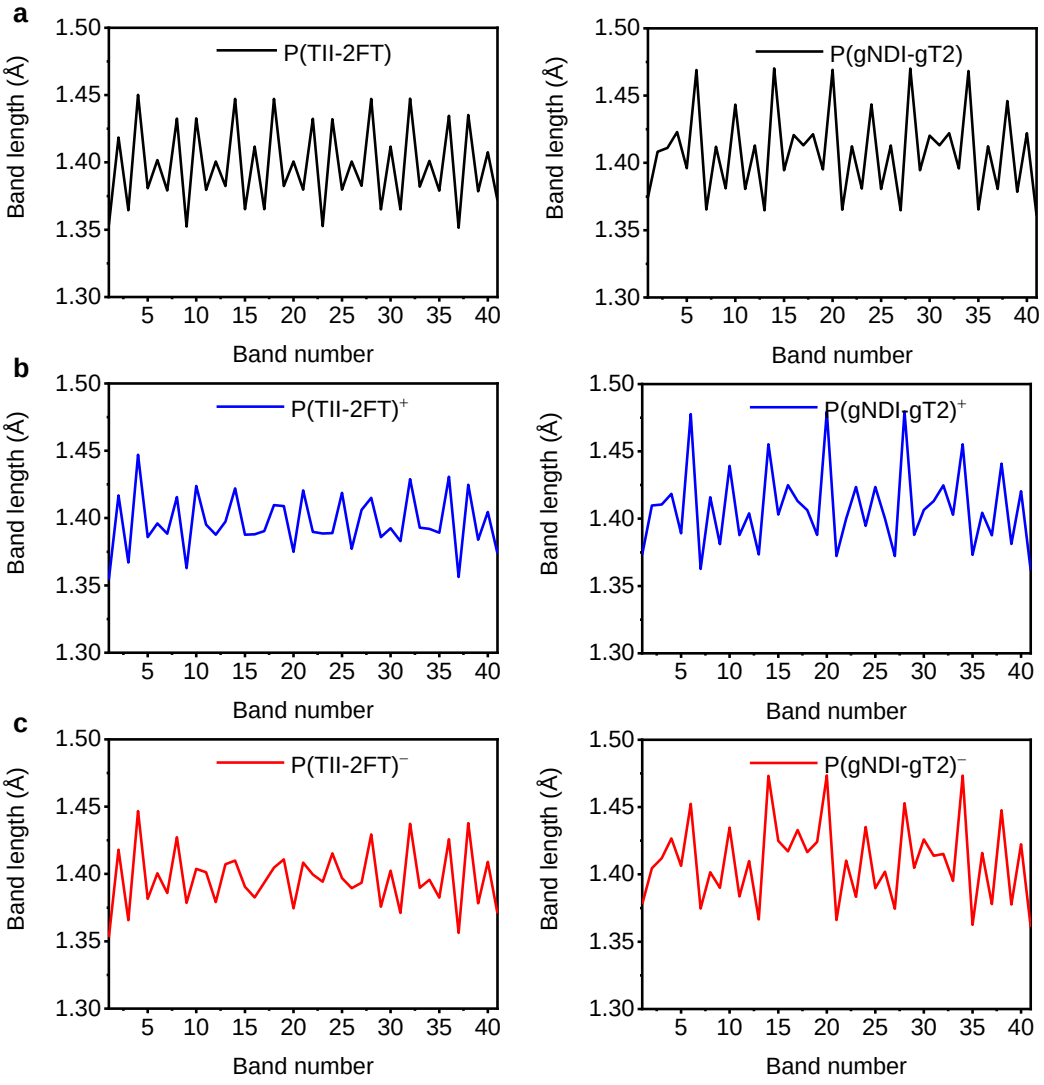

867

868 **Supplementary Fig 60. Comparison of the bond length alternation (BLA)**. P(TII-2FT) and
869 P(gNDI-gT2), from the number 1 to the number 41 under the **a** neutral, **b** positively, and **c** negatively
870 charged states.

871

872 Compared to P(gNDI-gT2), P(TII-2FT) exhibits a more uniform BLA in both neutral and
873 positively/negatively charged states, suggesting that P(TII-2FT) has a lesser disparity between
874 single and double bonds, a typical feature of high-spin conjugated polymers. Besides, the calculated
875 ΔE_{ST} of the P(gNDI-gT2) trimer is −21.22 kcal/mol, much lower than that of P(TII-2FT) (−11.32
876 kcal/mol). This further suggests that, compared to the high-spin polymer P(TII-2FT), P(gNDI-gT2)
877 is more likely to have a closed-shell structure. With its high-spin nature, P(TII-2FT) possesses
878 enhanced backbone rigidity and planarity compared to the conventional closed-shell structure
879 P(gNDI-gT2), especially in doped states, thereby facilitating charge delocalization and transport

after heavily doping.

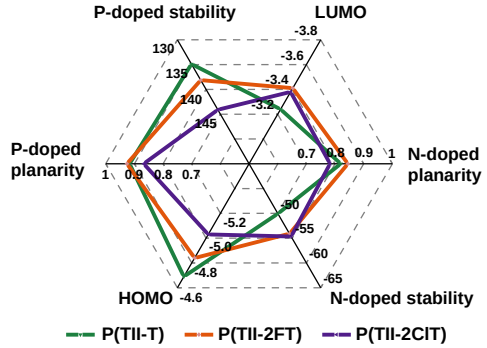

Supplementary Fig 61. Comparison of the six important parameters of the three ambipolar high-spin polymers. P(TII-T), P(TII-2FT), and P(TII-2ClT).

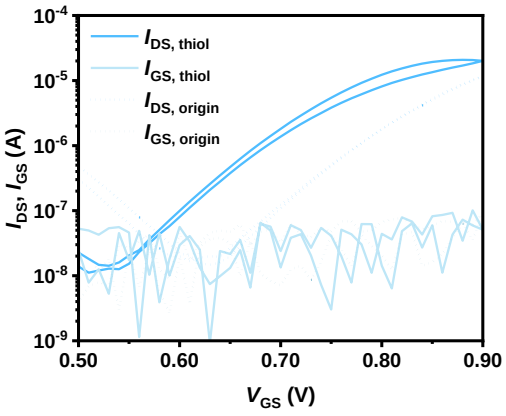

Supplementary Fig. 62 N-type transfer characteristics of the P(TII-T) OECT devices before (solid line) and after (dotted line) benzyl mercaptan modification. The modified transfer characteristics show a significant increase in the on-current and a decrease in the threshold voltage.

We attempted to experimentally demonstrate that the weak n-type OECT performance of P(TII-T) originates from poor electron injection from the electrode. We modified the gold source and drain electrodes using benzyl mercaptan to lower the electrode work function. Consequently, the n-type OECT performance of P(TII-T) improved, with an increased on-current and a smaller V_{th} (Supplementary Fig. 62). This result supports our assumption that the unmatched LUMO energy level of P(TII-T) impedes efficient electron injection, consistent with the results shown in the radar chart (Supplementary Fig. 61).

In conclusion, despite its ability to accept electrons due to its high-spin nature, the unmatched molecular energy levels of P(TII-T) upon n-type doping hinder efficient electron injection and transport. Thus, P(TII-T) does not exhibit ideal n-type OECT performance.

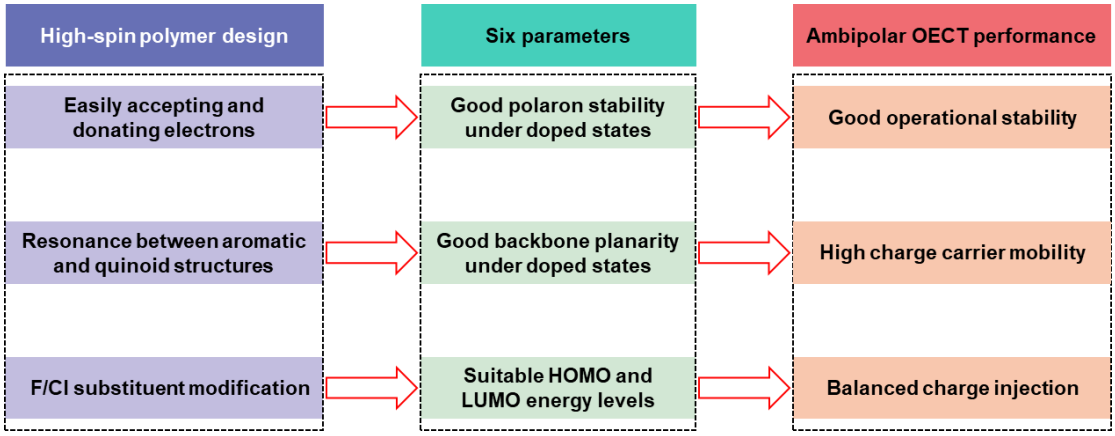

Supplementary Fig. 63 Schematic illustration of the relationship among the polymer's spin nature, the six parameters, and the ambipolar OECT performance in devices.

In Supplementary Fig. 63, our "high-spin polymer design" affects the ambipolar OECT performance through six parameters. The design strategy can be understood in the following three aspects: (1) A high-spin conjugated polymer has an open-shell electronic structure, which allows it to readily accept and donate electrons due to two electrons occupying two nearly degenerate frontier orbitals, making the generated polaron more stable after electrochemical doping (*Chem. Rev.* 123, 10468-10526 (2023); *Chem* 7, 333-357 (2021)). (2) In high-spin conjugated polymers, the bond order of the chemical bonds between two building blocks is around 1.5 (between the typical single and double bond orders) due to the interconversion of aromatic and quinoid structures. This feature makes the high-spin polymers more planar than traditional closed-shell polymers (*Chem. Soc. Rev.* 41, 7857-7889 (2012); *Chem. Rev.* 119, 11291-11351 (2019)). (3) Suitable substituent modification could tune the energy levels of the high-spin polymers for effective electron/hole injection. To achieve ideal ambipolar OECT performance, both efficient and stable charge transport and injection, should be considered. These require systematic molecular-level engineering. Unlike OFETs, which operate in neutral or lightly doped states, OECT materials usually operate under heavily doped states. To acquire stable polarons, OECT materials should have a smaller energy increase in the p-doped state or a larger energy decrease in the n-doped state than the molecular energy in the neutral state.

Besides, a more planar polaron backbone could lead to more efficient intrachain charge delocalization and interchain hopping (due to better interchain π-π stacking), which are beneficial for efficient charge transport. For efficient charge injection, a higher HOMO level is favorable for hole injection, and a lower LUMO level is favorable for electron injection. Based on these considerations, we propose six parameters (polaron stability, backbone planarity after doping, and HOMO and LUMO energy levels) as listed in Supplementary Fig. 63 to correlate our high-spin design with the ideal ambipolar OECT performance.

In our work, the polymer P(TII-T) was designed based on the first two principles. With its high-spin character, P(TII-T) could easily accept and donate electrons, providing good polaron stability after doping. The interconversion of aromatic and quinoid structures makes P(TII-T) a very planar polaron backbone. However, these capabilities do not ensure that the energy levels of P(TII-T) are suitable for effective hole/electron injection. From the six-parameter analysis (Supplementary Fig. 61), the HOMO energy level of P(TII-T) is good for hole injection, but its LUMO energy level is too high for electron injection. Therefore, we further designed and synthesized two other polymers based on P(TII-T), P(TII-2FT) and P(TII-2ClT), with two fluorine or chlorine atoms substituted on the thiophene to reduce the frontier orbital energy levels for more efficient electron injection. Both P(TII-2FT) and P(TII-2ClT) show more efficient electron injection and balanced OECT performance than P(TII-T), indicating that suitable HOMO/LUMO energy levels are necessary for our high-spin polymer design.

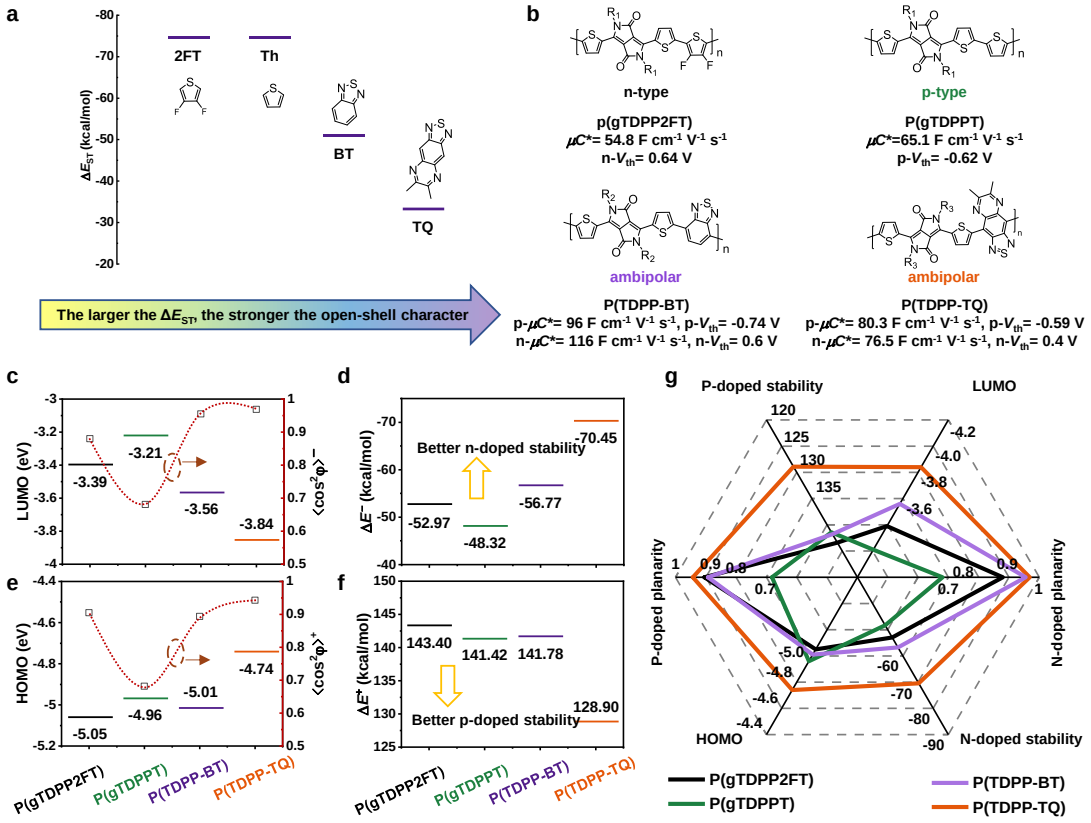

Supplementary Fig. 64 Generality of our high-spin polymer design strategy in the TDPP polymer system. a Calculated ΔE_{ST} values of the four comonomers used for the TDPP polymer system study. **b** Chemical structures, measured μC^* values, and threshold voltages of the four polymers: P(gTDPP2FT) (n-type), P(gTDPPT) (p-type), P(TDPP-BT) (ambipolar), and P(TDPP-TQ) (ambipolar). The side chains of each polymer are omitted for clarity. Although P(TDPP-BT) showed higher p-type and n-type μC^* values than P(TDPP-TQ), P(TDPP-BT) is a typical unbalanced ambipolar polymer, exhibiting electron-dominant transport behavior, and the p-type μC^* value may be overestimated due to the large threshold voltage in the p-type operation regime (Supplementary Fig. 65a, c). **c** LUMO energy levels and n-doped backbone planarity. $\langle\cos^2\varphi\rangle^-$ is the $\langle\cos^2\varphi\rangle$ value of the polymer in a negatively charged state. **d** N-doped stability (ΔE^-). **e** HOMO energy levels and p-doped backbone planarity. $\langle\cos^2\varphi\rangle^+$ is the $\langle\cos^2\varphi\rangle$ value of the polymer in a positively charged state. **f** P-doped stability (ΔE^+). **g** Comparison of the six parameters affecting the device performance of the four TDPP polymers.

Four commonly used building blocks with different ΔE_{ST} values were employed as the comonomers. As shown in Supplementary Fig. 64a, the ΔE_{ST} values of the four comonomers, 2FT, Th, BT, and TQ, increase sequentially, indicating a gradual enhancement of their open-shell characteristics. By polymerizing with the TDPP segment, four polymers, P(gTDPP2FT), P(gTDPPT), P(TDPP-BT), and P(TDPP-TQ), were obtained. The first two closed-shell structures

were reported in our previous work (*Nat. Commun.* 13, 5970 (2022)), while the latter two are newly synthesized with the high-spin structures for comparison. Regarding their OECT performance, P(gTDPP2FT) exhibits unipolar n-type behavior, and P(gTDPPT) exhibits unipolar p-type behavior, while both P(TDPP-BT) and P(TDPP-TQ) exhibit ambipolar behaviors (Supplementary Fig. 65), demonstrating the effectiveness of our molecular design strategy. Further theoretical calculations were conducted to study the molecular energy levels, planarity, and stability of the four polymers (Supplementary Fig. 66). P(gTDPPT) has higher HOMO energy levels and good p-doped stability (Supplementary Fig. 64e, f), occupying the left half of the radar chart, aligning well with its p-type OECT behavior. Similarly, P(gTDPP2FT) occupies the right half of the radar chart (Supplementary Fig. 64g), consistent with its good n-type OECT performance. P(TDPP-BT) and P(TDPP-TQ) span both areas, indicating they could have ambipolar charge transport properties. However, compared to P(TDPP-TQ), the lower HOMO energy level of P(TDPP-BT) results in poor p-type OECT performance. This is well supported by the P(TDPP-BT) OECT device results (Supplementary Fig. 65a-d). P(TDPP-BT) exhibited good n-type OECT output and transfer characteristics, whereas in the p-type operation regime, it exhibited high threshold voltage ($\underline{V}_{Th}$), low transconductance, and possibly overestimated p-type μC^* values (*Nat. Mater.* 23, 2–8 (2024)). The high-spin polymer P(TDPP-TQ) has appropriate HOMO/LUMO energy levels, good p-type/n-type doped stability, and backbone planarity, which enable the polymer to exhibit balanced, efficient, and stable ambipolar OECT performance. The significant differences between P(TDPP-BT) and P(TDPP-TQ) further demonstrate that the six parameters are critical for their ambipolar OECT performance.

In summary, the above results demonstrate that our high-spin polymer design strategy is not limited to the TII system but can also be applied to other polymer systems, such as the TDPP system. Therefore, we successfully demonstrate the generality of our molecular design strategy and are currently exploring its applicability to more polymer systems.

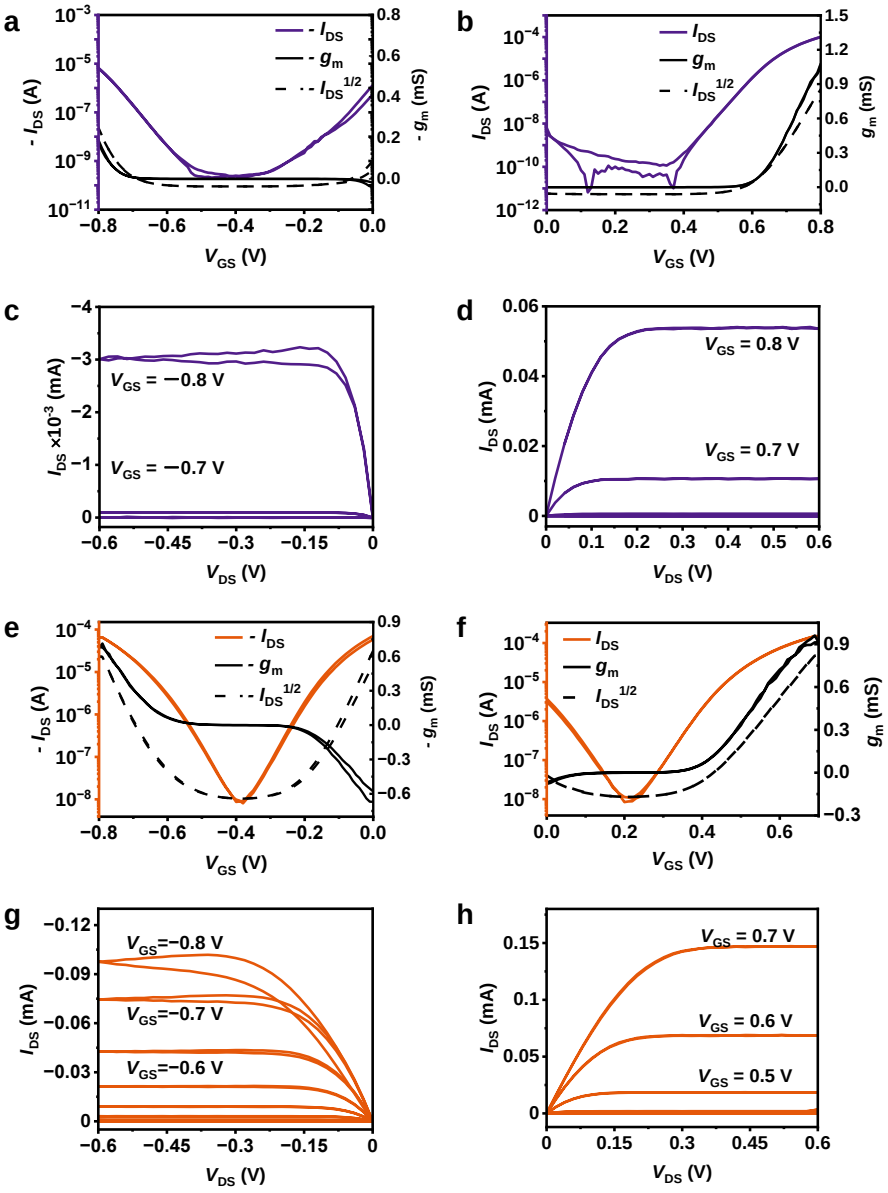

Supplementary Fig. 65 Transfer and output characteristics of OECT devices based on P(TDPP-BT) and P(TDPP-TQ). Typical p-type/n-type OECT transfer characteristics based on **a**/**b** P(TDPP-BT) and **e**/**f** P(TDPP-TQ). Typical p-type/n-type OECT output characteristics based on **c**/**d** P(TDPP-BT) and **g**/**h** P(TDPP-TQ).

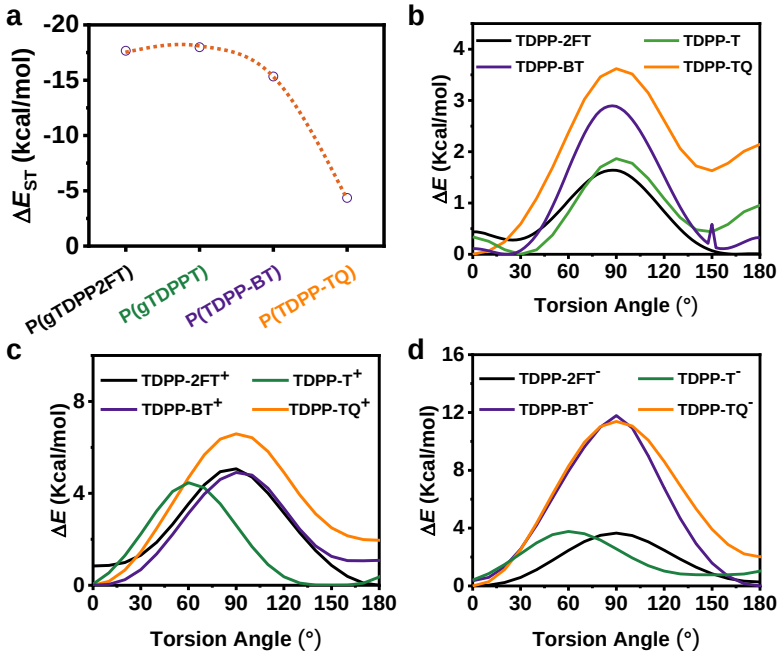

Supplementary Fig. 66 Comparison of the ΔE_{ST} values and the relaxed PES scans of the four DPP polymers. a Calculated ΔE_{ST} values of the trimers of P(gTDPP2FT), P(gTDPPT), P(TDPP-BT), and P(TDPP-TQ). These values indicate that the open-shell characteristics increase in the following order: P(gTDPPT) < P(gTDPP2FT) < P(TDPP-BT) < P(TDPP-TQ). Comparison of the relaxed PES scans of the torsional angles for the four monomers under **b** neutral, **c** positively, and **d** negatively charged states.

3. Synthesis and Characterization of New Compounds

Synthesis of compound 2Cl-T-2Sn

A solution of **2ClT** (177 mg, 1.16 mmol) in dry THF (20 mL) under argon was cooled to −78 ℃, and 2.89 mL (2.89 mmol) of LDA (1 M in THF) was slowly added (over 10 min). The mixture was then stirred for 30 min at −78 ℃, and 2.54 mL (2.54 mmol) of trimethyltin chloride (1 M in THF) was added in 3 min. The mixture was stirred for 1 h at −78 ℃. The reaction was then quenched by adding 40 mL of anhydrous methanol. The mixture was extracted with DCM. The combined organic layers were dried over $MgSO_4$ and concentrated. The product was purified by chromatography on silica gel to yield a colorless oil, **2Cl-T-2Sn** (389 mg, 70.0%). ^{1}H NMR (400 MHz, $CDCl_3$, 298 K, ppm): δ 0.44 (s, 18H, C*H*$_3$). ^{13}C NMR (101 MHz, $CDCl_3$, 298 K, ppm): δ 138.74, 132.02. FTMS (*m/z*): calcd. for $C_{10}H_{18}Cl_2SSn_2$: 479.8550 (100%), Found: 499.0826 (M + H_3O^+, 100%).

Synthesis of compound TII-PEG-7

Under a nitrogen atmosphere, **TII-H** (448 mg, 1.63mmol) and potassium carbonate (1.33 g, 4.09 mmol) were added to 25 mL of *N, N*-dimethylformamide. After heating the mixture to 80 ºC, **R-Br** (1.45 g, 3.60 mmol) in DMF (5 mL) was added dropwise into the mixture and stirred for 12 h. After cooling to room temperature (RT), the mixture was washed with water and extracted with DCM. The residue was purified by silica gel column chromatography using EA/MeOH (*v:v, 30/1*) as the eluent to get a red oil, **TII-PEG-7** (950 mg, 63.3%). ^{1}H NMR (400 MHz, $CDCl_3$, 298 K, ppm): δ 7.51-7.50 (d, *J* = 4.2 Hz, 2H, Th-*H*), 6.97-6.95 (d, *J* = 4.2 Hz, 2H, Th-*H*), 4.01-3.99 (t, *J* = 5.9 Hz, 4H, C*H*$_2$), 3.76-3.73 (m, 4H, C*H*$_2$), 3.63-3.54 (m, 48H, C*H*$_2$), 3.37 (s, 6H, C*H*$_3$). ^{13}C NMR (101 MHz, $CDCl_3$, 298 K, ppm): δ 171.09, 151.71, 134.00, 120.83, 114.11, 112.64, 71.87, 70.58, 70.54, 70.50, 70.45, 70.21, 69.64, 61.62, 58.98, 41.85, 29.63. FTMS (*m/z*): calcd. for $C_{42}H_{66}N_2O_{16}S_2$: 918.3854 (100%), Found: 941.3752 (M + Na^+, 100%).

Synthesis of compound TII-PEG-7-2Br

TII-PEG-7 (143 mg, 0.155 mmol) was added to 20 mL of anhydrous chloroform in a nitrogen atmosphere. After liquid bromine (16.3 μL, 0.318 mmol) was added slowly at 0 ºC, the mixture was

stirred at dark environment for 2 h. After the reaction was quenched by a $NaHSO_4$ aqueous solution, the mixture was washed with water and extracted with DCM. The residue was purified by silica gel column chromatography using EA/MeOH (*v:v, 40/1*) as the eluent to get a red oil, **TII-PEG-7-2Br** (150 mg, 90.1%). ^{1}H NMR (400 MHz, $CDCl_3$, 298 K, ppm): δ 7.04 (s, 2H, Th-*H*), 3.96-3.93 (t, J = 5.2 Hz, 4H, CH_2), 3.72-3.70 (m, 4H, CH_2), 3.64-3.53 (m, 48H, CH_2), 3.37 (s, 6H, CH_3). ^{13}C NMR (101 MHz, $CDCl_3$, 298 K, ppm): δ 170.18, 150.51, 122.58, 119.49, 116.65, 114.59, 71.89, 70.65, 70.62, 70.56, 70.53, 70.47, 69.77, 58.99, 42.00. FTMS (*m/z*): calcd. for $C_{42}H_{64}Br_2N_2O_{16}S_2$: 1074.2064 (100%), Found: 1097.1952 ($M + Na^+$, 100%).

Synthesis of polymer P(TII-T)

Tetratriphenylphosphine palladium (1.35 mg, 1.20 μmol), cuprous iodide (0.44 mg, 2.30 μmol), **T-2Sn** (25.25 mg, 61.3 μmol), and **TII-PEG-7-2Br** (62.7 mg, 58.0 μmol) were combined in a 25 mL Schlenk tube with toluene/N-methylpyrrolidone (5 mL/5 mL). The tube was purged with nitrogen through a freeze-pump-thaw cycle three times. The sealed tube was then heated to 115 ºC and stirred for 48 h. After cooling the reaction mixture to room temperature, diethylphenylazothioformamide (3 mg) was added to remove the catalyst and the resulting mixture was stirred at 80 ºC for 1 h. The reaction mixture was poured into 50 mL of hexane to precipitate and filter the polymer. The solid polymer was placed in a Soxhlet extractor and extracted with hexane, methanol, acetone, and chloroform. The chloroform solution was concentrated under reduced pressure and then poured into 20 mL of hexane to reprecipitate the polymer, **P(TII-T)**. The suspension was filtered and dried under vacuum to obtain the polymer. ^{1}H NMR (400 MHz, $CDCl_3$, 298 K, ppm): δ 7.07, 6.99, 6.87, 6.81, 3.90-3.35; M_n: 11.1 kDa; M_w: 29.3 kDa; PDI: 2.64.

Synthesis of polymer P(TII-2FT)

Tetratriphenylphosphine palladium (1.11 mg, 0.960 μmol), cuprous iodide (0.370 mg, 1.92 μmol), **2FT-2Sn** (22.5 mg, 50.4 μmol), **TII-PEG-7-2Br** (51.6 mg, 48.0 μmol), and toluene/N-methylpyrrolidone (3 mL/3 mL) were added in a 25 mL Schlenk tube. The tube was purged with nitrogen through a freeze-pump-thaw cycle three times. The sealed tube was then heated to 115 ºC and stirred for 48 h. After cooling the reaction mixture to room temperature, diethylphenylazothioformamide (3 mg) was added to remove the catalyst and the resulting mixture

was stirred at 80 ºC for 1 h. The reaction mixture was poured into 50 mL of hexane to precipitate and filter the polymer. The solid polymer was placed in a Soxhlet extractor and extracted with hexane, methanol, acetone, and chloroform. The chloroform solution was concentrated under reduced pressure and then poured into 20 mL of hexane to reprecipitate the polymer, **P(TII-2FT)**. The suspension was filtered and dried under vacuum to obtain the polymer. ^{1}H NMR (400 MHz, $CDCl_3$, 298 K, ppm): δ 6.84, 6.82, 6.67, 3.72-3.33; M_n: 8.48 kDa; M_w: 24.1 kDa; PDI: 2.84.

Synthesis of polymer P(TII-2ClT)

Tetratriphenylphosphine palladium (1.22 mg, 1.10 μmol), cuprous iodide (0.400 mg, 2.10 μmol), **2ClT-2Sn** (26.7 mg, 55.5 μmol), **TII-PEG-7-2Br** (56.9 mg, 53.0 μmol), and toluene/N-methylpyrrolidone (4 mL/4 mL) was added in a 25 mL Schlenk tube. The tube was purged with nitrogen through a freeze-pump-thaw cycle three times. The sealed tube was then heated to 115 ºC and stirred for 48 h. After cooling the reaction mixture to room temperature, diethylphenylazothioformamide (3 mg) was added to remove the catalyst and the resulting mixture was stirred at 80 ºC for 1 h. The reaction mixture was poured into 50 mL of hexane to precipitate and filter the polymer. The solid polymer was placed in a Soxhlet extractor and extracted with hexane, methanol, acetone, and chloroform. The chloroform solution was concentrated under reduced pressure and then poured into 20 mL of hexane to reprecipitate the polymer, **P(TII-2ClT)**. The suspension was filtered and dried under vacuum to obtain the polymer. ^{1}H NMR (400 MHz, $CDCl_3$, 298 K, ppm): δ 6.54, 6.33, 3.71-3.32; M_n: 6.40 kDa; M_w: 17.7 kDa; PDI: 2.76.

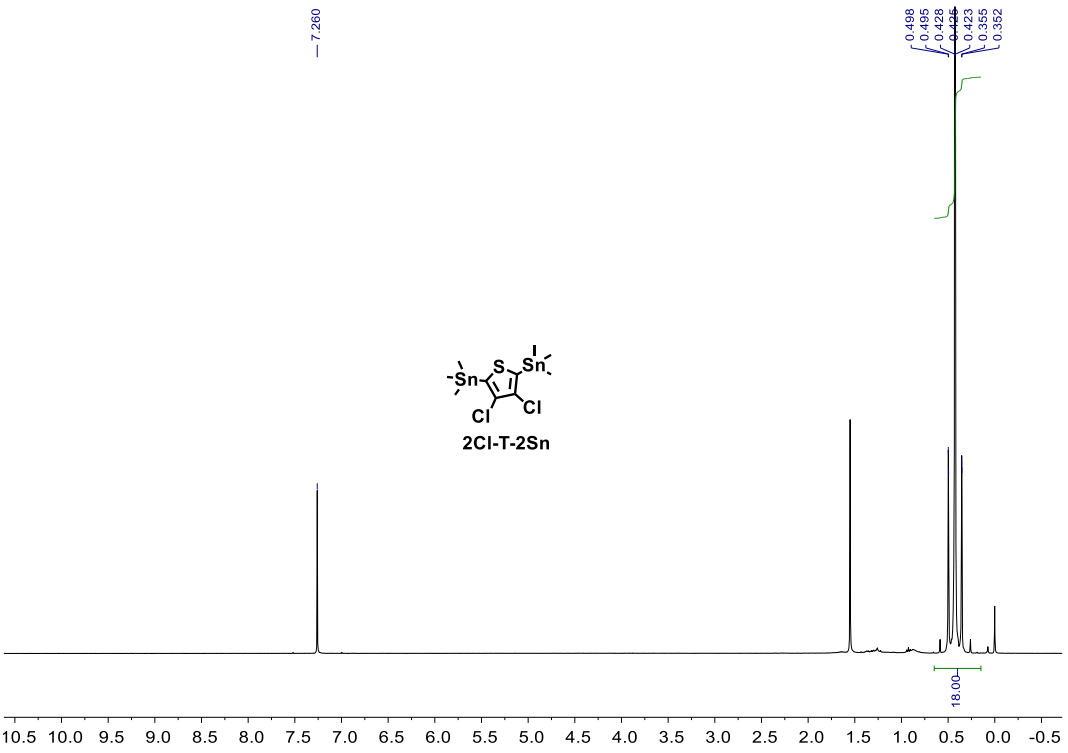

Supplementary Fig. 67 ^{1}H NMR spectrum of 2Cl-T-2Sn. The spectrum is collected using $CDCl_3$ as the solvent at 298 K.

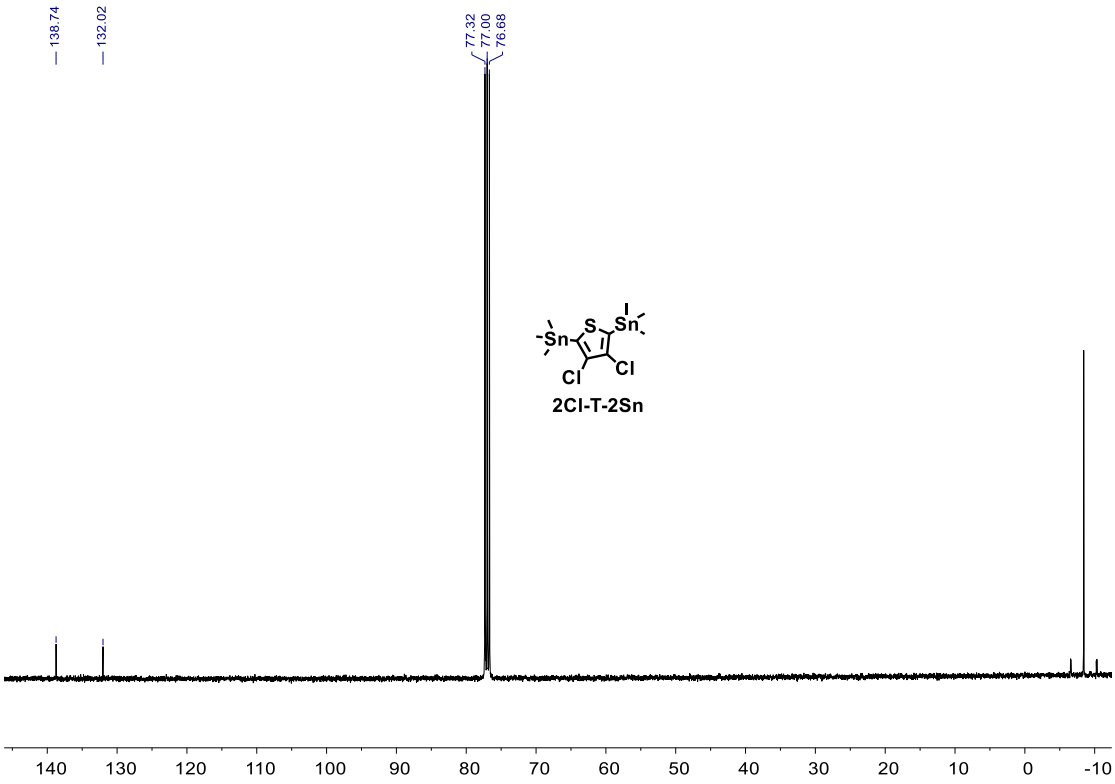

Supplementary Fig. 68 ^{13}C NMR spectrum of 2Cl-T-2Sn. The spectrum is collected using $CDCl_3$ as the solvent at 298 K.

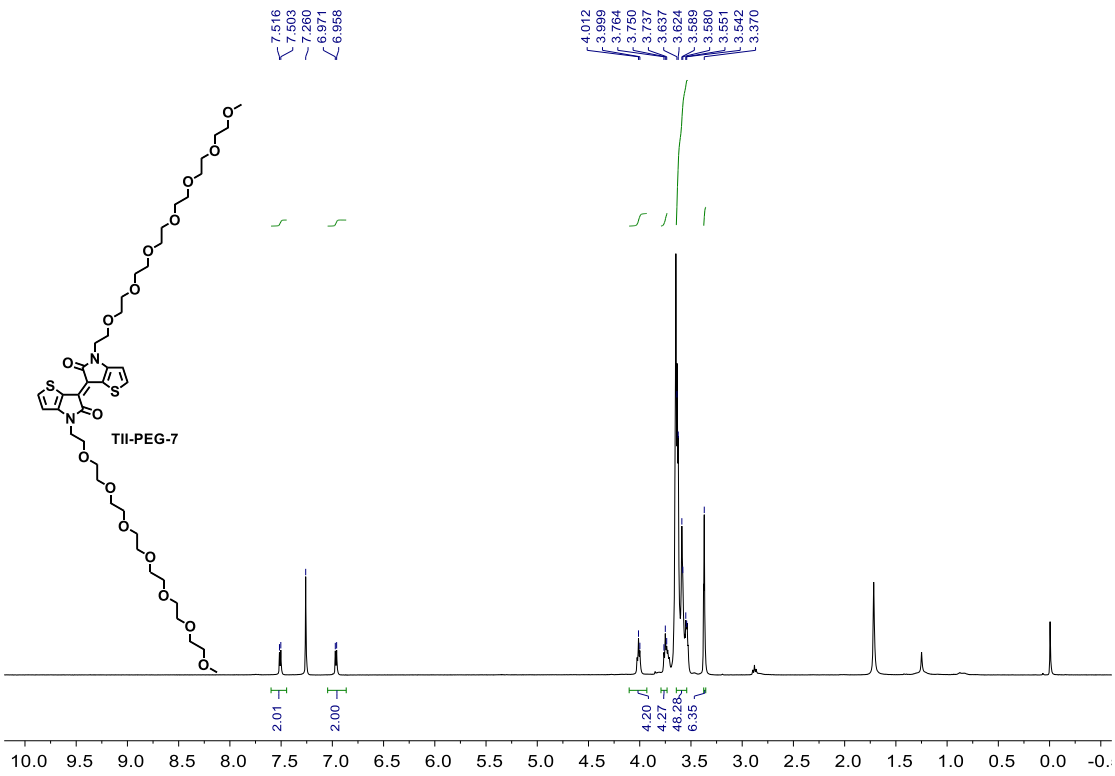

Supplementary Fig. 69 ^{1}H NMR spectrum of TII-PEG-7. The spectrum is collected using $CDCl_3$ as the solvent at 298 K.

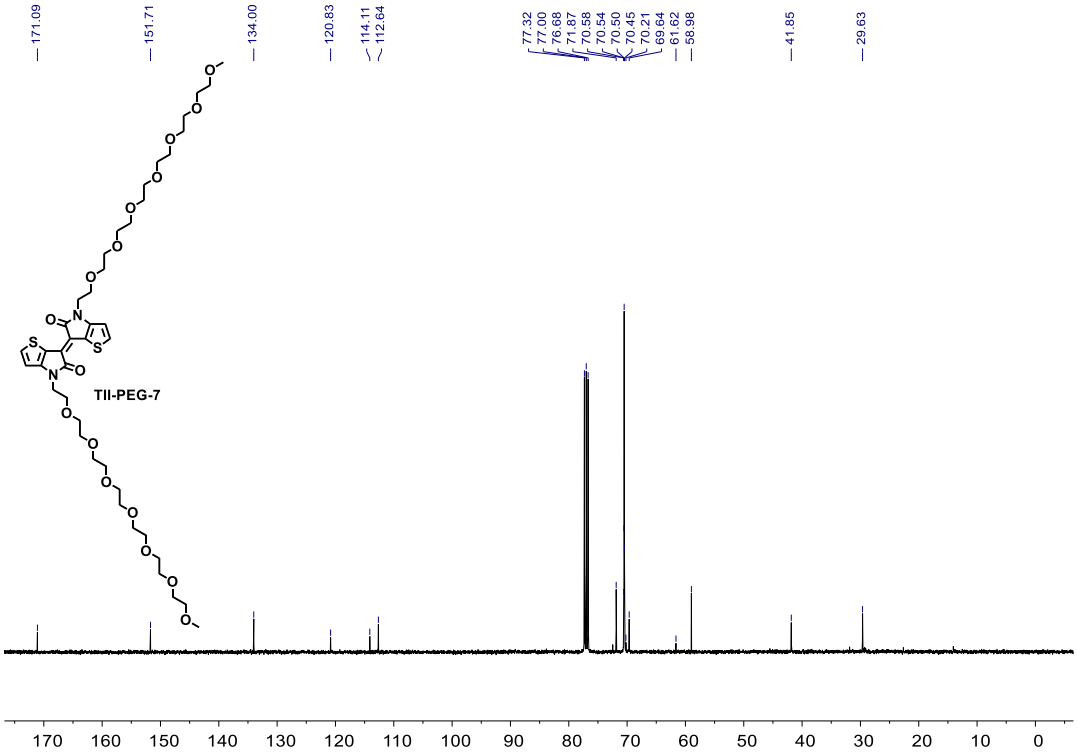

Supplementary Fig. 70 ^{13}C NMR spectrum of TII-PEG-7. The spectrum is collected using $CDCl_3$ as the solvent at 298 K.

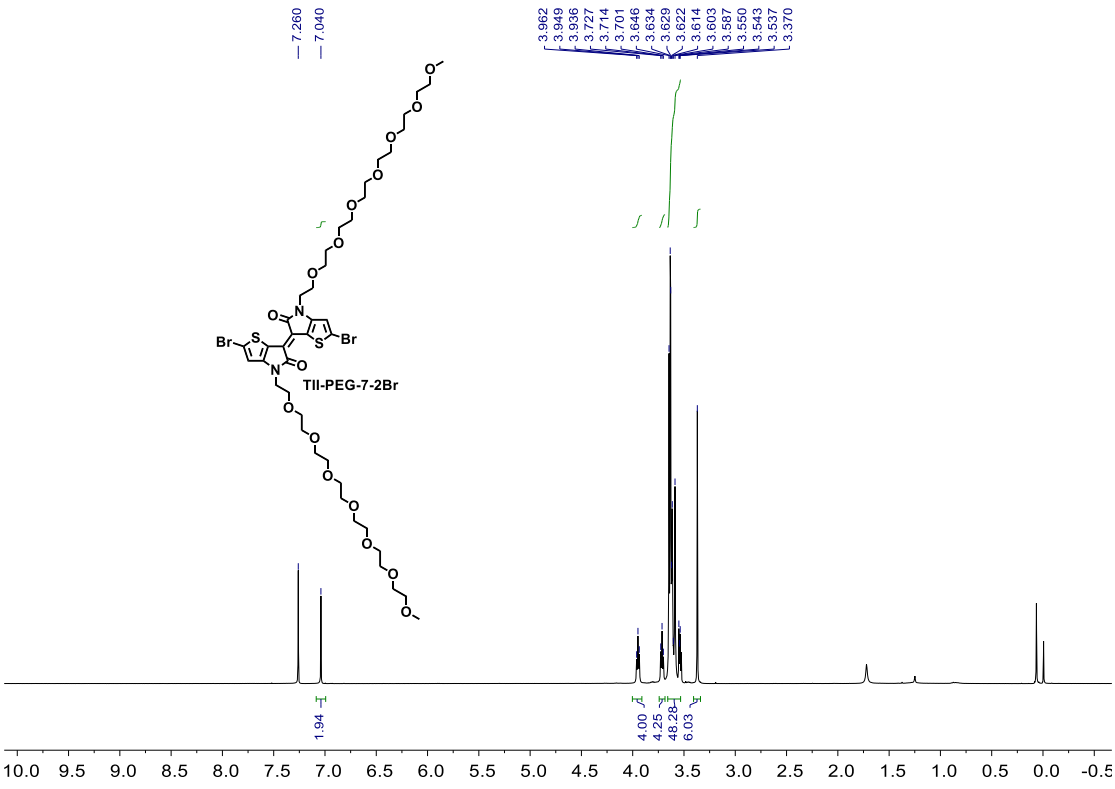

Supplementary Fig. 71 ^{1}H NMR spectrum of TII-PEG-7-2Br. The spectrum is collected using $CDCl_3$ as the solvent at 298 K.

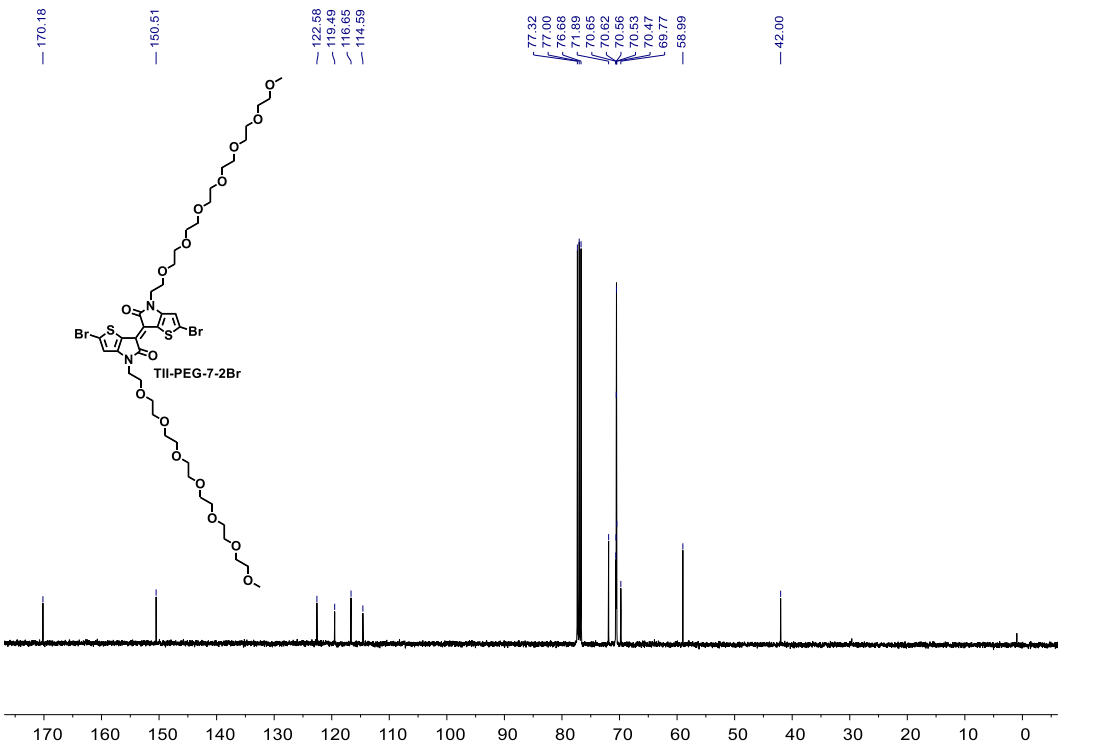

Supplementary Fig. 72 ^{13}C NMR spectrum of TII-PEG-7-2Br. The spectrum is collected using $CDCl_3$ as the solvent at 298 K.

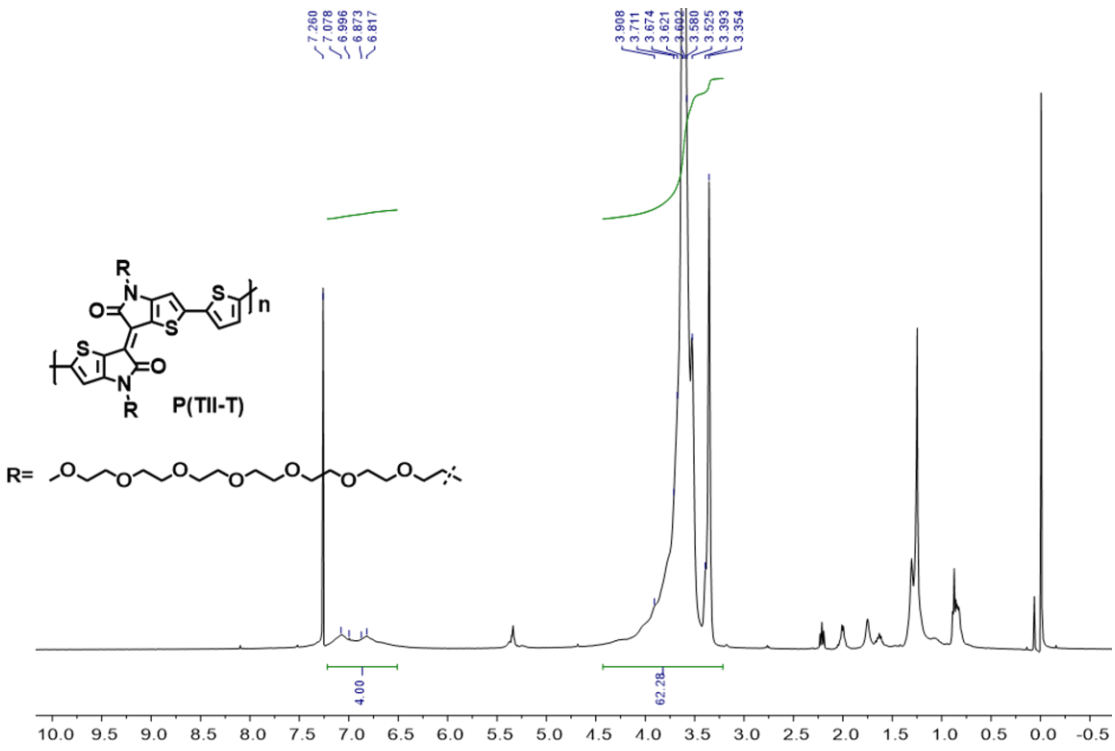

Supplementary Fig. 73 ^{1}H NMR spectrum of polymer P(TII-T). The spectrum is collected using $CDCl_3$ as the solvent at 298 K.

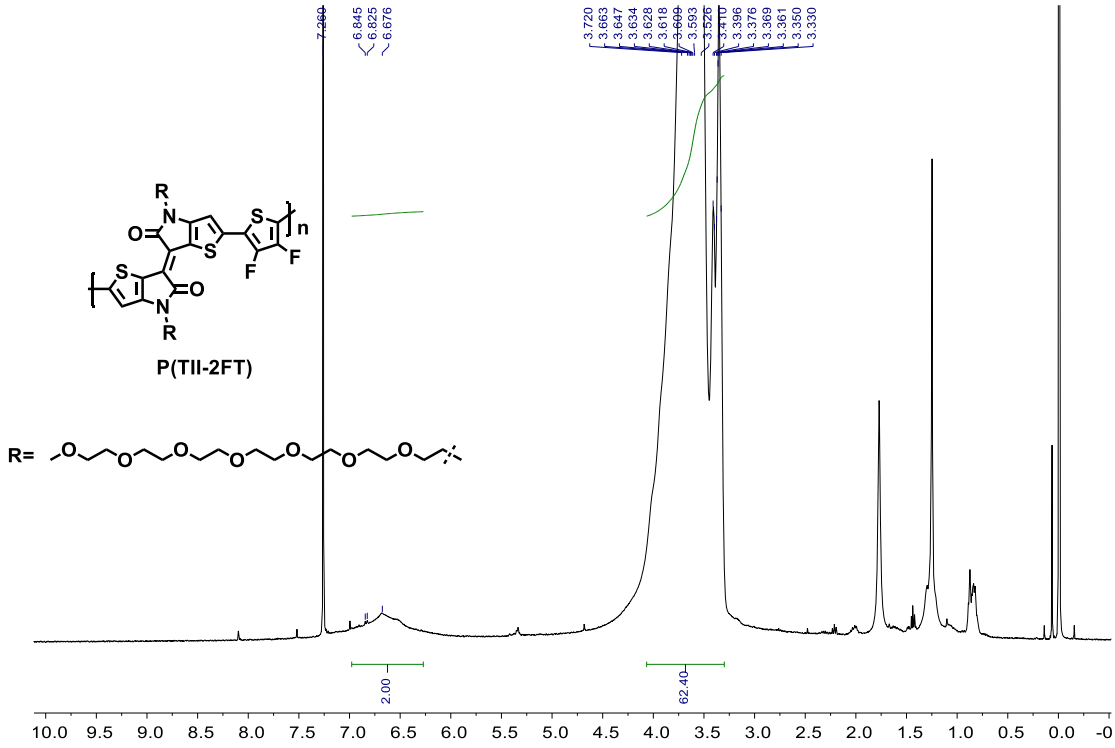

Supplementary Fig. 74 ^{1}H NMR spectrum of polymer P(TII-2FT). The spectrum is collected using $CDCl_3$ as the solvent at 298 K.

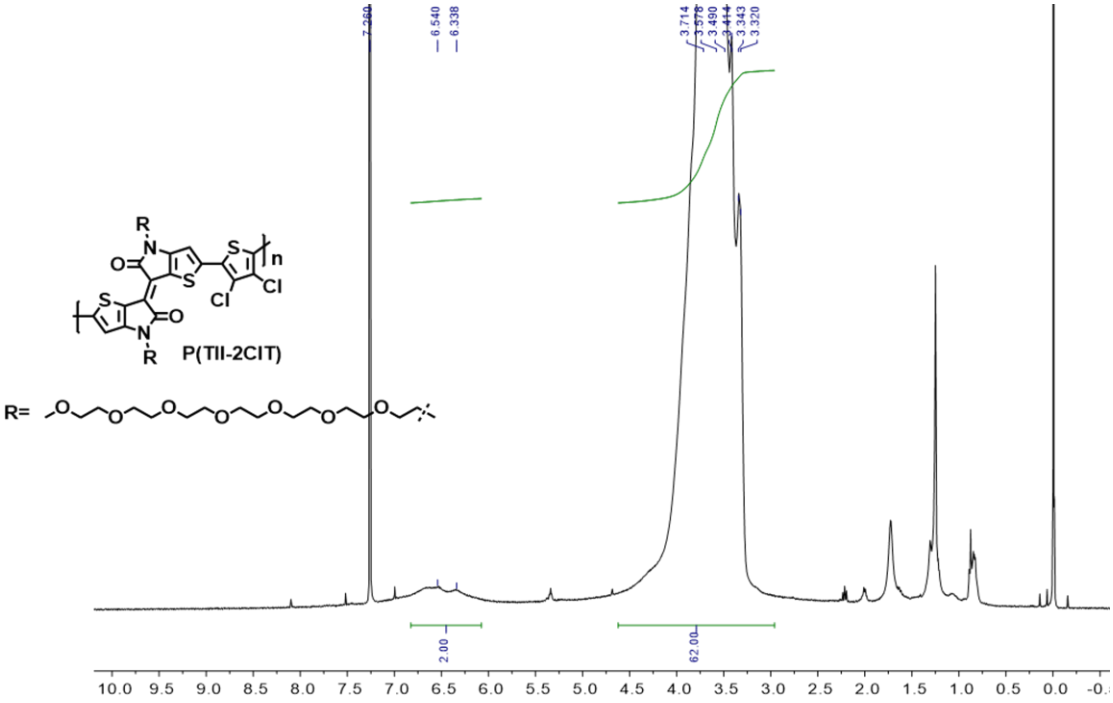

Supplementary Fig. 75 ^{1}H NMR spectrum of polymer P(TII-2ClT). The spectrum is collected using $CDCl_3$ as the solvent at 298 K.

.

4. Supplementary References

1 Frisch, M. *et al.* Gaussian 16 rev. C. 01, wallingford, ct. *Wallingford, CT* (2016).

2 Dennington, R., Keith, T. A. & Millam, J. M. Gaussview, version 6.0. 16. *Semichem Inc Shawnee Mission KS* (2016).

3 Lu, T. & Chen, F. Multiwfn: A multifunctional wavefunction analyzer. *J. Comput. Chem.* **33**, 580-592 (2012).

4 Humphrey, W., Dalke, A. & Schulten, K. Vmd: Visual molecular dynamics. *J Mol Graph* **14**, 33-38, 27-38 (1996).

5 Pan, Y. *et al.* An insight into the role of side chains in the microstructure and carrier mobility of high-performance conjugated polymers. *Polym. Chem.* **12**, 2471-2480 (2021).

6 Wu, H.-Y. *et al.* Influence of molecular weight on the organic electrochemical transistor performance of ladder-type conjugated polymers. *Adv. Mater.* **34**, 2106235 (2022).

7 Feng, K. *et al.* Fused bithiophene imide dimer-based n-type polymers for high-performance organic electrochemical transistors. *Angew. Chem.* **133**, 24400-24407 (2021).

8 Wang, Y. *et al.* Green synthesis of lactone-based conjugated polymers for n-type organic electrochemical transistors. *Adv. Funct. Mater.* **32**, 2111439 (2022).

9 Li, P., Shi, J., Lei, Y., Huang, Z. & Lei, T. Switching p-type to high-performance n-type organic electrochemical transistors via doped state engineering. *Nat. Commun.* **13**, 5970 (2022).

10 Feng, K. *et al.* Cyano-functionalized n-type polymer with high electron mobility for high-performance organic electrochemical transistors. *Adv. Mater.* **34**, 2201340 (2022).

11 Wang, Y. *et al.* Acceptor functionalization via green chemistry enables high-performance n-type organic electrochemical transistors for biosensing, memory applications. *Adv. Funct. Mater.* https://doi.org/10.1002/adfm.202304103 (2023).

12 Yang, W. *et al.* High-performance n-type polymeric mixed ionic-electronic conductors: The impacts of halogen functionalization. *Adv. Mater.* https://doi.org/10.1002/adma.202305416 (2023).

13 Giovannitti, A. *et al.* N-type organic electrochemical transistors with stability in water. *Nat. Commun.* **7**, 13066 (2016).

14 Samuel, J. J. *et al.* Single-component cmos-like logic using diketopyrrolopyrrole-based ambipolar organic electrochemical transistors. *Adv. Funct. Mater.* **31**, 2102903 (2021).

15 Rashid, R. B. *et al.* Ambipolar inverters based on cofacial vertical organic electrochemical transistor pairs for biosignal amplification. *Sci. Adv.* **7**, eabh1055 (2021).

16 Ohayon, D. *et al.* Influence of side chains on the n-type organic electrochemical transistor performance. *ACS Appl. Mater. Interfaces* **13**, 4253-4266 (2021).

17 Stein, E. *et al.* Ambipolar blend-based organic electrochemical transistors and inverters. *Nat. Commun.* **13**, 5548 (2022).

18 Wu, X. *et al.* All-polymer bulk-heterojunction organic electrochemical transistors with balanced ionic and electronic transport. *Adv. Mater.* **34**, 2206118 (2022).

19 Jeong, S. Y. *et al.* Ion gel-gated quasi-solid-state vertical organic electrochemical transistor and inverter. *Adv. Electron. Mater.* **9**, 2300053 (2023).

20 Hou, K. *et al.* High performance, flexible, and thermally stable all-solid-state organic electrochemical transistor based on thermoplastic polyurethane ion gel. *ACS Appl. Electron. Mater.* **5**, 2215-2226 (2023).

21 Sun, H. *et al.* Complementary logic circuits based on high-performance n-type organic electrochemical transistors. *Adv. Mater.* **30**, 1704916 (2018).

22 Zhang, Y. *et al.* High-performance organic electrochemical transistors and neuromorphic devices comprising naphthalenediimide-dialkoxybithiazole copolymers bearing glycol ether pendant groups. *Adv. Funct. Mater.* **32**, 2201593 (2022).

23 Ma, S. *et al.* Sequential cyanation of polythiophenes: Tuning charge carrier polarity in organic electrochemical transistors. *Adv. Electron. Mater.* **n/a**, 2300207

24 Cho, K. G., Seol, K. H., Kim, M. S., Hong, K. & Lee, K. H. Tuning threshold voltage of electrolyte-gated transistors by binary ion doping. *ACS Appl. Mater. Interfaces* **14**, 50004-50012 (2022).

25 Zabihipour, M. *et al.* Organic electrochemical transistors manufactured by laser ablation and screen printing. *Flex. Print. Electron.* **7**, 035018 (2022).

26 Granelli, R. *et al.* High-performance bioelectronic circuits integrated on biodegradable and compostable substrates with fully printed mask-less organic electrochemical transistors. *Small* **18**, 2108077 (2022).

27 Romele, P., Ghittorelli, M., Kovács-Vajna, Z. M. & Torricelli, F. Ion buffering and interface charge enable high performance electronics with organic electrochemical transistors. *Nat. Commun.* **10**, 3044 (2019).

28 Wu W, *et al.* Selenophene Substitution Enabled High-Performance n-Type Polymeric Mixed Ionic-Electronic Conductors for Organic Electrochemical Transistors and Glucose Sensors. *Adv. Mater.* **36**, 2310503 (2024).

29 Moser M, *et al.* Side Chain Redistribution as a Strategy to Boost Organic Electrochemical Transistor Performance and Stability. *Adv. Mater.* **32**, 2002748 (2020).

30 Wu X, Liu Q, Surendran A, Bottle SE, Sonar P, Leong WL. Enhancing the Electrochemical Doping Efficiency in Diketopyrrolopyrrole-Based Polymer for Organic Electrochemical Transistors. *Adv Electron. Mater.* **7**, 2000701 (2021).

31 Leydecker T, Wang ZM, Torricelli F, Orgiu E. Organic-based inverters: basic concepts, materials, novel architectures and applications. *Chemical Society Reviews* **49**, 7627-7670 (2020).